



Article

<https://doi.org/10.1038/s41594-025-01685-4>

Epigenetic priming promotes tyrosine kinase inhibitor resistance and oncogene amplification

Received: 31 March 2025

Accepted: 26 August 2025

Published online: 23 October 2025

Check for updates

A list of authors and their affiliations appears at the end of the paper

In mammalian cells, gene copy number is controlled to maintain gene expression and genome stability. However, a common molecular feature across cancer types is oncogene amplification, increasing the copy number and expression of tumor-promoting genes and thus promoting cancer progression. For example, in tyrosine kinase inhibitor (TKI)-resistant lung adenocarcinoma (LUAD), oncogene amplification is frequent. Despite the prevalence of oncogene amplification in TKI-resistant tumors, the underlying mechanisms are not fully understood. Here, we find that LUADs exhibit a unique chromatin signature demarcated by strong CTCF and cohesin deposition in drug-naive tumors, which correlates with the boundaries of oncogene amplicons in TKI-resistant LUAD cells. We identify a global chromatin-priming effect during the acquisition of TKI resistance, marked by a dynamic increase of H3K27Ac, cohesin loading and inter-TAD interactions, which occur before the onset of oncogene amplification. Furthermore, we show that METTL7A, reported to localize to the endoplasmic reticulum and inner nuclear membrane, has a chromatin regulatory function by binding to amplified loci and regulating cohesin recruitment and inter-TAD interactions. METTL7A appears to remodel the chromatin landscape prior to large-scale copy number gains. Although *METTL7A* depletion exerts little phenotypical effects on drug-naive cells, its depletion prevents the formation and maintenance of TKI resistant-clones, showcasing its role as cells become resistant. In summary, we unveil a mechanism required for the acquisition of TKI resistance regulated by an unexpected chromatin function of METTL7A.

Acquired resistance to TKIs, such as osimertinib, a third-generation TKI, is a major clinical challenge in treating *EGFR*-mutant non-small-cell lung cancer (NSCLC). One common mechanism of TKI resistance is oncogene amplification^{1–5}, which occurs in more than 40% of TKI-resistant lung adenocarcinoma (LUAD) tumors harboring *EGFR* mutations⁶. Oncogene amplification can occur both intrachromosomally and through the form of extrachromosomal DNA (ecDNA)^{7–12}. Despite the prevalence of oncogene amplification in TKI-resistant tumors, it is not fully understood how chromatin architecture changes throughout the acquisition of resistance to facilitate oncogene amplification. Furthermore, although previous studies have demonstrated that TKI-resistant tumors emerge from a quiescent, drug-tolerant persister (DTP) stage characterized by a unique

and reversible epigenetic state¹³, the mechanisms that govern the exit from the DTP stage and entry into a proliferative, drug-resistant stage remain elusive. Here, we identify the chromatin regulator METTL7A, which is specifically upregulated as LUAD cells exit the DTP stage and develop resistance to osimertinib. METTL7A has a crucial role in shaping the epigenetic landscape of future amplicons by recruiting the cohesin complex.

TKI-resistant LUAD tumors exhibit diverse forms of oncogene amplicons

To understand the genomic changes associated with osimertinib resistance in LUAD tumors, we conducted whole-genome sequencing (WGS) in paired parental and osimertinib-resistant (OR) *EGFR*-mutant LUAD

e-mail: andrew.xiao@yale.edu

cell lines: PC9/PC9-OR, HCC827/HCC827-OR and H1975/H1975-OR (Extended Data Fig. 1a). Our AmpliconArchitect (AA) analysis¹⁴ revealed gene amplification in parental and resistant cells, which was increased in resistant cells. This finding is consistent with oncogene amplification being a common feature of osimertinib resistance in tumors of patients (Fig. 1a,b)⁶. In accordance with previous work¹⁵, *RAF1* was one of the most highly amplified oncogenes in PC9-OR cells. In HCC827 cells, *EGFR* was amplified in both parental and osimertinib-resistant cells, with increased copy numbers in HCC827-OR cells. Furthermore, HCC827-OR cells exhibited *MET* amplification, consistent with previous reports that have identified *MET* amplification as a mechanism of gefitinib resistance in the HCC827 cell line⁴ and osimertinib resistance in tumors⁶. In H1975 cells, we observed *PVT1-MYC* amplification in both parental and resistant cells. In addition, we observed that osimertinib-resistant cells consistently exhibited an increased amplicon complexity score, a metric that accounts for the size and number of amplicons¹⁶ (Extended Data Fig. 1b). We validated these results through DNA fluorescence in situ hybridization (FISH) using probes targeting amplified oncogenes and non-amplified chromosomal control loci (Fig. 1c and Extended Data Fig. 1c,d). Metaphase FISH revealed that most amplified oncogenes adopted the form of homogeneously staining regions (HSRs), which can arise from ecDNA reintegration into chromosomes (Extended Data Fig. 1e), compared with extrachromosomal amplification (Extended Data Fig. 1f). We performed RNA sequencing (RNA-seq) and correlated these results with our AA analysis, identifying that the amplified oncogenes were some of the most highly expressed genes in the transcriptome (Fig. 1d and Supplementary Table 1).

We next examined whole-exome sequencing (WES) and RNA-seq data from people with NSCLC ([NCT02759835](#)) to explore the prevalence of oncogene amplification in pre-osimertinib-treated and osimertinib-resistant EGFR-mutant LUADs. In accordance with previous results¹⁷, we identified four tumors that developed *MET* amplification and five that developed *EGFR* amplification in the samples, and, similar to our analyses in cell lines, these amplified genes were often the most highly expressed ones (Supplementary Fig. 1).

To further understand the structure of the oncogene amplicons in osimertinib-resistant tumors, we performed WGS and AA analysis on patient-derived xenograft (PDX) models from a subset of osimertinib-treated individuals from [NCT02759835](#) (ref. 18) (Supplementary Table 2 and Extended Data Fig. 2a,b). Across the PDXs, the most frequently amplified oncogenes were *EGFR*, *MDM2*, *KRAS* and *MET* (Extended Data Fig. 2c). Of the four resistant tumors with high oncogene amplification (>50 genes amplified), diverse amplicon structures were detected by AA. These amplified oncogenes correlated strongly with high transcription (Extended Data Fig. 2d). Furthermore, these tumors exhibited high amplicon-complexity scores, suggesting that these amplicons could have undergone cycles of amplification, recombination and integration during tumor evolution (Extended Data Fig. 2e).

Together, using *in vitro*, PDX and clinical-trial data, our results indicate that oncogene amplification is highly prevalent in osimertinib-resistant *EGFR*-mutant LUAD, and these amplicons occur in the form of diverse chromosomal and extrachromosomal structures.

A unique chromatin landscape in drug-naïve EGFR-mutant LUAD correlates with oncogene amplicon boundaries in TKI-resistant LUAD and other tumor types

Although we observed a range of amplicon structures, we hypothesized there could be a unique chromatin signature permitting the amplification of oncogene amplicons. Alterations in chromatin topology have been well documented in cancer^{19–23}, and these alterations can be caused by changes in the binding of CCCTC-binding factor (CTCF), which regulates chromatin structure by demarcating topologically associated domains (TADs), also known as contact domains. Thus,

we sought to determine whether amplicon boundaries were associated with CTCF. We analyzed CTCF chromatin immunoprecipitation sequencing ([ENCSR243INX](#)) and Hi-C data ([ENCSR859DRK](#)) from the ENCODE Project^{24,25}, performed in parental PC9 cells. We correlated CTCF binding in PC9 cells with our PC9-OR WGS data and observed that CTCF was enriched at the boundaries of amplicons determined by AA compared with randomly shuffled, non-amplicon coordinates ($P < 7.5 \times 10^{-15}$, Fisher's exact test; Fig. 1e, left). This finding is surprising because this CTCF enrichment occurred in drug-naïve PC9 cells lacking detectable levels of oncogene amplification (Fig. 1b–d). We deemed these loci 'future amplicons' on the basis of the observation that CTCF is enriched over the boundaries of these loci in cells that have not yet become amplified. To determine the strength of the CTCF signal at these future-amplicon boundaries, we compared our findings with the CTCF signal at TAD boundaries, as annotated on the basis of PC9 Hi-C data from ENCODE. The CTCF signal over amplicon boundaries was even more pronounced than at TAD boundaries (Fig. 1e, right). We observed that CTCF was frequently enriched on one side of the amplicon boundary, a feature similar to super-stripes, which facilitate long-range interactions across TAD boundaries²⁶. This contrasts with the enriched CTCF signal observed at both ends of TAD boundaries (Fig. 1e). To assess CTCF enrichment at loop anchors, we performed CUT&RUN analysis of the cohesin component RAD21 in drug-naïve PC9 cells and correlated these findings with CTCF data. We observed a similar enrichment of RAD21 at the future-amplicon boundaries, with a similar bias toward enrichment at one end of the amplicon (Fig. 1e, bottom).

We next classified amplicons into four categories, on the basis of the presence of at least one CTCF-binding site within 10 kb upstream or downstream of the amplicon edges: amplicons with an upstream CTCF-binding site, a downstream CTCF-binding site, both upstream and downstream CTCF-binding sites, or no such sites (Fig. 1f, left). We plotted CTCF signal over amplicons within each category and observed a significant overlap between the presence of CTCF binding within 10 kb of the amplicon boundary (Fisher's Exact Test, $P < 8.5 \times 10^{-12}$), with 18/35 amplicons exhibiting this one-sided enrichment (Fig. 1f, right). Even for the amplicons characterized by two-sided CTCF binding (9/35), the CTCF signal was still stronger at one amplicon boundary than at the other (Fig. 1f, right). When we examined individual amplicons, the similarity to architectural super-stripes became even more apparent. For example, PC9-OR cells exhibited an amplicon on chromosome 7, containing the genes *UPK3BL2*, *RASA4* and *POLR2J2*. The upstream boundary of this amplicon contained a strong CTCF-binding site, oriented toward the amplicon, which overlapped with RAD21 deposition (Fig. 1g).

We next correlated CTCF binding in PC9 cells with the amplified intervals in the PDXs derived from previously described osimertinib-treated tumors. In two PDXs, LAT001 and TMN0123 (Extended Data Fig. 2a), we observed that the CTCF signal was similarly enriched over the amplicon boundaries, with a biased enrichment near one side (Extended Data Fig. 2f,g). These data suggest that, before oncogene amplification, a unique chromatin landscape signature could already exist at the future-amplicon boundaries, which may be regulated via cohesin-mediated loop extrusion.

To determine whether this observation occurs in other tumor types, we re-analyzed WGS data from PC3 (ref. 7) prostate cancer cells and *BRAF*^{V600E}-mutated M249 melanoma cells resistant to vemurafenib (BRAF inhibitor) and selumetinib (MEK inhibitor)²⁷. We correlated these data with CTCF chromatin immunoprecipitation and sequencing (ChIP-seq) data from PC3 ([ENCSR359LOD](#)) and neural crest cells ([ENCSR218MVT](#)), respectively, from ENCODE^{24,25}. We analyzed data from neural crest cells because they are the progenitors of melanocytes, which eventually give rise to melanoma. Thus, we reasoned that CTCF deposition in neural crest cells could more closely resemble melanocytes than other tissue types. As was the case for LUAD tumors, we observed an enriched CTCF signal at the amplicon boundaries in

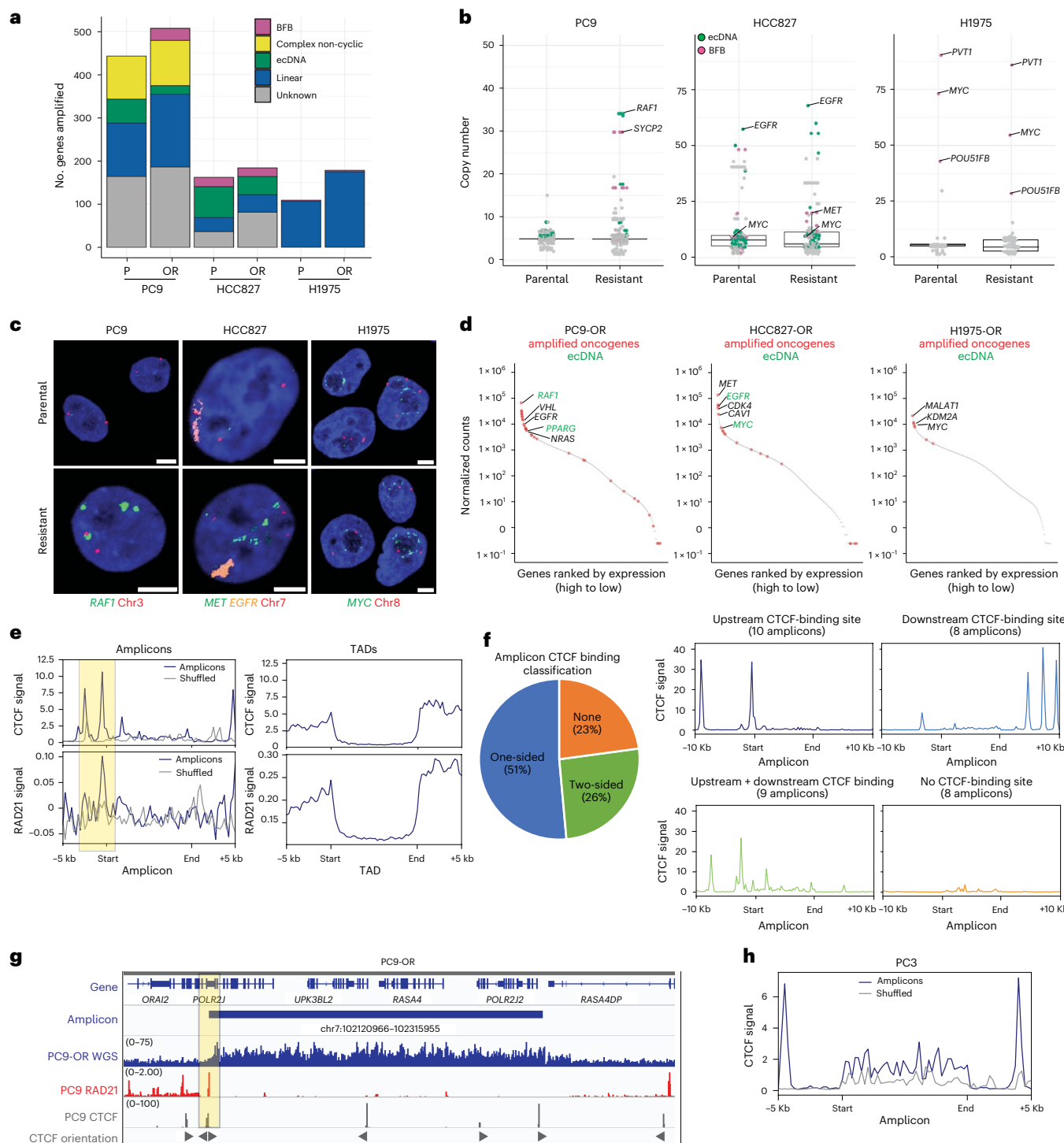


Fig. 1 | Osimertinib-resistant EGFR-mutant LUADs exhibit oncogene amplicons demarcated by CTCF binding. **a**, WGS and AA analysis of parental and osimertinib-resistant cells showing the breakdown of amplicon structures across cell lines. P, parental; OR, osimertinib-resistant. **b**, Scatterplot of genes amplified across cell lines reveals an increase in amplicon copy number in PC9-OR and HCC827-OR cells compared with their parental counterparts. Pink and green dots denote genes predicted to be amplified through breakage–fusion–bridge (BFB) cycles and as ecDNA, respectively, on the basis of AA analysis. WGS data are from one biological replicate per cell line. Box plot center, median; hinges, first and third quartiles; whiskers, hinge $\pm 1.5 \times$ IQR. **c**, Representative FISH images of amplified oncogenes and unamplified, control chromosomal loci. Scale bars, 5 μ m. **d**, Ranked RNA expression plots in osimertinib-resistant cell lines. Red dots, amplified oncogenes; green dots, ecDNA based on WGS/AA analysis. **e**, Analysis of average CTCF and RAD21 signal at the boundaries of amplicons (left) compared

with the average signal at TAD boundaries (right) in PC9 cells. CTCF and RAD21 signal is increased at amplicon boundaries. Amplicon boundaries are determined by AA/WGS analysis in PC9-OR cells, and TAD boundaries are determined by PC9 Hi-C. Because amplicons range in size from approximately 15 kb to 10 Mb, the CTCF signal was plotted over scaled amplicons. The intersection between CTCF peaks and amplicons: $P < 7.5 \times 10^{-15}$, Fisher's exact test. **f**, Left, amplicon CTCF motif classification on the basis of the presence of a CTCF motif within 10 kb of the start and/or end of the amplified interval. CTCF ChIP data are from PC9 parental cells; amplicons are based on AA from PC9-OR cells. Right: PC9 CTCF signal plotted over each of the PC9-OR amplicons, categorized by the presence of CTCF motifs. **g**, Example IGV tracks showing CTCF (light grey) and RAD21 (red) enrichment over amplicon (dark blue) boundaries. CTCF orientation is indicated by gray triangles. **h**, CTCF signal plotted over amplicons (or amplicon coordinates shuffled over the genome, gray) in PC3 cell line.

the PC3 (Fig. 1h) and M249 (Extended Data Fig. 2h) cell lines. Although vemurafenib- and selumetinib-resistant M249 cells only contained one amplicon (*BRAF*), we were intrigued by the observation that CTCF was enriched at this locus in neural crest cells, which do not harbor gene amplification.

We investigated ENCODE histone-modification ChIP-seq data from PC9 cells to hone in on the distinct epigenetic profile of the future amplicon boundaries. We observed enrichment for euchromatic histone modifications, such as histone H3 dimethylated at K79 (H3K79me2) across the future amplicons and H3 monomethylated at K4 (H3K4me1) near the upstream boundary of amplified regions. By contrast, we observed no correlation between repressive histone modifications (such as H3 trimethylated at K9 (H3K9me3) and H3K27me3) and amplicon boundaries (Extended Data Fig. 2i,j).

These observations suggest that non-amplified, drug-naïve tumor cells could have a predefined chromatin structure permissive to the future amplification of these loci, a phenomenon that might occur in multiple types of oncogene-amplified cancer.

Dynamic changes in chromatin architecture precede oncogene amplification during acquired resistance

Previous studies have demonstrated that TKI-resistant tumors emerge from a quiescent, DTP stage characterized by a unique, reversible epigenetic state^{13,28}. However, the mechanisms that govern the exit from the DTP stage and entry into a proliferative, drug-resistant stage, remain elusive (Fig. 2a). Furthermore, the time point at which oncogene amplification occurs during the acquisition of resistance in *EGFR*-mutant LUAD is unknown. To address these questions, we first performed a time-course experiment in which we treated PC9 parental cells with escalating doses of osimertinib for 3 months and probed for oncogene amplification. We examined global copy number by plotting the normalized sequencing read coverage over each PC9-OR amplicon locus at three time points: 0, 6–8 or 12 weeks of osimertinib treatment. After 6–8 weeks of treatment, PC9 cells started to enter an exponential growth stage, and after 12 weeks, cells were resistant to osimertinib. We observed a global increase in copy number after 12 weeks of treatment (Extended Data Fig. 3a). Consistent with the bulk sequencing data, we probed for *RAF1* amplification through DNA FISH and observed that global *RAF1* amplification occurred after 12 weeks of treatment (Fig. 2b,c). At the 6- to 8-week stage, we observed a modest yet significant increase in *RAF1* copy number, suggesting that this is the time point immediately preceding global increases in gene copy number.

Fig. 2 | METTL7A promotes the acquisition of osimertinib-resistant LUAD.

a, Schematic of the PC9 cell line model of acquired osimertinib resistance. Cells transition through a quiescent DTP state before entering a proliferative resistant state. +osi, osimertinib treatment. **b**, DNA FISH for the *RAF1* locus (green) in PC9 cells treated for 0, 8 or >12 weeks with osimertinib. –osi, no osimertinib treatment. **c**, Quantification of **b**. Significance was determined by unpaired two-sided *t*-test. *n*, number of nuclei imaged per sample from two biological replicates. **d**, Total number of significant H3K27ac peaks (left) and RAD21 peaks (right) in PC9 cells treated without osimertinib or for 8 weeks with osimertinib. The consensus peaks, determined on the basis of IDR analysis between two biological replicates, are plotted. **e**, H3K27ac CUT&RUN signal in PC9 cells that were treated without osimertinib or were treated with osimertinib for 6–8 weeks, centered on genes significantly upregulated upon osimertinib treatment. H3K27ac signal is normalized by counts per million (CPM) and H2A is subtracted. The gain of H3K27ac signal in 8-week osimertinib-treated cells is not correlated with differentially expressed genes. **f**, The CTCF signal is enriched at H3K27ac (top) and RAD21 (bottom) peaks gained upon osimertinib treatment compared with peaks randomly shuffled over the genome. **g**, Ranked RNA-expression plot showing the differentially expressed ($P_{adj} < 0.001$) putative and known chromatin and epigenetic factors that are upregulated (red, $\log_2(FC) > 1$) or downregulated (blue, $\log_2(FC) < 1$) in PC9 cells after 5 weeks of osimertinib treatment. **h**, Heatmap

We next addressed how chromatin architecture changes during the acquisition of osimertinib resistance before oncogene amplification. Because histone-acetylation changes are associated with the DTP stage^{13,28}, we performed H3K27ac CUT&RUN. We observed a global increase in H3K27ac levels in PC9 cells treated with osimertinib for 6–8 weeks compared with levels in drug-naïve PC9 cells (Fig. 2d, left). Although this time point occurs before global oncogene amplification, we observed a significant intersection between the H3K27ac peaks gained with osimertinib treatment after 6–8 weeks and the oncogene amplicons in PC9-OR cells ($P < 2 \times 10^{-10}$, Fisher's exact test). We assessed whether the gain of H3K27ac peaks corresponded to changes in gene expression. Although H3K27ac is frequently associated with transcriptional upregulation, the gained H3K27ac peaks were not correlated with concurrent gene expression changes (Fig. 2e and Extended Data Fig. 3b) and instead were associated with CTCF deposition from PC9 parental cells (Fig. 2f). We hypothesized that changes in cohesin-mediated chromatin looping occur during the acquisition of resistance. Thus, we performed CUT&RUN for the core cohesin component RAD21. As was the case for H3K27ac, we observed a global increase in RAD21 deposition in PC9 cells treated with osimertinib for 6–8 weeks (Fig. 2d, right), which was also correlated with the CTCF signal (Fig. 2f). These data suggest that chromatin undergoes dynamic changes that precede massive oncogene amplification as tumors acquire resistance to osimertinib, suggestive of a chromatin-priming event.

We next addressed the functional effects of oncogene amplification during acquired resistance. We transduced PC9 and HCC827 parental cells with short hairpin RNAs (shRNAs) targeting either *RAF1* or *MET*, respectively, or a non-targeting control shRNA and treated cells with osimertinib over the course of approximately 1 month (Extended Data Fig. 3c). We found that both *RAF1* and *MET* knockdown resulted in significantly fewer osimertinib-resistant clones in PC9 and HCC827 cells, respectively, than in control cells ($P < 2.2 \times 10^{-16}$ and $P < 2 \times 10^{-7}$, respectively; Extended Data Fig. 3d,e), further emphasizing the functional role of oncogene amplification during the acquisition of resistance.

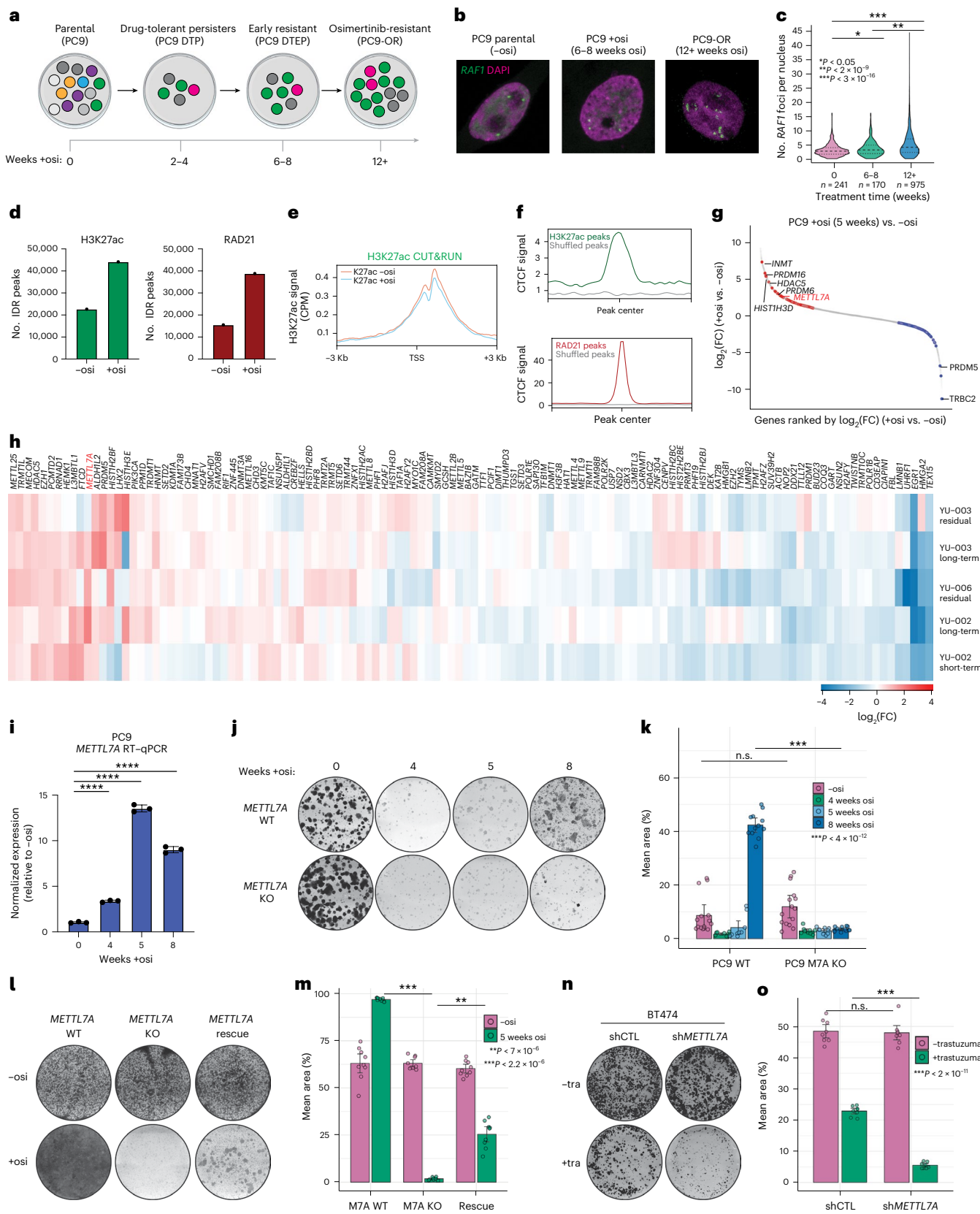
METTL7A promotes the acquisition of osimertinib resistance

We next investigated factors that facilitate chromatin organization prior to oncogene amplification. We were particularly interested in factors upregulated after 5 weeks of osimertinib treatment, which corresponds to the exit from the DTP stage. Given the dynamic change in chromatin landscape during the acquisition of resistance, we

of differentially expressed epigenetic factors in PDX models (YU-002, YU-003, YU-006) treated with osimertinib compared with vehicle. *METTL7A* (red) is one of the top upregulated genes across PDX samples treated with osimertinib. **i**, RT-qPCR validation of RNA-seq shows significant upregulation of *METTL7A* during the acquisition of osimertinib resistance in PC9 cells. $P < 0.0001$ (from left to right: $P = 2.12 \times 10^{-6}$, 5.63×10^{-7} , 1.12×10^{-6}), calculated through an unpaired two-sided *t*-test. The s.d. is based on three technical replicates. Mean \pm s.d. is plotted. **j**, Long-term colony-formation assay in PC9 WT and *METTL7A*-KO cells stained with crystal violet at the indicated time points during chronic (1 μ M) osimertinib treatment. **k**, Quantification of **j**. *** $P = 3.39 \times 10^{-12}$. Error bars represent the s.d. between three biological replicates. **l**, Colony-formation assay of PC9 WT, *METTL7A*-KO and *METTL7A*-rescue cells treated with increasing doses of osimertinib (0.1 to 1 μ M) for 5 weeks. *METTL7A* (M7A) rescue cells were derived by overexpressing *METTL7A* in the KO background. **m**, Quantification of the colony-formation assay results. The mean is plotted and error bars represent the s.d. between biological triplicates. Significance was determined by an unpaired two-sided *t*-test. ** $P = 7.04 \times 10^{-6}$, *** $P = 2.2 \times 10^{-16}$. **n**, Crystal violet assay performed in shCTL or sh*METTL7A* BT474 breast cancer cells treated with or without trastuzumab. **o**, Quantification of **n**. The mean is plotted, and error bars represent the s.d. between biological triplicates. Significance was determined by unpaired two-sided *t*-test. n.s., non-significant. *** $P = 1.21 \times 10^{-11}$.

specifically profiled known and putative chromatin binding and/or epigenetic factors for differential expression between untreated and osimertinib-treated cells at multiple time points. Five weeks after treatment, we identified 43 factors that were significantly upregulated ($P_{adj} < 0.001$, $\log_2(\text{FC}) > 1$) in osimertinib-treated cells compared with

parental PC9 cells (Fig. 2g). Similarly, we identified 39 putative and known epigenetic factors that were significantly upregulated at both the 4-week and 8-week time points (Extended Data Fig. 4a). To discern which factors were most essential for resistance, we analyzed RNA-seq data from matched vehicle- and osimertinib-treated PDX



tumors, consisting of PDXs treated with osimertinib for approximately 3 days (short term) or multiple months (long term), and residual tumors that persisted after osimertinib treatment²⁹. One of the top shared, differentially upregulated genes was *METTL7A*, which encodes methyltransferase-like protein 7A (*METTL7A*). *METTL7A* was significantly upregulated in PC9 cells treated at all 3 time points (4, 5 and 8 weeks post-osimertinib treatment) and in 4/5 osimertinib-treated PDX tumors (Fig. 2h). We validated this result with qRT-PCR in PC9 and HCC827 cells, which similarly showed that *METTL7A* expression peaked after 5 weeks of treatment (Fig. 2i and Extended Data Fig. 4b).

We addressed whether the observed upregulation arises from a pre-existing, *METTL7A*-high population or is induced upon osimertinib treatment. We analyzed published single-cell RNA-seq (scRNA-seq) data from untreated and osimertinib-treated, drug-tolerant residual cells from an *EGFR*-mutant lung adenocarcinoma PDX, YU-006 (ref. 29). We observed that *METTL7A* expression was enriched in cluster 8, which is predominantly composed of osimertinib-treated, drug-tolerant cells. Unlike untreated cells in clusters 2 and 8, *METTL7A* expression was specific to the osimertinib-treated, drug-tolerant residual cells in cluster 8 (Extended Data Fig. 4d,e). This suggests that osimertinib treatment leads to increased expression of *METTL7A*, rather than selection of a pre-existing, *METTL7A*^{hi} population.

To interrogate the function of *METTL7A* in acquired resistance, we knocked out *METTL7A* in parental PC9 cells and challenged wild-type and *METTL7A*-knockout (KO) cells with 1 μM osimertinib for 8 weeks. Although parental wild-type cells acquired resistance and resumed proliferation in the presence of osimertinib after 5 weeks, *METTL7A*-KO cells could not exit the DTP stage and largely died by 8 weeks of treatment (Fig. 2j,k), similar to the phenotype we observed upon depletion of major amplified oncogenes in PC9 and HCC827 cells (Extended Data Fig. 3c,d). We rescued this phenotype by overexpressing *METTL7A* in the KO background and confirmed *METTL7A* expression through western blot and RT-qPCR (Extended Data Fig. 4c). We observed a moderate yet significant rescue effect ($P < 7 \times 10^{-6}$), suggesting that *METTL7A* is crucial for cells to acquire resistance (Fig. 2l,m). We confirmed this phenotype through shRNA-mediated knockdown of *METTL7A* in both PC9 and HCC827 parental cells and validated efficient knockdown with RT-qPCR (Extended Data Fig. 4f). Similar to *METTL7A*-KO cells, when treated with osimertinib, sh*METTL7A*-transduced PC9 and HCC827 cells failed to generate osimertinib-resistant clones, in contrast to parental cells transduced with a non-targeting control shRNA (Extended Data Fig. 5g,h). Moreover, there was no significant growth phenotype in *METTL7A*-deficient drug-naïve cells (Fig. 2j,k, $P = 0.21$; Extended Data Fig. 4g,h).

To investigate whether *METTL7A* is required to maintain osimertinib resistance, we performed cell-viability assays in osimertinib-resistant PC9 cells (PC9-OR) depleted of *METTL7A* using shRNA. We performed this in resistant cells taken off osimertinib for the duration of the experiment (~2 weeks) or in PC9-OR cells in which *METTL7A* was knocked down in the presence of osimertinib. In PC9-OR cells taken off osimertinib, we saw a modest yet significant decrease in resistant colonies in sh*METTL7A* versus shCTL cells (Extended Data Fig. 4i,j). In PC9-OR cells kept on osimertinib, we saw an even greater decrease in colonies upon *METTL7A* depletion. We calculated the ‘resistance index’ for both genotypes by dividing the mean percentage area of crystal violet staining in osimertinib-treated cells by the mean percentage area in cells taken off osimertinib. The resistance index was lower for sh*METTL7A*-transfected cells, suggesting that, even after normalizing by the number of cells taken off osimertinib, *METTL7A* depletion had an additional effect on drug treatment (Extended Data Fig. 4k). These results suggest that *METTL7A* has a role in maintaining resistance, but because the effect is less significant than that of *METTL7A* depletion in the DTP stage, we believe that *METTL7A*’s function is likely more important for the acquisition of resistance.

Finally, we investigated whether *METTL7A* is essential for acquired resistance in other oncogene-amplified cancers treated with targeted therapies. We used *HER2*-amplified BT474 breast cancer cells that can acquire resistance to the *HER2* inhibitor trastuzumab. We depleted *METTL7A* with shRNA and treated cells with trastuzumab for 2 months. Like our findings in *EGFR*-driven LUAD, we found that *METTL7A* depletion significantly impaired the emergence of trastuzumab-resistant clones without affecting cell viability in drug-naïve cells (Fig. 2n,o). This suggests that *METTL7A* might mediate drug resistance in other targeted therapy contexts. Together, these data strongly indicate that *METTL7A* plays a specific and crucial role in acquired resistance.

METTL7A binds to amplified oncogenes and correlates with CTCF binding

We next investigated the mechanism through which *METTL7A* promotes acquired resistance. *METTL7A* has previously been reported to localize to the endoplasmic reticulum and inner nuclear membrane but not the nuclear interior or chromatin^{30,31}. To elucidate the localization of *METTL7A* in LUAD cells, we performed immunofluorescence in PC9/PC9-OR and HCC827/HCC827-OR cells that express *METTL7A* fused to the MYC tag and FLAG epitope tags (*METTL7A*-MYC-FLAG) owing to lack of reliable antibodies that detect endogenous *METTL7A* through immunofluorescence. Consistent with previous reports, we observed strong accumulation of *METTL7A* in the cytoplasm of PC9 and HCC827 parental cell lines (Supplementary Videos 1 and 3). However, we observed both cytoplasmic and nuclear localization of *METTL7A* in osimertinib-resistant cells (Fig. 3a,b and Supplementary Videos 2, 4 and 5). We quantified nuclear *METTL7A* foci and found that there were significantly more foci in resistant cells than in parental cells (Fig. 3c). We additionally performed subcellular fractionation and observed increased *METTL7A* in the nuclear fraction of osimertinib-resistant cells compared with parental cells (Extended Data Fig. 5a).

On the basis of *METTL7A*’s nuclear localization, we wanted to determine whether it binds chromatin. We performed ChIP-seq in resistant and parental cells overexpressing the *METTL7A*-MYC-FLAG fusion protein and used a MYC-tag antibody to capture *METTL7A*’s localization on chromatin. We identified 4,937 and 3,165 high-confidence *METTL7A* peaks in both PC9-OR and HCC827-OR cells, respectively, that expressed *METTL7A*-MYC-FLAG fusion protein, compared with little *METTL7A* binding in parental cell lines (Fig. 3d and Methods). Approximately 60% of amplified oncogenes in both PC9-OR and HCC827-OR cells contained a *METTL7A* peak (Extended Data Fig. 5b), such as the *RAFI*-containing amplicon locus, which was one of the most amplified loci in PC9-OR cells (Extended Data Fig. 5c). We annotated *METTL7A* peaks in OR cells and identified an increased proportion of peaks present on promoters compared to the rest of the genome (Extended Data Fig. 5d). Additionally, we performed motif and gene ontology analyses on total *METTL7A* peaks and promoter peaks, respectively, but did not identify any common motifs between PC9-OR and HCC827-OR cells (Extended Data Fig. 5e,f).

On the basis of our observation that CTCF is enriched on the boundaries of future amplicons, we analyzed the correlation between *METTL7A* binding and CTCF using ChIP-seq in PC9 cells. We found a strong correlation between *METTL7A* binding and CTCF signal (Fig. 3e), and observed a significant overlap between *METTL7A* peaks and CTCF peaks ($P < 2 \times 10^{-10}$) in PC9-OR cells. By contrast, H3K9me2 and H3K9me3 ([ENCSR521GRK](#) and [ENCSR555TAX](#), respectively) were significantly excluded from *METTL7A* peaks ($P < 4 \times 10^{-6}$ and $P < 3 \times 10^{-7}$, respectively) (Extended Data Fig. 5g). These results suggest that *METTL7A* binds to amplified genes in osimertinib-resistant cells and correlates with CTCF-binding sites.

We next investigated the residues responsible for *METTL7A*’s chromatin-binding activity and mutated lysine residues that might be responsible for *METTL7A*’s DNA-binding activity, honing in on the residue K86. We overexpressed the K86A mutant in the *METTL7A*-KO

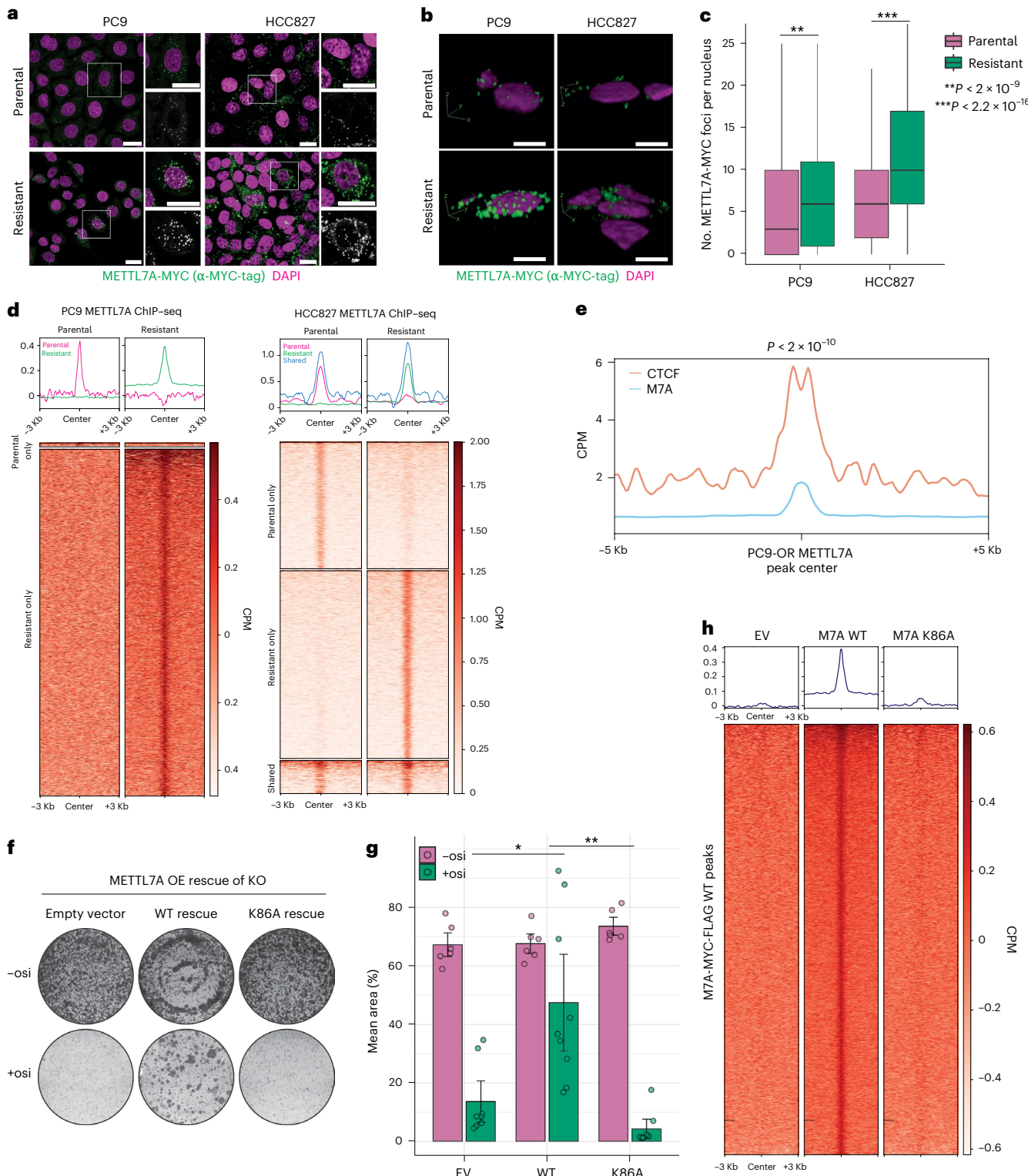


Fig. 3 | METTL7A binds to amplified oncogenes. **a**, Immunofluorescence in PC9 and HCC827 cells expressing MYC-tagged METTL7A shows increased nuclear localization of METTL7A in osimertinib-resistant cells compared with parental cells. Scale bars, 20 μ m. **b**, 3D reconstruction of PC9 and HCC827 cells expressing MYC-tagged METTL7A. Scale bar, 5 μ m. **c**, Quantification of **a** reveals a significant increase in the number of nuclear METTL7A foci in OR cells compared with parental cells. Data are from three biological replicates. Box plot center, median; hinges, first and third quartiles; whiskers, hinge $\pm 1.5 \times$ IQR. Statistics, two-sided *t*-test. **d**, Heatmaps of METTL7A MYC-tag ChIP-seq in PC9 and HCC827 cells. The signal is separated on the basis of peaks called in parental cells only, resistant cells only or peaks in both parental and resistant cells. Signal is normalized on the

basis of CPM and signal from input. **e**, The CTCF signal is enriched over METTL7A peaks. Signal is normalized by CPM. METTL7A peaks significantly intersect CTCF peaks ($P < 2 \times 10^{-10}$, Fisher's exact test, two-sided). **f**, Colony-formation assays in parental cells that were treated with or without osimertinib. Colony-formation assays were performed in METTL7A-KO cells with reconstituted wild-type (WT) METTL7A or METTL7A-K86A (or empty-vector control). **g**, Quantification of **f**. Error bars, s.d. between biological triplicates. Significance was determined by unpaired *t*-test. * $P = 0.0017$; ** $P = 0.00184$. **h**, MYC-tag ChIP-seq reveals a depletion of signal upon overexpression of M7A-FLAG-MYC-K86A mutant, similar to ChIP in cells overexpressing a FLAG-MYC EV. The mean ChIP signal between biological replicates is shown. Signal is normalized to the input.

background and validated that mutant METTL7A and WT METTL7A were expressed at similar levels (Extended Data Fig. 5h). To test whether K86 has a functional role in vivo, we treated *METTL7A*-KO cells rescued with an empty vector (EV), WT METTL7A or METTL7A-K86A with or without osimertinib and stained cells after 5 weeks. Whereas METTL7A WT overexpression in *METTL7A*-depleted cells rescued the drug-sensitivity phenotype, overexpression of the K86A mutant failed to do so (Fig. 3f,g).

We next tested whether METTL7A-K86A affects the localization or chromatin-binding activity of METTL7A. We observed a significant decrease in the number of METTL7A nuclear foci in the K86A mutant compared with the WT (Extended Data Fig. 5i,j). Furthermore, we performed ChIP-seq against the MYC-tag in PC9-OR cells overexpressing a FLAG-MYC EV; wildtype M7A-MYC-FLAG; or M7A-MYC-FLAG with a K86A mutation. K86A reduced METTL7A's ability to bind chromatin (Fig. 3h). These results suggest that the K86 residue is critical for METTL7A's function in the acquisition of drug resistance, nuclear localization and binding to chromatin.

To elucidate the chromatin-binding activity of METTL7A, we purified MBP-tagged METTL7A from *Escherichia coli* (Extended Data Fig. 6a), incubated it with 60 bp double-stranded DNA and single-stranded DNA substrates, and ran the complex on a non-denaturing gel. We observed an upward shift of the MBP-METTL7A-DNA complex at increasing concentrations of METTL7A (Extended Data Fig. 6b). As a positive control, we performed the DNA-binding assay with the DNMT3A2-DNMT3L complex³² and found that its binding affinity for DNA is similar to that of METTL7A (Extended Data Fig. 6c-e). We performed the same assay with the K86A mutant and observed that its binding affinity was moderately reduced compared with that of the wild-type METTL7A protein (Extended Data Fig. 6e). These data support the notion that METTL7A binds to DNA in vitro, and the K86 residue could be responsible for METTL7A's chromatin binding activity in vivo.

METTL7A primes the chromatin landscape for oncogene amplification

On the basis of the enrichment of CTCF and RAD21 signal over amplicon boundaries, the correlation between METTL7A and CTCF binding and METTL7A's binding activity toward DNA, we hypothesized that METTL7A primes the chromatin landscape during resistance acquisition. We performed H3K27ac and RAD21 CUT&RUN in *METTL7A* wildtype, KO, and rescue cells under drug-naïve conditions or after cells were treated with osimertinib for 6–8 weeks. During this period, we observed global changes in chromatin architecture, but this was before major oncogene amplification (Figs. 2b,c and 4a). Strikingly, our data demonstrated that the global chromatin re-organization was abolished in *METTL7A*-KO cells treated with osimertinib: on the basis of PCA analysis of H3K27ac and RAD21 CUT&RUN signal, the chromatin state in *METTL7A*-KO cells treated with osimertinib was nearly indistinguishable from that of their drug-naïve counterparts (Fig. 4b). Additionally, the peaks gained upon osimertinib treatment in wild-type PC9 cells were those lost upon KO of *METTL7A* in osimertinib-treated cells (Fig. 4c). We could partially rescue this phenotype by overexpressing *METTL7A* in the KO background (Extended Data Fig. 7a). In untreated PC9 cells, we observed a modest decrease in H3K27ac and RAD21 deposition upon *METTL7A* KO, but the effect was stronger in drug-treated cells (Extended Data Fig. 7b). These data suggest that METTL7A is crucial for the chromatin-structure changes and epigenetic priming as cells exit the DTP stage but before oncogene amplification.

We next assessed the mechanism through which METTL7A primes chromatin. We identified nuclear METTL7A-interacting proteins through nuclear fractionation, immunoprecipitation, mass spectrometry and APOSTL SAINT analysis³³ in parental and osimertinib-resistant PC9 cells expressing tagged METTL7A. (Supplementary Table 3 and Methods). We found that PDS5A interacts with METTL7A, which is intriguing because PDS5A is known to

load and unload cohesin to chromatin and localizes to CTCF-loop anchors³⁴. We validated this interaction by performing immunoprecipitation, followed by western blotting, and that these two proteins interact in both the METTL7A overexpression and endogenous contexts (Extended Data Fig. 7c,d). Additionally, we performed proximity ligation assays (PLAs) and identified significantly more METTL7A-PDS5A PLA foci in cells expressing METTL7A-MYC-FLAG than in wild-type controls (Extended Data Fig. 7e,f).

We next determined whether METTL7A-mediated changes in the chromatin landscape were due to METTL7A's association with PDS5A. We performed PDS5A CUT&RUN in wild-type, *METTL7A*-KO and *METTL7A*-rescue cells at the aforementioned time points. We first correlated PDS5A CUT&RUN signal with METTL7A ChIP-seq peaks and observed a significant overlap ($P < 2 \times 10^{-10}$, Fisher's exact test) between PDS5A and METTL7A peaks (Fig. 4d). When we centered PDS5A signal from wild-type, *METTL7A*-KO or *METTL7A*-rescue cells on the PC9-OR *METTL7A* peaks, we observed decreased PDS5A signal upon knock out, and the PDS5A signal was fully restored in the rescue cells (Fig. 4d). We performed the same analysis with RAD21, and found that it was depleted in *METTL7A*-KO cells at METTL7A-binding sites, and its binding was almost completely restored in the rescue cells (Fig. 4e). On the basis of these findings, we hypothesized that METTL7A affects cohesin deposition through PDS5A recruitment, either directly or indirectly, to chromatin. Indeed, we observed a 47% decrease in global PDS5A peaks in *METTL7A*-KO cells compared with wild-type cells (Fig. 4f), and PDS5A signal was decreased globally (Extended Data Fig. 7g). Similar to our H3K27ac and RAD21 CUT&RUN data, we observed only modest effects of *METTL7A* KO on PDS5A deposition in parental cells (Extended Data Fig. 7h). Although PDS5A has been shown to both load and unload the cohesin complex^{34–37}, the concomitant loss of both PDS5A and RAD21 binding upon *METTL7A* KO suggests that PDS5A is likely more responsible for loading of the cohesin complex in this context. We observed a strong overlap between both PDS5A and RAD21 peaks in our CUT&RUN data (Extended Data Fig. 7i). We ruled out the possibility that differences in PDS5A and RAD21 deposition were due to changes in expression upon *METTL7A* KO, because we observed no differences in PDS5A and RAD21 protein levels between genotypes (Extended Data Fig. 7j).

On the basis of our findings that METTL7A promotes acquisition of osimertinib resistance through PDS5A-mediated cohesin deposition and global chromatin reorganization, we asked which specific gene targets METTL7A regulates. We observed that, in PC9 cells treated with osimertinib for 6–8 weeks, before any oncogene amplification, METTL7A targets PDS5A and RAD21 to future amplified oncogenes, such as the *RAF1* locus: in *METTL7A*-KO cells, PDS5A and RAD21 are depleted at these 'future amplicons.' These sites further correlate with METTL7A deposition, on the basis of the METTL7A ChIP-seq data (Extended Data Fig. 7k). The future amplicons correlate most strongly with CTCF binding, cohesin deposition and METTL7A peaks. In summary, these results suggest that METTL7A recruits the cohesin complex to CTCF-enriched loci and 'primes' chromatin for amplification.

Previous work has shown that DNA amplification caused by super-helical tension is regulated by topoisomerase 2B, which relieves topological stress at loop anchors³⁸. Thus, we assessed whether TOP2B functions downstream of this METTL7A-mediated chromatin-priming mechanism. We performed TOP2B CUT&RUN in parental and osimertinib-treated wild-type and *METTL7A*-KO PC9 cells. We observed increased TOP2B signal in wild-type cells treated with osimertinib, which was depleted upon *METTL7A* KO (Fig. 4g, red box), reminiscent of the changes in RAD21 and H3K27ac deposition. We looked for correlations in these data and our H3K27ac and RAD21 CUT&RUN data, and found that the TOP2B signal in wild-type PC9 cells treated with osimertinib correlates with H3K27ac and RAD21 sites gained upon osimertinib treatment (Fig. 4h,i). At these sites, TOP2B signal is reduced upon *METTL7A* depletion. Together, these results suggest that the

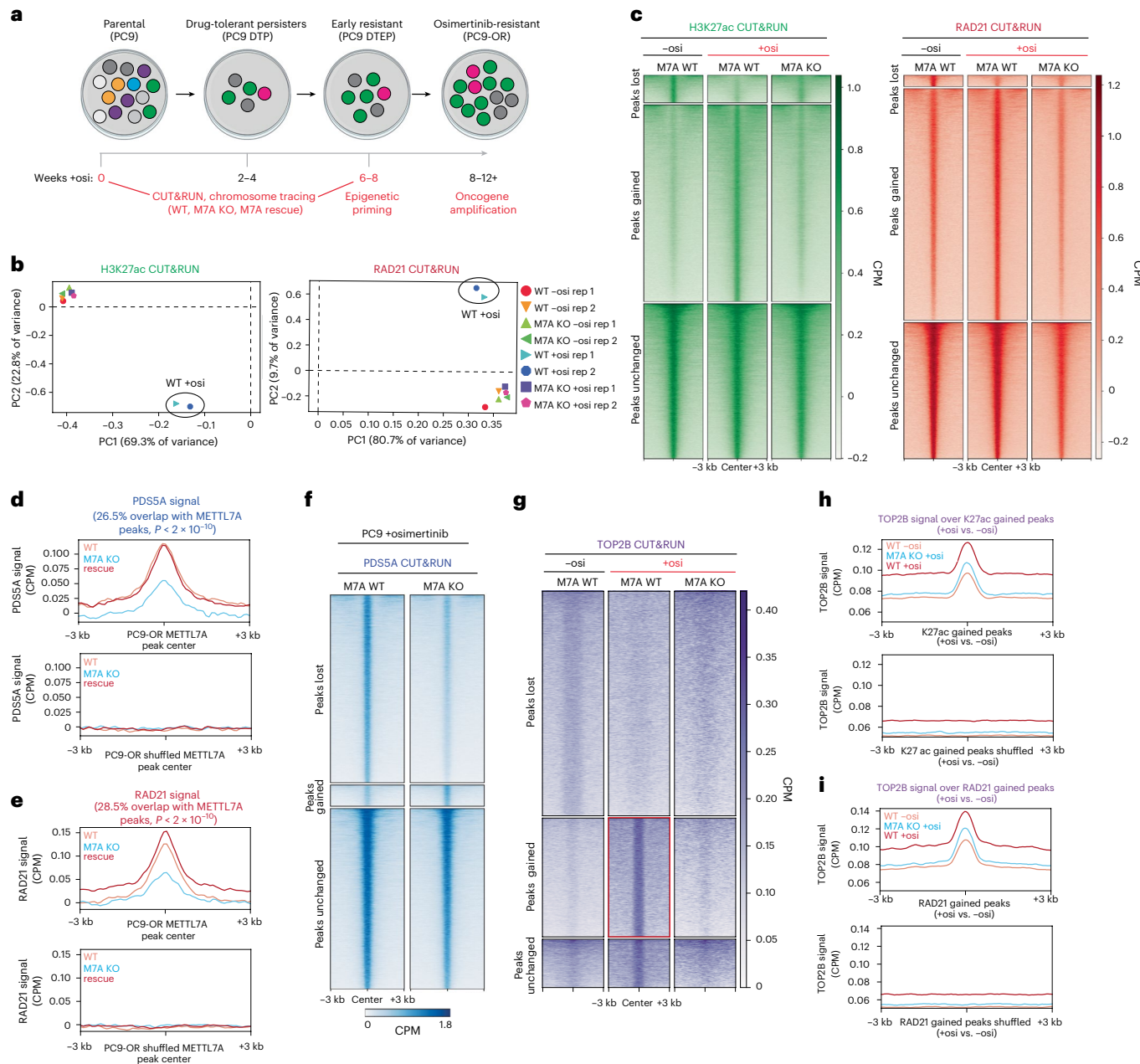


Fig. 4 | METTL7A primes chromatin through recruitment of cohesin components. **a**, Schematic of the PC9 cell line model of acquired osimertinib resistance. Cells emerge from a quiescent DTP state before entering a proliferative resistant state. Time points selected for genomics experiments are highlighted in red. **b**, PCA plots of H3K27ac and RAD21 CUT&RUN bigWig signal show that *METTL7A*-KO cells treated with osimertinib fail to exit a drug-naïve-like chromatin state. Individual biological replicates are plotted. Signal is normalized on the basis of CPM, and H2A CUT&RUN signal is subtracted. **c**, Heatmaps of H3K27ac and RAD21 CUT&RUN signal in PC9 cells that were or were not treated with osimertinib. Signal is centered on peaks that were lost, gained or unchanged upon osimertinib treatment. Treatment with osimertinib is associated with gain of both H3K27ac and RAD21 peaks. Depletion of *METTL7A* (M7A) results in reduced H3K27ac and RAD21 binding, resembling the drug-naïve chromatin state. **d**, The PDSSA signal is enriched over METTL7A peaks compared with peaks shuffled over the genome. Significance was calculated through Fisher's exact test ($P < 2 \times 10^{-10}$). **e**, RAD21 signal is enriched over METTL7A peaks compared with randomly shuffled peaks. Significance was calculated through Fisher's exact test ($P < 2 \times 10^{-10}$). **f**, Heatmaps of PDSSA CUT&RUN data in WT METTL7A and METTL7A-KO PC9 cells treated with osimertinib. The signal is centered on peaks that were lost, gained or unchanged upon KO of *METTL7A*. CUT&RUN signal is normalized by CPM, and H2A signal is subtracted. The mean bigWig signal between two biological replicates is shown. **g**, TOP2B CUT&RUN shows an increase in TOP2B intensity in WT cells treated with osimertinib (red box), which is depleted upon KO of *METTL7A*. The CUT&RUN signal is normalized by *E. coli* spike-in and CPM. The mean bigWig signal between two biological replicates is shown. **h-i**, The TOP2B signal is enriched over H3K27ac (**h**) and RAD21 (**i**) peaks gained in WT cells treated with osimertinib. The TOP2B signal is depleted in *METTL7A*-KO cells treated with osimertinib to levels similar to untreated WT cells.

METTL7A-mediated chromatin priming phenotype could be further regulated by TOP2B.

Finally, we examined whether this METTL7A-mediated mechanism directly regulates oncogene amplification by performing *RAF1* DNA FISH in wild-type and *METTL7A*-KO cells exiting the DTP stage.

In wild-type cells, we observed a moderate yet significant increase in *RAF1* copy number in cells treated with osimertinib for 6–8 weeks ($P < 0.0005$). However, we observed no significant increase in *RAF1* copy number in *METTL7A*-KO cells treated with osimertinib compared with untreated cells (Extended Data Fig. 8a,b). These results suggest

that METTL7A facilitates gene amplification as cells acquire resistance to osimertinib. We further probed the effect of METTL7A on copy number by depleting *METTL7A* in PC9-OR cells, which we previously showed re-sensitizes PC9-OR cells to osimertinib (Extended Data Fig. 4i,j). We observed a significant decrease in the number of *RAF1* DNA FISH foci in sh*METTL7A* cells compared with shCTL cells (Extended Data Fig. 8c,d). Finally, we performed WGS and AmpliconArchitect analysis in PC9-OR WT and *METTL7A*-KO cells and observed a global decrease in gene copy number upon *METTL7A* depletion. Together, these results suggest that METTL7A regulates oncogene copy number.

METTL7A is a regulator of chromatin compaction

To understand how METTL7A regulates chromatin conformation during the acquisition of osimertinib resistance, we performed imaging-based, single-cell chromatin tracing of chromosome 22 in PC9 cells during the acquisition of osimertinib resistance (Fig. 5a)³⁹. This technique circumvents the high cell number required for standard Hi-C experiments, which is challenging to obtain when cells are treated with osimertinib, especially in the *METTL7A*-KO background. We performed this experiment in drug-naïve PC9 cells and PC9 cells treated with osimertinib for 6–8 weeks. Because gene amplification had not yet occurred at this time point, the chromatin tracing was not confounded by multiple copies of the same locus.

In wild-type cells, we observed a global decrease in inter-TAD distances in the osimertinib-treated cells compared with parental cells (Fig. 5b and Extended Data Fig. 9a). By contrast, *METTL7A*-KO cells failed to acquire these increased long-range inter-TAD interactions when treated with osimertinib (Fig. 5b), supporting our H3K27ac and RAD21 CUT&RUN results revealing that *METTL7A*-KO cells cannot transition into a drug-resistant chromatin state (Fig. 4b,c). We measured the number of long-range inter-TAD contact events and found that wild-type cells treated with osimertinib developed a greater frequency of long-range inter-TAD interactions than did *METTL7A*-KO cells (Extended Data Fig. 9b). We defined two compartments as A and B, and observed that in wild-type cells, osimertinib treatment led to small changes in compartment designation (Fig. 5c). However, loss of *METTL7A* led to significant changes in compartment scores in both untreated and osimertinib-treated KO cells (Fig. 5c). We quantified the long-range AA, AB, and BB inter-TAD contact frequencies and observed that *METTL7A* KO cells failed to develop long-range AA and AB when treated with osimertinib (Extended Data Fig. 9c).

We next addressed whether there was a correlation between the decrease of inter-TAD distance in osimertinib-treated wild-type cells, METTL7A binding based on our ChIP-seq analysis and the amplification of genomic loci in resistant cells by plotting Chr22 tracing data alongside METTL7A ChIP-seq data and whole-genome sequencing data. We observed that the highest fold change between drug-treated cells and parental cells occurred between TADs 1–10 and TADs 23–25. These regions are of particular interest because these are the loci that eventually become amplified in PC9-OR cells (Fig. 5d). Additionally, the increase of inter-TAD proximity in wild-type cells treated with osimertinib occurred at loci containing the highest density of METTL7A peaks, determined on the basis of our ChIP-seq analysis (Fig. 5d). For example, TADs 3–6 and 24–27 contained the highest density of METTL7A peaks, and these TADs were also the regions that displayed the greatest increase in spatial proximity in wild-type cells treated with osimertinib (Fig. 5d). Together, these data suggest that METTL7A promotes long-range inter-TAD interactions during the acquisition of osimertinib resistance, which could be permissive to the formation and evolution of complex oncogene amplicons.

Discussion

Acquired resistance to TKIs is a major clinical challenge in the treatment of EGFR-mutant LUAD. Oncogene amplification is a hallmark of TKI-resistant LUAD tumors, but the underlying mechanisms are

poorly understood. Here, we identified a unique chromatin signature in drug-naïve tumors that correlates with the boundaries of oncogene amplicons in drug-resistant tumors. We found that CTCF is enriched in drug-naïve tumors over the boundaries of ‘future amplicons’, with a biased enrichment over one side of these amplicons. This finding builds on recent work showing that CTCF deposition affects the copy number and rearrangement of the *KMT2A* gene amplification in leukemia⁴⁰. Although the importance of 3D chromatin organization in driving oncogene expression in cancer has previously been observed¹⁹, our findings have broader implications for the identification of loci that are especially susceptible to oncogene amplification.

Furthermore, we have identified an unexpected function of METTL7A in regulating this chromatin landscape: METTL7A localizes to the nucleus of osimertinib-resistant LUAD cells, where it binds to chromatin to facilitate cohesin-mediated chromatin reorganization. Through the recruitment of PDS5A and the cohesin complex, METTL7A has a chromatin-priming effect; it remodels chromatin architecture to facilitate the future amplification of these oncogenes (Fig. 5e). *METTL7A*-depleted, parental LUAD cells cannot transition into a drug-resistant chromatin state, which we propose is owing in part to decreased long-range inter-TAD chromatin contacts required to form complex oncogene amplicons demarcated by CTCF and cohesin. In *METTL7A*-depleted cells, this mechanism prevents the acquisition of osimertinib-resistant LUAD clones.

During the acquisition of TKI resistance, cells transition through a quiescent, drug-tolerant persister stage, marked by a defined, reversible, epigenetic state. We found that *METTL7A* was specifically upregulated during this time point, before global oncogene amplification. In *METTL7A*-deficient parental cells, we did not notice any cell-viability defects and instead observed impaired cell viability only upon osimertinib treatment. We identified that METTL7A promotes trastuzumab resistance in *HER2*-amplified BT474 cells, which could suggest that METTL7A might more broadly promote resistance to targeted therapies in other oncogene-amplified cancers. Future work should expand this finding to additional targeted therapy models and determine whether *METTL7A* depletion has a phenotype in cancers that do not utilize oncogene amplification as a mechanism of resistance. One limitation of the current study is that we could not obtain WGS data from matched pre- and post-treatment tumor samples from patients, which would be the ideal comparison for assessing *METTL7A*-mediated amplification in drug resistance. Thus, future work should further examine the function of *METTL7A* and the epigenetic priming mechanism in matched tumor samples.

Although the current work primarily focused on the acquisition of resistance, it is important to consider METTL7A’s potential function in the maintenance of drug resistance. We observed a moderate yet significant effect of *METTL7A* depletion on the re-sensitization of resistant cells to osimertinib and a decrease in oncogene copy number in *METTL7A*-depleted, resistant cells. However, it is possible that METTL7A’s function in maintaining drug resistance could be decoupled from its role in regulating oncogene amplification, because previous work has shown that *RAF1* knockdown or MEK inhibition in PC9-OR cells harboring *RAF1* amplification does not re-sensitize resistant cells to osimertinib¹⁵. Future work should examine how and whether METTL7A regulates drug resistance in tumors that have already acquired resistance.

METTL7A has previously been shown to methylate long non-coding RNA⁴¹ and thiol group⁴² substrates, the latter of which has been identified of a mechanism of resistance to other drugs. However, because osimertinib lacks a thiol group, the thiol-methylating activity likely does not contribute to osimertinib resistance. Although we cannot rule out the possibility that additional functions of *METTL7A* could contribute to osimertinib resistance, our work nevertheless has identified an unexpected chromatin- and DNA-binding function of this understudied protein. Future biochemical and structural work will investigate whether *METTL7A* exhibits additional methyltransferase activity toward

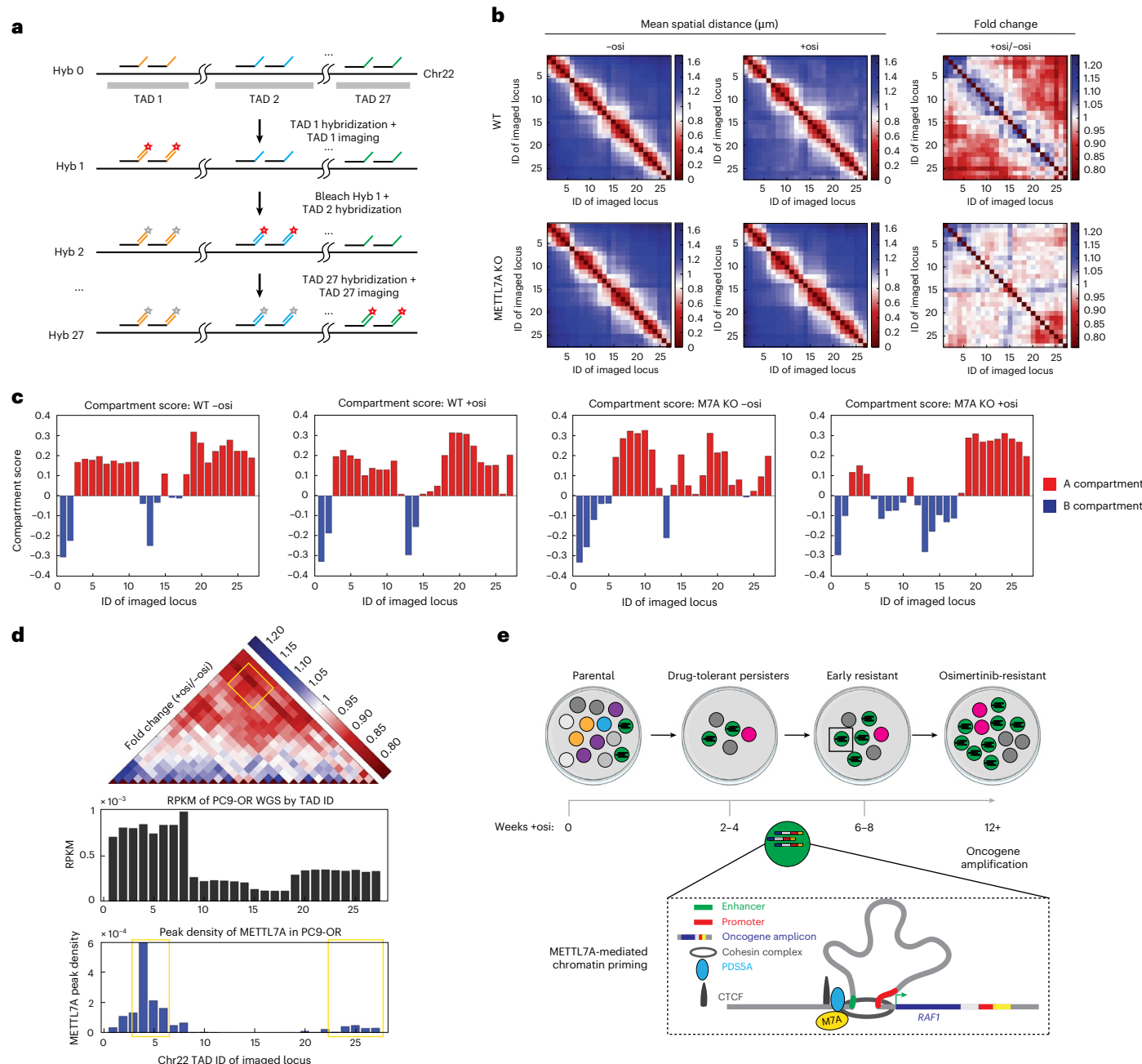


Fig. 5 | METTL7A regulates chromatin architecture. **a**, Schematic of chromosome 22 chromatin tracing. After initial primary probe hybridization (hyb) to 27 TADs along Chr22, unique secondary probes that bind to primaries for each TAD are sequentially hybridized, imaged and bleached. **b**, Chr22 tracing reveals increased inter-TAD interaction in wild-type cells treated with osimertinib. In METTL7A-KO cells, this gain of inter-TAD contacts is absent. **c**, Compartment score profiles of wild-type and METTL7A-KO cells treated with or without osimertinib for 6–8 weeks. **d**, Bar chart showing the WGS coverage (RPKM) in PC9-OR cells in each locus targeted by Chr22 TAD probes and the METTL7A peak density in each TAD on the basis of METTL7A ChIP-seq analysis. **e**, Proposed model of the role of METTL7A during the acquisition of osimertinib resistance. We propose that METTL7A is upregulated as cells acquire resistance to osimertinib. METTL7A localizes to the nucleus, where it binds to amplified oncogenes and affects chromatin architecture through PDS5A-mediated cohesin recruitment, which primes these loci for future gene amplification.

chromatin, and whether its chromatin-binding activity is distinct from its methyltransferase function. Here, we identify a residue, K86, that is crucial for METTL7A's function and chromatin-binding activity. Additionally, METTL7A has homology to METTL7B, which has also been shown to display activity toward small molecules and RNA^{42–44}. Although we did not perform any mechanistic studies with METTL7B, it would be interesting to further explore its potential role in other models of resistance. In summary, we have identified a unique epigenetic priming mechanism regulated by METTL7A that occurs during the acquisition of TKI resistance in EGFR-mutant LUAD and drives oncogene amplification. This work is significant both mechanistically and translationally: METTL7A not only displays a unique chromatin-binding and priming function, but it also lays the groundwork for the development of therapies to prevent TKI resistance. These findings could lead to improved therapeutic strategies to prevent osimertinib resistance from occurring in patients, and future work will further investigate the possibility of targeting METTL7A in LUAD and other tumor types.

Online content

Any methods, additional references, Nature Portfolio reporting summaries, source data, extended data, supplementary information, acknowledgements, peer review information; details of author contributions and competing interests; and statements of data and code availability are available at <https://doi.org/10.1038/s41594-025-01685-4>.

References

1. Nukaga, S. et al. Amplification of EGFR wild-type alleles in non-small cell lung cancer cells confers acquired resistance to mutation-selective EGFR tyrosine kinase inhibitors. *Cancer Res.* **77**, 2078–2089 (2017).
2. Chmielecki, J. et al. Analysis of acquired resistance mechanisms to osimertinib in patients with EGFR-mutated advanced non-small cell lung cancer from the AURA3 trial. *Nat. Commun.* **14**, 1071 (2023).
3. Sequist, L. V. et al. Genotypic and histological evolution of lung cancers acquiring resistance to EGFR inhibitors. *Sci. Transl. Med.* **3**, 75ra26 (2011).
4. Engelman, J. A. et al. MET amplification leads to gefitinib resistance in lung cancer by activating ERBB3 signaling. *Science* **316**, 1039–1043 (2007).
5. Cappuzzo, F. et al. MET increased gene copy number and primary resistance to gefitinib therapy in non-small-cell lung cancer patients. *Ann. Oncol.* **20**, 298–304 (2009).
6. Passaro, A., Jänne, P. A., Mok, T. & Peters, S. Overcoming therapy resistance in EGFR-mutant lung cancer. *Nat. Cancer* **2**, 377–391 (2021).
7. Wu, S. et al. Circular ecDNA promotes accessible chromatin and high oncogene expression. *Nature* **575**, 699–703 (2019).
8. Hung, K. L. et al. ecDNA hubs drive cooperative intermolecular oncogene expression. *Nature* **600**, 731–736 (2021).
9. Kim, H. et al. Extrachromosomal DNA is associated with oncogene amplification and poor outcome across multiple cancers. *Nat. Genet* **52**, 891–897 (2020).
10. Turner, K. M. et al. Extrachromosomal oncogene amplification drives tumour evolution and genetic heterogeneity. *Nature* **543**, 122–125 (2017).
11. Zhu, Y. et al. Oncogenic extrachromosomal DNA functions as mobile enhancers to globally amplify chromosomal transcription. *Cancer Cell* **39**, 694–707 (2021).
12. Nathanson, D. A. et al. Targeted therapy resistance mediated by dynamic regulation of extrachromosomal mutant EGFR DNA. *Science* **343**, 72–76 (2014).
13. Sharma, S. V. et al. A chromatin-mediated reversible drug-tolerant state in cancer cell subpopulations. *Cell* **141**, 69–80 (2010).
14. Deshpande, V. et al. Exploring the landscape of focal amplifications in cancer using AmpliconArchitect. *Nat. Commun.* **10**, 392 (2019).
15. Miguel et al. Mammalian SWI/SNF chromatin remodeling complexes promote tyrosine kinase inhibitor resistance in EGFR-mutant lung cancer. *Cancer Cell* **41**, 1516–1534.e9 (2023).
16. Luebeck, J. et al. Extrachromosomal DNA in the cancerous transformation of Barrett's oesophagus. *Nature* **616**, 798–805 (2023).
17. Roper, N. et al. Clonal Evolution and Heterogeneity of Osimertinib Acquired Resistance Mechanisms in EGFR Mutant Lung Cancer. *Cell Rep. Med.* **1**, 100007 (2020).
18. Roper, N. Functional heterogeneity in MET pathway activation in PDX models of osimertinib resistant EGFR-driven lung cancer. *Cancer Res. Commun.* **4**, 337–348 (2023).
19. Hnisz, D. et al. Activation of proto-oncogenes by disruption of chromosome neighborhoods. *Science* **351**, 1454–1458 (2016).
20. Flavahan, W. A. et al. Insulator dysfunction and oncogene activation in IDH mutant gliomas. *Nature* **529**, 110–114 (2016).
21. Flavahan, W. A. et al. Altered chromosomal topology drives oncogenic programs in SDH-deficient GISTs. *Nature* **575**, 229–233 (2019).
22. Johnstone, S. E. et al. Large-scale topological changes restrain malignant progression in colorectal cancer. *Cell* **182**, 1474–1489 (2020).
23. Xu, J. et al. Subtype-specific 3D genome alteration in acute myeloid leukaemia. *Nature* **611**, 387–398 (2022).
24. Dunham, I. et al. An integrated encyclopedia of DNA elements in the human genome. *Nature* **489**, 57–74 (2012).
25. Luo, Y. et al. New developments on the Encyclopedia of DNA Elements (ENCODE) data portal. *Nucleic Acids Res.* **48**, D882–D889 (2019).
26. Vian, L. et al. The energetics and physiological impact of cohesin extrusion. *Cell* **173**, 1165–1178 (2018).
27. Song, K. et al. Plasticity of extrachromosomal and intrachromosomal BRAF amplifications in overcoming targeted therapy dosage challenges. *Cancer Discov.* **12**, 1046–1069 (2021).
28. Guler, G. D. et al. Repression of stress-induced LINE-1 expression protects cancer cell subpopulations from lethal drug exposure. *Cancer Cell* **32**, 221–237.e13 (2017).
29. Hu, B. et al. ASCL1 Drives tolerance to osimertinib in EGFR mutant lung cancer in permissive cellular contexts. *Cancer Res.* **84**, 1303–1319 (2024).
30. Zehmer, J. K., Bartz, R., Liu, P. & Anderson, R. G. W. Identification of a novel N-terminal hydrophobic sequence that targets proteins to lipid droplets. *J. Cell Sci.* **121**, 1852–1860 (2008).
31. Zehmer, J. K. et al. Targeting sequences of UBXD8 and AAM-B reveal that the ER has a direct role in the emergence and regression of lipid droplets. *J. Cell Sci.* **122**, 3694–3702 (2009).
32. Chen, X. et al. Structural basis for the H2AK119ub1-specific DNMT3A-nucleosome interaction. *Nat. Commun.* **15**, 6217 (2024).
33. Kuenzi, B. M. et al. APOSTL: An interactive galaxy pipeline for reproducible analysis of affinity proteomics data. *J. Proteome Res.* **15**, 4747–4754 (2016).
34. Yu, D. et al. Regulation of cohesin-mediated chromosome folding by PDS5 in mammals. *EMBO Rep.* **23**, e54853 (2022).
35. Losada, A., Yokochi, T. & Hirano, T. Functional contribution of Pds5 to cohesin-mediated cohesion in human cells and *Xenopus* egg extracts. *J. Cell Sci.* **118**, 2133–2141 (2005).
36. Ruiten, M. S. et al. The cohesin acetylation cycle controls chromatin loop length through a PDS5A brake mechanism. *Nat. Struct. Mol. Biol.* **29**, 586–591 (2022).
37. Bsteh, D. et al. Loss of cohesin regulator PDS5A reveals repressive role of Polycomb loops. *Nat. Commun.* **14**, 8160 (2023).
38. Canela, A. et al. Genome organization drives chromosome fragility. *Cell* **170**, 507–521.e18 (2017).
39. Wang, S. et al. Spatial organization of chromatin domains and compartments in single chromosomes. *Science* **353**, 598–602 (2016).
40. Gray, Z. H. et al. Epigenetic balance ensures mechanistic control of MLL amplification and rearrangement. *Cell* **84**, 1303–1319 (2023).
41. Wang, Z. et al. Induction of m6A methylation in adipocyte exosomal lncRNAs mediates myeloma drug resistance. *J. Exp. Clin. Cancer Res.* **41**, 4 (2022).
42. Russell, D. A. et al. METTL7A (TMT1A) and METTL7B (TMT1B) are responsible for alkyl S-thiol methyl transferase activity in liver. *Drug Metab. Dispos.* **51**, 1024–1034 (2023).
43. Maldonato, B. J., Russell, D. A. & Totah, R. A. Human METTL7B is an alkyl thiol methyltransferase that metabolizes hydrogen sulfide and captopril. *Sci. Rep.* **11**, 4857 (2021).
44. Robey, R. W. et al. The methyltransferases METTL7A and METTL7B confer resistance to thiol-based histone deacetylase inhibitors. *Mol. Cancer Ther.* **23**, 464–477 (2023).

Publisher's note Springer Nature remains neutral with regard to jurisdictional claims in published maps and institutional affiliations.

Open Access This article is licensed under a Creative Commons Attribution-NonCommercial-NoDerivatives 4.0 International License, which permits any non-commercial use, sharing, distribution and reproduction in any medium or format, as long as you give appropriate credit to the original author(s) and the source, provide a link to the Creative Commons licence, and indicate if you modified the licensed material. You do not have permission under this licence to share

adapted material derived from this article or parts of it. The images or other third party material in this article are included in the article's Creative Commons licence, unless indicated otherwise in a credit line to the material. If material is not included in the article's Creative Commons licence and your intended use is not permitted by statutory regulation or exceeds the permitted use, you will need to obtain permission directly from the copyright holder. To view a copy of this licence, visit <http://creativecommons.org/licenses/by-nc-nd/4.0/>.

© The Author(s) 2025

Rebecca M. Starble  ^{1,2,3,15}, **Eric G. Sun**  ^{1,2,14,15}, **Rana Gbyli** ^{1,2}, **Jonathan Radda**  ¹, **Jiuwei Lu**  ⁴, **Tyler B. Jensen**  ^{1,2}, **Ning Sun**  ^{1,2}, **Nelli Khudaverdyan** ⁴, **Ting Zhao** ⁵, **Bomiao Hu**  ³, **Mary Ann Melnick** ⁶, **Shuai Zhao**  ^{7,8}, **Nitin Roper** ⁹, **Gang Greg Wang**  ^{7,8}, **Alan J. Tackett** ¹⁰, **Yinsheng Wang** ^{5,11}, **Jikui Song** ⁴, **Katerina Politi** ^{3,6,12}, **Siyuan Wang**  ^{1,13} & **Andrew Z. Xiao**  ^{1,2} 

¹Department of Genetics, Yale School of Medicine, New Haven, CT, USA. ²Yale Stem Cell Center, Yale School of Medicine, New Haven, CT, USA.

³Department of Pathology, Yale School of Medicine, New Haven, CT, USA. ⁴Department of Biochemistry, University of California, Riverside, CA, USA.

⁵Environmental Toxicology Graduate Program, University of California, Riverside, CA, USA. ⁶Yale Cancer Center, New Haven, CT, USA. ⁷Department of Pharmacology and Cancer Biology, Duke University School of Medicine, Durham, NC, USA. ⁸Duke Cancer Institute, Duke University School of Medicine, Durham, NC, USA. ⁹Developmental Therapeutics Branch, Center for Cancer Research, NCI, NIH, Bethesda, MD, USA. ¹⁰University of Arkansas for Medical Sciences, Little Rock, AR, USA. ¹¹Department of Chemistry, University of California, Riverside, CA, USA. ¹²Department of Internal Medicine (Section of Medical Oncology), Yale School of Medicine, New Haven, CT, USA. ¹³Department of Cell Biology, Yale School of Medicine, New Haven, CT, USA.

¹⁴Present address: Tri-Institutional MD-PhD Program, Weill Cornell Medicine, Rockefeller University, Memorial Sloan Kettering Cancer Center, New York, NY, USA. ¹⁵These authors contributed equally: Rebecca M. Starble, Eric G. Sun.  e-mail: andrew.xiao@yale.edu

Methods

Cell culture

PC9 cells were obtained from ATCC; H1975 and HCC827 cells were a gift from K. Politi; and BT474 cells were a gift from Q. Yan. PC9, H1975, HCC827 and BT474 cells were cultured in RPMI-1640 medium (Thermo Fisher, cat. no. 11875119) with 1% penicillin–streptomycin (pen-strep, Thermo Fisher, cat. no. 15140122) and 10% fetal bovine serum. HEK 293T cells were obtained from ATCC (cat. no. CRL-3216) and maintained in DMEM-F12 (Thermo Fisher, cat. no. 11330057) supplemented with 1% pen-strep and 10% FBS. All cells were passaged with 0.25% trypsin (Thermo Fisher, cat. no. 25200056) after reaching 70–90% confluence. PC9-OR, H1975-OR and HCC827-OR were generated by treating parental sensitive cells with escalating doses of osimertinib (Selleckchem, cat. no. S7297) over the course of 12 weeks. Resistant cells were subsequently maintained in 1 μM osimertinib. All cell lines were maintained at 37 °C with 5% CO₂. All cell lines were tested regularly for mycoplasma at the Yale Virology Core.

Colony-formation assay

For the assays performed in Figure 2j, PC9 cells were seeded onto 6-well plates in triplicate with 1,000 cells seeded per well. For all other assays, 20,000 cells were seeded onto each well of a 6-well plate in triplicate. In both cases, one day after seeding, PC9 and HCC827 cells were treated with either 1 μM or 0.1 μM osimertinib, respectively. HCC827 cells were treated with a lower concentration of osimertinib owing to their increased drug sensitivity compared with that of PC9 cells. The medium was changed every 3 days. Osimertinib-treated cells were fixed at the indicated time points with 100% cold methanol for 10 min at –20 °C. Untreated control cells were fixed once cells were confluent. Cells were subsequently stained with crystal violet (0.5% crystal violet in 25% methanol) for 10 min at room temperature and washed with deionized H₂O. Plates were imaged at 800 dots per inch as TIF files. The green channel of each image was isolated and the area of each well was quantified using ImageJ.

For BT474 cells, 3,000 cells were seeded per well in technical and biological triplicates. One day after seeding, trastuzumab was added at a concentration of 10 μg ml⁻¹. The medium was replaced every 2 days for 2 months. Cells were fixed, stained and imaged as described above.

Cell viability assay

Cells were seeded onto 96-well plates in technical triplicate, with 1,000 cells (PC9 and H1975) or 1,500 cells (HCC827) per well. Twenty-four hours after seeding, osimertinib was added at the indicated concentrations. Four days after seeding, cells were fixed for 15 min in 4% formaldehyde and washed two times with PBS. Hoechst (Thermo Fisher, cat. no. H3570) was added at a final concentration of 1 μg ml⁻¹. Plates were imaged using Cytaction 3 (BioTek), and CellProfiler was used to quantify the number of cells per well. Percentage viability was calculated by normalizing to the lowest concentration of osimertinib (100% viability).

Lentivirus production

293T cells were seeded into 10-cm dishes. Upon reaching 80–90% confluence, cells were transfected with 10 μg packaging plasmid (psPAX2, Addgene 12260), 2 μg envelope plasmid (PM2.6, Addgene 12259) and 10 μg expression vector using the jetPRIME DNA and siRNA Transfection Reagent (Polyplus), according to the manufacturer's instructions. Virus was collected 48–72 h post-transfection and filtered through a 0.45-μm filter. Virus was concentrated using the Lenti-X Concentrator kit (Takara Biosciences), according to the manufacturer's instructions, and resuspended in PBS.

Generation of METTL7A KO clones

METTL7A guide RNAs were designed using the Benchling CRISPR tool. Single guide RNAs were designed to target the following two sites (5'→3'): TGTGATATAACGAAACAGA and CCTCGCGGAGAACCTCGCTCC.

Single guide RNAs were cloned into a lentiviral CRISPR–Cas9 plasmid (Addgene cat. no. 52963), using the BbsI restriction digest method from the Zhang lab⁴⁵. Lentivirus was prepared as described above. Cells were transduced with lentivirus and underwent selection for 10–14 days with puromycin (Thermo Fisher cat. no. A1113803). Cells were then single-cell sorted into 96-well plates using a FACS AriaII. Individual clones were screened for homozygous knock out through genotyping using primers METTL7A_GT_F and METTL7A_GT_R, Sanger sequencing and RT-qPCR for METTL7A using primers METTL7A_RNA_F, METTL7A_RNA_R, actin-F and actin-R (Supplementary Table 4).

shRNA-mediated gene knockdown

Cells with shRNA-mediated gene knockdown were created by lentiviral transduction using the PLKO.1 backbone. shRNA lentiviruses were produced by the Yale Functional Genomics Core facility by cotransferring HEK293T cells with packaging vectors psPAX2 (Addgene plasmid cat. no. 12260) and pMD2.G (Addgene plasmid cat. no. 12259) together with lentiviral transfer constructs. Viral supernatant was collected 48 h and 72 h after transfection and filtered with a 0.45-μm filter. Cells were infected with filtered viral supernatant diluted 1:5 in growth medium. Two days after infection, cells were selected with 1 μg ml⁻¹ puromycin (Thermo Fisher cat. no. A1113803). Selection was performed for at least 10 days before downstream analysis. The following shRNAs from the The RNAi Consortium (TRC) were used: TRCN0000197115 (RAF1), TRCN0000195502 (RAF1), TRCN0000121248 (MET), TRCN0000121233 (MET), TRCN0000240738 (METTL7A) and SHC002 (non-targeting control).

DNA FISH probe design

Oligopaint FISH probe libraries were constructed as previously described⁴⁶. Each oligonucleotide is 100 nucleotides (nt) long, with 30-nt homology to the genome. Individual FISH probes were generated by PCR amplification, in vitro transcription and reverse transcription. DNA secondary probes that were conjugated with either Alexa Fluor 488, Alexa Fluor 594 or Alexa Fluor 647 were used in FISH experiments to the unique secondary sequence for each library subpool.

The following Oligopaint-covered genomic regions (hg19) were used: chr3, 12,621,717–12,721,700 (hg19_RAF1_100kb); chr3, hg19, 20,505,612–22,005,610 (hg19_Landmark_Chromosome_3_1.5 Mb); chr20, 58,425,276–58,525,044 (hg19_SYCP2_100kb); chr20, chr20, 51,500,001–53,000,000 (hg19_Landmark_Chromosome_20_1.5 Mb); chr8, 128,730,038–128,833,605 (hg19_MYC_100kb); chr8, 116,860,000–118,680,000 (hg19_Landmark_Chromosome_8_1.5 Mb); chr7, 116,350,000–116,450,000 (hg19_MET_100kb); chr7, 55,135,000–55,235,000 (hg19_EGFR_100kb); chr7, 89,500,000–91,000,000 (hg19_Landmark_Chromosome_7_1.5 Mb); chr3, hg19, 12,366,001–12,866,000 (hg19_RAF1_500kb). Single-stranded DNA oligonucleotide pools were ordered and synthesized from GenScript.

Interphase DNA FISH

Cells were fixed in 4% PFA for 10 min, washed with PBS and permeabilized in 0.5% Triton X-100 for 30 min. DNA was denatured with 0.1 M HCl for 5 min. Samples were treated with 20 μl of RNase A/T1 (Thermo Fisher, cat. no. EN0551) for 40 min at 37 °C. Cells were washed twice with 2× SSC and incubated for 30 min in pre-hybridization buffer: 2× SSC + 0.1% Tween20 + 50% (vol/vol) formamide (Millipore Sigma, F9037). Then, 200 ng FISH probes were diluted in 10 μl hybridization buffer: 2× SSC, 50% formamide, 20% dextran sulfate (EMD Millipore, cat. no. S4030). The coverslip was denatured at 86 °C for 5 min. Samples were incubated with primary probe at 37 °C for 16 h in a humidified chamber. Samples were then washed twice for 15 min in 2× SSCT at 60 °C and once with 2× SSCT for 15 min at room temperature. Samples were then incubated with secondary probes (2 μM fluorescently conjugated secondary probe diluted in 30% formamide + 2× SSC) for 30 min at room temperature. Coverslips were washed with 40% formamide in 2× SSC for 5 min, followed by additional washes in 2× SSC. Coverslips

were then mounted in Prolong Gold Antifade Mountant with DAPI. CellProfiler was used to quantify interphase FISH images.

Metaphase DNA FISH

Cells in metaphase were prepared by KaryoMAX (Gibco) treatment at $0.1\text{ }\mu\text{g ml}^{-1}$ for 3 h. The single-cell suspension was then collected and washed by PBS, and treated with 75 mM KCl for 15 min. Samples were then fixed in 3:1 methanol to glacial acetic acid (vol/vol) and washed once with the fixative. Samples were stored at $-20\text{ }^\circ\text{C}$ before use. Cells were then dropped onto slides and heated for 1 min at $86\text{ }^\circ\text{C}$. Slides were equilibrated with 2 \times SSC for 5 min and DNA FISH was performed using the same protocol as interphase DNA FISH.

Microscopy

Images were acquired on a Leica SP5, Zeiss LSM 880 or Leica Stellaris at either $\times 40$ or $\times 63$ for interphase FISH samples. For metaphase FISH samples, images were acquired at $\times 100$. All images were taken as Z-stacks at either $0.5\text{-}\mu\text{m}$ steps or optimized steps depending on the pinhole size. Z-stack images were further processed as maximum intensity projection images in ImageJ/FIJI and analyzed in CellProfiler or ImageJ/FIJI.

Whole-genome sequencing

Library preparation and sequencing was performed by Novogene. One microgram of gDNA was sheared, and fragments were end-repaired, A-tailed and ligated with Illumina adapters. Size selection was performed, followed by PCR amplification and purification. The resulting library was analyzed with Qubit, RT-PCR and bioanalyzer. Libraries were then pooled and loaded onto an S4 flowcell and sequenced with NovaSeq 6000 with $\times 10$ genomic coverage per sample.

AmpliconArchitect and AmpliconClassifier

WGS FASTQ files were processed using the AmpliconSuite-pipeline v0.1555.2 to call AmpliconArchitect v1.3.r5, AmpliconClassifier v0.5.3, and CNVKit v0.9.10 against GRCh38, using GRCh38 as the reference genome with default settings. Amplicon complexity scores, which measure the diversity of amplicons, were retrieved from the output of AmpliconClassifier. To perform grouped analysis in paired sensitive and resistant cells, GroupedAnalysis.py was run.

Patient-derived xenograft sample processing

Viable tumors or single-cell suspensions of PDXs were provided by the NCI CAPR, which were derived from tumors that progressed on osimertinib treatment from [NCT02759835](#). DNA and RNA were isolated from approximately 30 mg of tissue using the All Prep DNA/RNA Mini Kit (Qiagen).

Whole-exome sequencing analysis of oncogene amplification

BAM files were retrieved from dbGaP accession code [phs002001](#). CNVKit v0.9.9 was used to analyze copy-number variation between tumors that had been treated with osimertinib and tumors before osimertinib treatment. The pre-treated sample was input using the -normal flag. The -target flag was the S06588914_Regions.bed file provided by Agilent, as the original patient samples were processed using the SureSelect Clinical Research Exome Kit. The -annotate flag was provided from UCSC as refFlat.txt for hg19. Reads per kilobase per million mapped reads (RPKM) values for RNA-seq were retrieved from the supplemental information of Roper et al.¹⁷. To produce the graphs in Extended Data Figure 2, amplified oncogenes, with the cut-off provided in Supplementary Table 2, were used. Oncogenes were retrieved from the supplemental information of Luebeck et al.¹⁶.

RNA sequencing

RNA was extracted using the RNeasy Mini Kit (Qiagen, cat. no. 741040), and concentrations were measured using Nanodrop. Library preparation was performed using approximately 1 μg of RNA. Library

preparation and sequencing were performed by Novogene. mRNA was purified from total RNA with poly-T oligonucleotide-attached magnetic beads. Fragmentation was performed and the first strand cDNA was synthesized with random hexamer primers, followed by second-strand cDNA synthesis. cDNA was then subject to end repair, A-tailing, adapter ligation, size selection, PCR amplification and purification. Qubit and RT-PCR were used to quantify resulting libraries, and bioanalyzer analysis was performed to determine size distribution. Libraries were pooled and loaded onto an S4 flowcell and sequenced with NovaSeq 6000.

RNA-seq analysis

Sequencing reads were aligned with STAR version 2.7.7a using a GRCh38 STAR index. Gene expression was quantified using featureCounts from Subread version 2.0.3. DESeq2 was used for differential analysis. To profile differentially expressed putative and known epigenetic factors, the GSEA database was used to search for epigenetic gene lists. A single list of known or putative epigenetic and/or chromatin factors was curated by combining GSEA lists: 'REACTOME_EPIGENETIC_REGULATION_OF_GENE_EXPRESSION,' 'GOMF_TRANSFERASE_ACTIVITY,' 'GOMF_DOUBLE_STRANDED_METHYLATED_DNA_BINDING,' and 'GOBP_NEGATIVE_REGULATION_OF_GENE_EXPRESSION_EPIGENETIC.'

ChIP-seq

ChIP-seq was performed using the Active Motif ChIP-IT Express Kit (Active Motif 53008) according to the manufacturer's instructions. Approximately 2×10^7 cells were used per replicate. Chromatin was sheared using a Covaris S220 (peak power: 175 W, duty factor: 10%, 200 cycles/burst, 160 seconds/run). One μL of de-crosslinked chromatin was analyzed via Agilent TapeStation to determine fragment size, and DNA concentration was measured using Qubit (Invitrogen Q32854). The following antibodies were used: IgG isotype control (CST 5415S) and c-MYC-tag (Cell Signaling Technologies 2276S). 20 μg of chromatin was pre-incubated with antibody overnight at $4\text{ }^\circ\text{C}$. Protein G beads were subsequently added to antibody-bound chromatin and incubated for 4 h at $4\text{ }^\circ\text{C}$. 2.5 ng of immunoprecipitated chromatin was subject to library preparation using EpiCypher CUT&RUN Library Kit (EpiCypher 141001) according to the manufacturer's instructions. Pooled libraries were sequenced by Novogene with NovaSeq 6000 with 20 million paired-end reads sequenced per library.

ChIP-seq analysis

Adapter sequences from paired-end sequencing reads were trimmed with Trimmomatic, and quality control was performed using FastQC. Bowtie2 v2.4.2 was used to align reads to the GRCh37 genome (-very-sensitive flag, one mismatch allowed). SAMtools v1.16 was used to remove unmapped reads, secondary alignment reads and reads with a Phred score of <30. Macs2 v2.2.7.1 was used to call peaks with default peak-calling settings. Peaks were called against input chromatin. Peaks from two biological replicates were merged. To account for the presence of amplicons in OR cells, we were stringent with our peak-calling and called peaks against both ChIP input and IgG samples, thus normalizing for changes in copy number. Additionally, we normalized our data to PC9-OR and HCC827-OR wildtype cells that did not express the METTL7A-MYC-FLAG fusion protein. DeepTools v3.5.1 was used for ChIP-seq data visualization. Plots depicting ChIP-seq signal were generated by using DeepTools bamCoverage to normalize signal by CPM, and duplicates were ignored. Peak intersections were performed using BEDTools v2.30 and quantified using BEDTools Fisher. The mean bigWig signal between biological replicates was plotted.

GO analysis

ChIP-seq peaks were annotated to the nearest gene using ChIP-seeker, and promoter peaks were filtered before running EnrichR

(<https://maayanlab.cloud/Enrichr/>). The top five significant terms ranked by *P* value from ENCODE and ChEA Consensus TFs from ChIP-X were plotted.

MEME analysis

FASTA sequences were generated using the center of ChIP-seq peaks with flanking windows of 250 bp (total window size, 500 bp). Enriched motifs were identified using MEME v5.4.1 meme-chip. The top three STREME outputs, ranked by *P* value, were visualized in R using universalmotif v3.15.

CUT&RUN

CUT&RUN was performed using the CUTANA ChIC/CUT&RUN Kit (EpiCypher 141048), according to the manufacturer's instructions. Approximately 5×10^5 cells were used per reaction. Antibodies to histone H2A (CST cat. no. 12349), PDS5A (Thermo Fisher cat. no. PA5-57755), RAD21 (Active Motif cat. no. 91245), H3K27ac (CST cat. no. 8173), TOP2B (Abcam cat. no. ab72334) and IgG (EpiCypher cat. no. 13-0042) were used. One microliter of chromatin was analyzed using Agilent TapeStation to determine fragment size. DNA concentration was measured using Qubit (Invitrogen Q32854). Library preparation was performed using the CUTANA CUT&RUN Library Prep Kit (EpiCypher 14-1001) using 2.5 ng chromatin as input. Pooled libraries were sequenced by Novogene with NovaSeq with 20 million paired-end reads sequenced per library.

CUT&RUN analysis

Adapter sequences from paired-end sequencing reads were trimmed with Trimmomatic, and quality control was performed using FastQC. Bowtie2 v2.4.2 was used to align reads to GRCh37 (–very-sensitive flag, one mismatch allowed). SAMtools v1.16 was used to remove unmapped reads, secondary alignment reads and reads with a Phred score of <30. Macs2 version 2.2.7.1 was used to call peaks with default peak-calling settings. Peaks were called against H2A. IgG peaks were subtracted from BED files using BEDTools v2.30. IDR was used to determine significant peaks between two biological replicates. DeepTools v3.5.1 was used for data visualization. CUT&RUN signal plots were generated using DeepTools bamCompare, normalizing by CPM and relative to H2A, with duplicates excluded. In all plots, the mean normalized bigWig signal between two biological replicates is plotted. Peak intersections were identified using BEDTools v2.30 and quantified with BEDTools Fisher.

For TOP2B CUT&RUN, owing to higher levels of noise in the sequencing data, SEACR was used to call peaks. bigWig signal was normalized via *E. coli* spike-in DNA, and normalized bigWig signals were used as inputs for SEACR using the 'stringent' settings. BEDTools was used to intersect peaks between biological replicates. Downstream visualization with DeepTools was performed as previously described.

Subcellular fractionation and protein immunoprecipitation

Approximately 2×10^7 wild-type and METTL7A-MYC-FLAG-tag-expressing cells were subject to subcellular fractionation using the Subcellular Fractionation Kit for Cultured Cells (Thermo Fisher cat. no. 78840). The protein concentration of each fraction was measured with a BCA assay (Pierce 23225). Anti-FLAG magnetic beads (Millipore cat. no. M8823) were washed three times with TBS buffer (50 mM Tris-HCl pH 7.4, 150 mM NaCl), and 30 µl of bead slurry was added to 500 µg of nuclear lysate diluted in 1 ml TBS. Nuclear lysates were incubated with beads for 2 h at 4 °C. Beads were spun down and subsequently washed with TBS buffer at 4 °C three times for 10 min. Immunoprecipitated proteins were eluted by incubating beads twice for 30 min with 150 ng µl⁻¹ FLAG peptide at 4 °C. Eluted proteins were subjected to mass spectrometry (MS) analysis. Two biological replicates were performed for each sample.

Mass spectrometry

MS was performed by the IDeA National Resource for Quantitative Proteomics in Little Rock, Arkansas, with the following procedure:

protein samples were reduced, alkylated and digested using filter-aided sample preparation⁴⁷ with sequencing grade modified porcine trypsin (Promega). Tryptic peptides were then separated by reverse-phase XSelect CSH C18 2.5-µm resin (Waters) on an in-line 150 × 0.075 mm column using an UltiMate 3000 RSLC nano system (Thermo). Peptides were eluted using a 60-min gradient from 98:2 to 65:35 buffer A:B ratio (buffer A, 0.1% formic acid, 0.5% acetonitrile; buffer B, 0.1% formic acid, 99.9% acetonitrile). Eluted peptides were ionized by electrospray (2.4 kV) followed by MS analysis on an Orbitrap Eclipse Tribrid mass spectrometer (Thermo). MS data were acquired using the FTMS analyzer in profile mode at a resolution of ×120,000 over a range of 375 to 1,200 *m/z*. Following HCD activation, tandem MS data were acquired using the ion trap analyzer in centroid mode, with a normal mass range with a normalized collision energy of 30%. Proteins were identified by database search using MaxQuant (Max Planck Institute) with a parent ion tolerance of 3 p.p.m. and a fragment ion tolerance of 0.5 Da. Scaffold Q + S (Proteome Software) was used to verify peptide and protein identifications. Protein identifications were accepted if they had a false discovery rate below 1.0% and contained at least two identified peptides. Protein probabilities were assigned by the Protein Prophet algorithm⁴⁸.

Mass spectrometry analysis

Analysis of MS hits was performed with the SAINTExpress/APOSTL pipeline. A samples report was generated from Scaffold using the following parameters: protein threshold, 99%; minimum number of peptides, 1; peptide threshold, 95%. Known contaminants such as keratin were manually removed. The samples report, containing two biological replicates for each sample, was then uploaded to the APOSTL Galaxy Server. Wild-type cells not expressing the METTL7A-MYC-FLAG fusion protein were set as negative controls. The CRAPome was queried to exclude known contaminants from analysis. Thresholds were set by using a SAINT score > 0.5 and log₂FC > 2.

Immunoprecipitation and western blot validation of mass spectrometry

To validate MS hits, nuclear lysates were prepared through the Dignam and Roeder method⁴⁹. Nuclear lysates were quantified with BCA assay, and 300 µg protein was diluted in 400 µl PBS with protease inhibitors. To validate endogenous METTL7A interactors, nuclear lysates were prepared via the Thermo NE-PER Nuclear and Cytoplasmic Extraction kit. Nuclear lysates were quantified with BCA assay, and 200 µg protein was diluted in 400 µl PBS + 0.1% BSA with protease inhibitors. Lysates were pre-incubated with antibodies overnight at 4 °C. Antibodies to IgG (CST cat. no. 541SS), FLAG (Sigma cat. no. F1804), MYC-tag (CST cat. no. 2276S) and METTL7A (OTI4B10, Thermo cat. no. TA809878) were used. Dynabeads M-280 Sheep anti-mouse-IgG (Invitrogen cat. no. 11201D) were washed three times with PBS + 0.1% BSA, and 50 µl bead slurry was added to each antibody-lysate mixture. Lysates were incubated with beads for 2 h at 4 °C. Beads were washed three times for 5 min each with PBS + 0.1% BSA and eluted with 2× Laemmli buffer + BME by boiling for 5 min at 95 °C.

Chromatin tracing

The design of a chromatin-tracing library targeting each of 27 TADs of chromosome 22 (Chr22) was previously described³⁹, and this library was amplified using the same method as that for the interphase DNA FISH probes⁴⁶. Primary hybridization of Chr22 probes was performed as described (see 'Interphase DNA FISH'). Sequential imaging was performed with a custom microscope and microfluidics setup⁴⁶. All images were acquired as multi-color Z-stacks, including consecutive imaging of Alexa Fluor 647 dyes (first 14 TADs of Chr22), ATTO 565 dyes (last 13 TADs of Chr22) and yellow-green fiducial beads for sequential image alignment at each Z-step. Images were acquired with 0.5 sec of exposure per channel per Z-plane, using a 200-nm Z-step size and

50 total Z-steps (10 μm total image depth). FISH signals were removed between rounds of sequential hybridization and imaging by 50 sec of simultaneous illumination in the 647-nm and 560-nm color channels, as previously detailed^{39,46}. Image analysis and chromatin trace assembly were performed using the MinaAnalyst package, available at <https://campuspress.yale.edu/wanglab/mina-analyst/>.

Analysis of chromosome compaction

We calculated the inter-TAD distances between all pairs of TADs on chr22 for each cell type, and generated mean inter-TAD distance matrix by calculating the mean distance between each pair of TADs. To quantify the decompaction score, we performed two-sided Wilcoxon signed rank test between the mean inter-TAD distances between untreated and osimertinib-treated cells and calculated FDR and fold change values, as previously described⁵⁰.

Determination of A and B compartment identity of TADs

We assigned TADs to A and B compartments using a previously published algorithm³⁹. In brief, we fitted a power-law function to the data points of the mean inter-TAD spatial distances versus their genomic distances across chromosome 22, which yielded the expected inter-TAD spatial distance for each pair of TADs, according to their genomic distance. We then normalized the observed mean inter-TAD spatial distance by the expected spatial distance, yielding a normalized inter-TAD distance matrix. We then calculated the Pearson correlation coefficient between each pair of rows and columns in this matrix, generating a Pearson correlation matrix. We next applied principal-component analysis to the Pearson correlation matrix, and took the coefficients of the first principal component as compartment scores. The compartment score profiles were validated with published ChIP-seq profiles in PC9 cells such that the compartment A regions are enriched in active histone modifications, gene density and DNaseI accessibility. The following published ChIP-seq datasets from the ENCODE Project were used: ENCFF364RGE, ENCFF406PHZ and ENCFF605RZQ.

Analysis of long-range contact in A and B compartments

A long-range contact is defined when two non-adjacent TADs were less than 500 nm apart from each other. We quantified the number of long-range contact events across all inter-TAD pairs and used the A and B compartments identities to further quantify the number of AA, AB and BB long-range TAD contact events. The Wilcoxon rank-sum test was used to calculate statistical significance.

RPKM and peak density analysis

BAM files were converted to bed files using bamtobed from bedtools. Bedtools coverage was run with -a set to the BED file containing TAD coordinates and -b set to the BED file of the sequencing sample. METTL7A peak density was calculated by identifying peaks on chromosome 22 that belong to a particular TAD ID, summing the signalValue of peaks within such TAD ID, and normalizing the sum to the length of the TAD ID. RPKM and peak density were visualized in Matlab R2022b.

Immunofluorescence

Cells were fixed with 4% paraformaldehyde, washed three times with PBST (PBS + 0.1% Tween-20) and permeabilized for 20 min with PBS-Tx (PBS + 0.2% Triton X-100). Blocking was performed for 1 h (PBST + 2% BSA). Samples were incubated with primary antibody overnight at 4 °C in blocking buffer using the following antibodies: anti-MYC-tag 1:1,000 (CST 2276S). Cells were washed three times with PBST and incubated with secondary antibody (1:1,000) for 1 h at room temperature using the following secondary antibodies: Alexa-Fluor-488-conjugated goat anti-mouse-IgG (Thermo Fisher, cat. no. A-11001) or Alexa-Fluor-568-conjugated goat anti-mouse-IgG (Thermo Fisher, cat. no. A-11031). Cells were washed with PBST and mounted in mounting medium containing DAPI.

Proximity ligation assay

Cells were fixed in 4% paraformaldehyde, washed three times in PBS and permeabilized for 20 min with PBS-Tx (PBS + 0.2% Triton X-100). Blocking was performed for 1 h in PBST + 2% BSA. Samples were incubated with primary antibody overnight at 4 °C in blocking buffer using the following antibodies: anti-MYC-tag 1:1,000 (CST cat. no. 2276S), PDSSA1:500 (Thermo Fisher cat. no. PA5-57755), Rad21:1,000 (Active Motif cat. no. 91245). Cells were washed three times with PBST. The PLA was performed using the Duolink In Situ Red Starter Kit Mouse/Rabbit (Millipore DUO92101-1KT).

RT-qPCR

RNA was extracted using the RNeasy Mini Kit (Qiagen, cat. no. 741040). One microgram of RNA was reverse transcribed into cDNA using the iScript cDNA Synthesis Kit (BioRad cat. no. 1708890). Each qPCR consisted of 5 ng cDNA, 1× iQ SYBR Green Supermix (BioRad cat. no. 1708880) and 300 nM forward and reverse primers. Relative expression was calculated using the $2^{-\Delta\Delta C_t}$ method relative to actin using the average values from three technical replicates. Each experiment was performed in biological triplicate. Primer sequences are listed in Supplementary Table 4.

Immunoblotting

Approximately 2×10^6 cells were lysed with RIPA buffer (Thermo Fisher cat. no. 89900) for 15 min on ice. Lysate was clarified by centrifugation at top speed for 30 min at 4 °C. Protein concentration was quantified via BCA assay. Approximately 20 μg of protein was mixed with 1× Laemmli buffer (BioRad cat. no. 1610747) and 10% BME, boiled for 5 min and loaded onto a 4–20% polyacrylamide gel. Electrophoresis was performed at 100 V for approximately 90 min. Gels were then transferred onto a PVDF membrane at 90 V for 90 min in transfer buffer. Blots were blocked for 1 h at room temperature in blocking buffer (5% milk in TBST (1× TBS, 0.5% Tween-20)) and incubated overnight at 4 °C with primary antibodies diluted in blocking buffer. The following primary antibodies were used: anti-FLAG M2 (1:1,000; Sigma cat. no. F1804), anti-FLAG (1:1,000; Sigma cat. no. F7425), anti-MYC-tag (1:1,000, CST cat. no. 2276S), METTL7A (1:1,000; OTI4B10, Thermo cat. no. TA809878), histone H3 (CST cat. no. 4499), PDSSA (Thermo Fisher, cat. no. PA5-57755), lamin B1 (1:1,000; Proteintech cat. no. 66095-1), calnexin (1:1,000; CST cat. no. 2679), alpha-tubulin (CST cat. no. 2144S), CoxIV (Abcam cat. no. ab16056), cRAF (1:1,000; CST cat. no. 53745) and MET (1:1,000; CST cat. no. 4560). Blots were washed 3×5 min in TBST and incubated with secondary antibody (CST cat. no. 7074P2 or 7076P2) diluted in blocking buffer for 1 h at room temperature. Blots were washed 3×5 min with TBST and visualized with SuperSignal Western Femto (Thermo cat. no. 34096).

Protein expression and purification

DNA encoding human METTL7a was inserted into a modified vector preceded by an amino-terminal hexahistidine(His₆)-MBP tag and a TEV cleavage site. BL21(DE3) RIL cells expressing the plasmids were induced by addition of 0.13 mM isopropyl β-D-1-thiogalactopyranoside (IPTG) when the cell density reached an absorbance at 600 nm of 1.1 and were grown at 16 °C overnight. The cells were harvested and lysed in buffer containing 50 mM Tris-HCl (pH 8.0), 1 M NaCl, 25 mM Imidazole, 10% glycerol and 1 mM PMSF. Subsequently, the fusion proteins were purified through a nickel column and size-exclusion chromatography. The purified protein samples were concentrated in 20 mM Tris-HCl (pH 7.5), 100 mM NaCl, 5% glycerol and 5 mM DTT and stored at -80 °C. For positive control of DNA-binding assay, human DNMT3A (residues 281–912) and full-length DNMT3L were purified as previously described⁵⁰.

Electrophoretic mobility shift assay

For this assay, 0.04 μM of 60 nt DNA (ATTCTTCCGAGTTTTTC-CTCATCTCACTTCCAATACAGAAAGCTTGCCCCGCCCTTCCT

and duplex (upper strand: ATTCTTCCGAGTTTTCTCATCT-CACTTCCAATACAGAAAGCTTGGCCGCCCTCCT; lower strand: AGGAAGGGCGGGCAAGCTTCTGTATTGGAAGTGAGATGAG-GAAAAAACTCGGAAGAAT) was titrated with MBP-tagged METTL7A ranging from 0 to 0.8 μ M in the 10- μ l reaction mixture with the binding buffer containing 20 mM Tris-HCl (pH 7.5), 50 mM NaCl, 5% glycerol and 5 mM DTT. Samples were incubated on ice for 20 min and then resolved on a 5% wt/vol polyacrylamide gel (59:1 acrylamide: bis(acrylamide)), which was run at 100 V using 0.2 \times TBE (pH 8.3) running buffer for 50 min at 4 °C. The gel was stained with SYBR Gold (Thermo) and visualized by ChemiDoc Imaging System (BioRad). The bound ratio (fraction bound = bound / (bound + unbound)) from the band intensities for the free and protein-bound forms was quantified by using ImageJ. The dissociation constant (K_d) was obtained by plotting the bound ratio versus protein concentration and fitting the curve to the Hill equation (fraction bound = (protein concentration) h / ((K_d) h + (protein concentration) h) where h is the Hill coefficient using GraphPad Prism 10.

Reporting summary

Further information on research design is available in the Nature Portfolio Reporting Summary linked to this article.

Data availability

WGS has been deposited under [PRJNA1065471](#). RNA-seq, ChIP-Seq and CUT&RUN have been deposited in GEO database under accession number [GSE254521](#). Source data are provided with this paper.

References

45. Sanjana, N. E., Shalem, O. & Zhang, F. Improved vectors and genome-wide libraries for CRISPR screening. *Nat. Methods* **11**, 783–784 (2014).
46. Liu, M. et al. Chromatin tracing and multiplexed imaging of nucleome architectures (MINA) and RNAs in single mammalian cells and tissue. *Nat. Protoc.* **16**, 2667–2697 (2021).
47. Wiśniewski, J. R., Zougman, A., Nagaraj, N. & Mann, M. Universal sample preparation method for proteome analysis. *Nat. Methods* **6**, 359–362 (2009).
48. Nesvizhskii, A. I., Keller, A., Kolker, E. & Aebersold, R. A Statistical Model for Identifying Proteins by Tandem Mass Spectrometry. *Anal. Chem.* **75**, 4646–4658 (2003).
49. Carey, M. F., Peterson, C. L. & Smale, S. T. Dignam and Roeder Nuclear Extract Preparation. *Cold Spring Harb. Protoc.* **2009**, pdb. prot5330 (2009).
50. Liu, M. et al. A genome-wide single-cell 3D genome atlas of lung cancer progression. *Nat. Genet.* <https://doi.org/10.1038/s41588-025-02297-w> (2025).

Acknowledgements

We thank C. Calderwood at the Yale Functional Genomics Core for help producing shRNA lentiviruses. We are grateful to P. Mischel, who generously provided COLO320-HSR and COLO320-DM cells for use in this study. We thank B. Bernstein for depositing PC9 CTCF, H3K9me2, and H3K9me3 ChIP-seq datasets to ENCODE, which were used in this study, and to E. Aiden for depositing PC9 Hi-C data to ENCODE. We thank T. Ardito and J. Wolenski for imaging support, R. Elmeskini

and Z. Weaver Ohler from NCI Center of Advanced Preclinical Research (CAPR) for PDXs, N. Neuenkirchen for biochemistry support, M. Liu for chromosome tracing analyses, members of the Xiao lab for feedback, and the Yale Center for Research Computing for computational support. R.M.S. was supported by the NSF GRFP and 5T32HD007149-43. E.G.S. was supported by the Yale Hahn Scholars Fellowship. A.Z.X. was partly supported by NIH (R35GM136346). This work is supported by a DRP to A.Z.X. from the Yale Lung SPORE (P50CA196530). A.T. is supported by R24GM137786. S.W. was partly supported by NIH (R01HG011245, DP2GM137414, R01CA292936). J.S. was supported by NIH R35GM119721. Y.W. was supported by the National Institutes of Health (R35 ES035717). J.R. was partly supported by NIH Predoctoral Training Grant (2T32GM007499). G.G.W. was supported by NIH 1 R01 CA271603.

Author contributions

R.M.S. and A.Z.X. conceptualized and designed experiments. R.M.S. and E.G.S. performed imaging, sequencing, and cell proliferation and viability experiments and analyses. R.M.S., R.G., J.L. and N.K. performed biochemical experiments. E.G.S., J.R. and T.J. designed FISH and chromatin tracing probes. J.R. and R.M.S. performed chromatin tracing experiments. N.S. produced METTL7A-KO cells. N.R. generated PDXs used in Fig. 1 and Extended Data Figs. 2–3. B.H. and M.A.M. generated PDXs and PDX RNA-seq data used in Fig. 2. A.T., T.Z. and Y.W. performed mass spectrometry. S.Z. and G.G.W. provided biochemistry guidance designing METTL7A mutants. J.S., K.P., S.W. and A.Z.X. supervised the study. R.M.S., E.G.S. and A.Z.X. wrote the paper with insights from all co-authors. The funders had no role in study design, data collection and analysis, decision to publish or preparation of the manuscript.

Competing interests

K.P. has grants from AstraZeneca, Roche/Genentech, Boehringer Ingelheim and D2G Oncology; personal fees from AstraZeneca and Revelio Therapeutics, Inc; and a patent related to EGFR T790M mutation testing with royalties paid “from MSKCC/MolecularMD”. K.P. is a co-founder of and consultant for Revelio Therapeutics, Inc. All other authors declare no competing interests.

Additional information

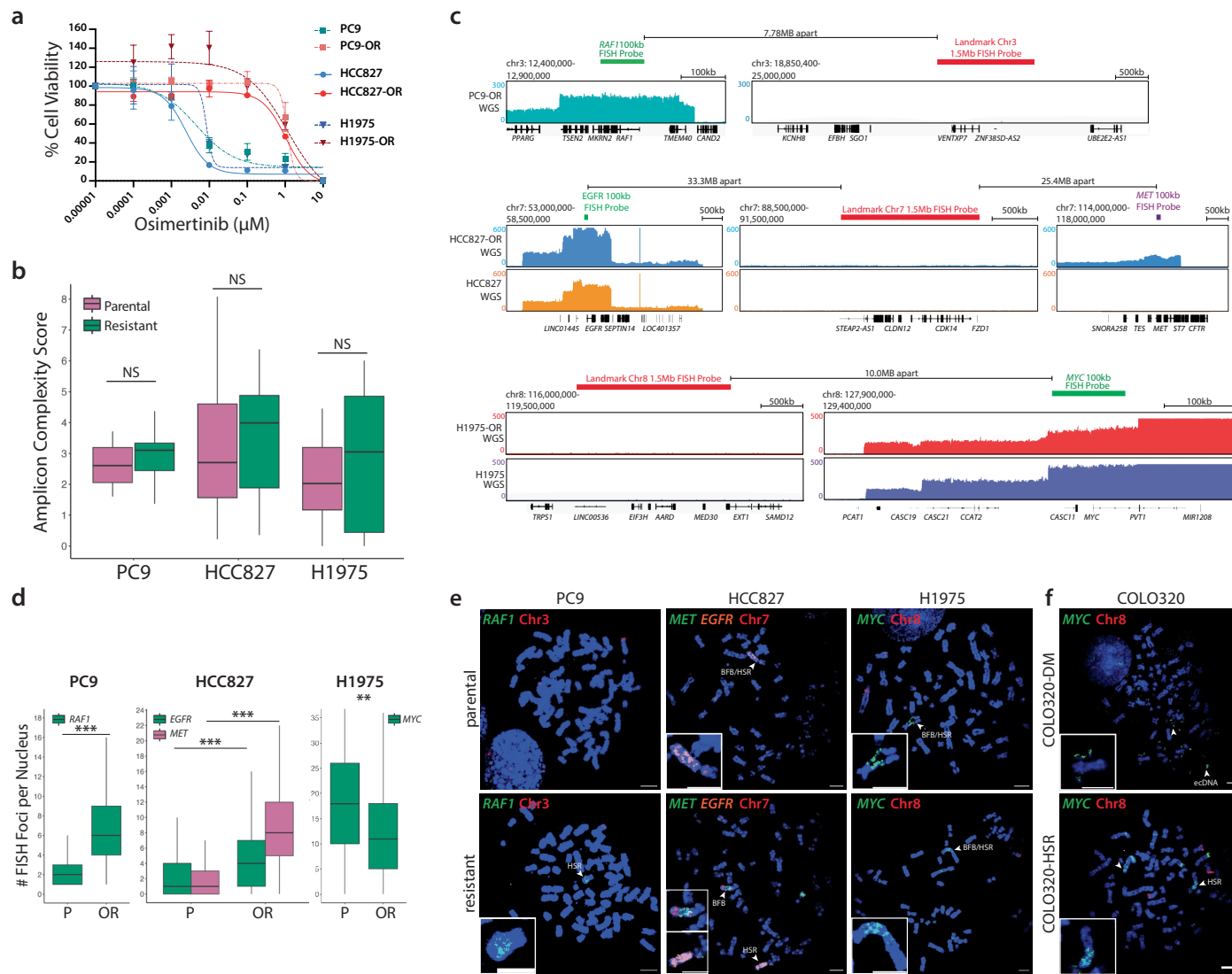
Extended data is available for this paper at <https://doi.org/10.1038/s41594-025-01685-4>.

Supplementary information The online version contains supplementary material available at <https://doi.org/10.1038/s41594-025-01685-4>.

Correspondence and requests for materials should be addressed to Andrew Z. Xiao.

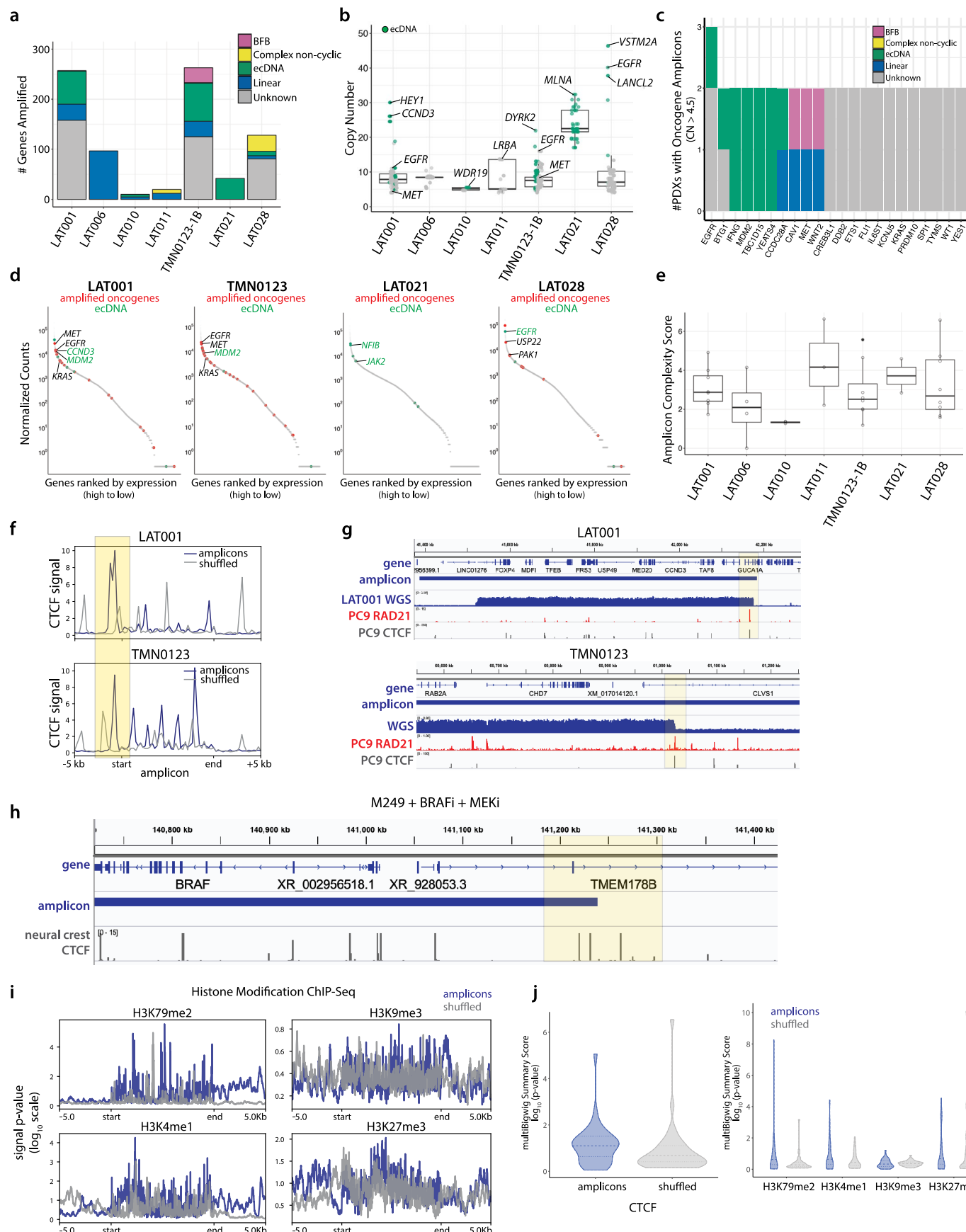
Peer review information *Nature Structural & Molecular Biology* thanks the anonymous reviewer(s) for their contribution to the peer review of this work.

Reprints and permissions information is available at www.nature.com/reprints.



Extended Data Fig. 1 | Oncogene amplification occurs in EGFR-mutant LUADs.
a, Cell viability curves in EGFR-mutant LUAD cell lines PC9, HCC827, and H1975 comparing osimertinib sensitivity between parental cells and osimertinib-resistant (OR) cell lines. Mean is plotted and error bars represent standard deviation between three biological replicates. **b**, Amplicon complexity score increases, although not statistically significant (NS), in osimertinib resistant cells compared to parental cells. WGS data is from one biological replicate per cell line. Box plot center: median; hinges: first and third quartiles; whiskers: hinge $\pm 1.5 \times$ IQR. Statistics: Two-sided Wilcoxon rank-sum exact test. **c**, WGS IGV tracks with schematic of DNA FISH probe design strategy. DNA FISH probes

were designed to target a 100 kb amplified locus or a 1.5 Mb unamplified control locus. **d**, Quantification of FISH foci from Fig. 1c. P values determined by two-sided Wilcoxon test. ** $P < 0.01$, *** $P < 2.2 \times 10^{-16}$. N = 1042 cells (PC9); N = 584 cells (H1975); N = 1179 cells (HCC927), from 3 independent experiments. Box plot center: median; hinges: first and third quartiles; whiskers: hinge $\pm 1.5 \times$ IQR. P: parental; OR: osimertinib-resistant. **e**, Representative metaphase FISH images in sensitive and resistant cells. Scale bars are 5 μm in all images except PC9-OR HSR inset, which has a 3 μm scale bar. Representative images from 3 biological replicates. **f**, Metaphase FISH images from COLO320-DM (top) and COLO320-HSR (bottom) which exhibit ecDNA- and HSR-like MYC amplicons, respectively.

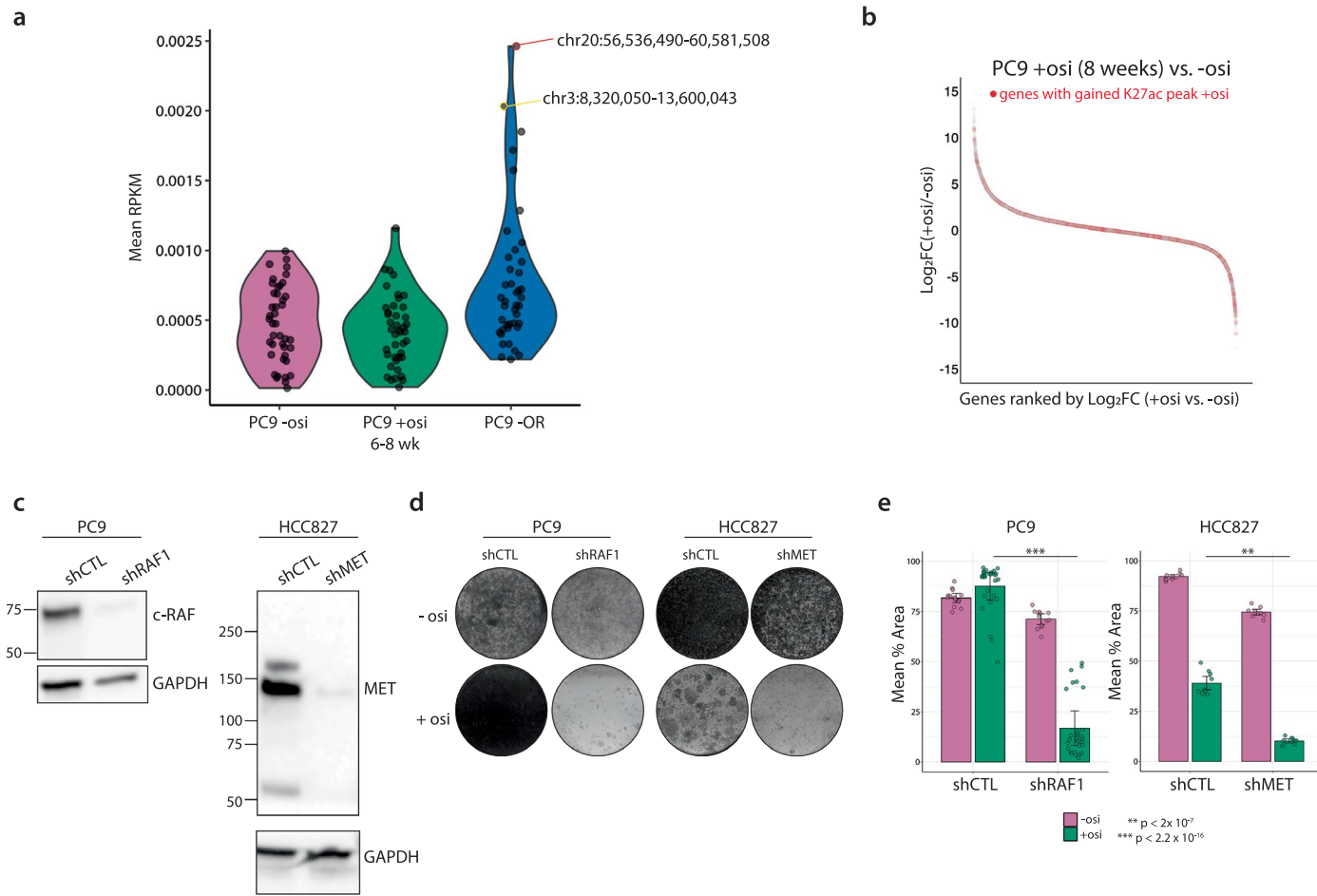


Extended Data Fig. 2 | See next page for caption.

Extended Data Fig. 2 | Oncogene amplicons have a pre-defined chromatin architecture. **a**, Breakdown of amplicon structures in PDX tumors derived from osimertinib-treated LUAD tumors. **b**, Copy number of amplified genes in PDX LUAD samples. Green: genes predicted to be amplified as ecDNA based on AA. Box plot center: median; hinges: first and third quartiles; whiskers: hinge $\pm 1.5 \times \text{IQR}$. **c**, Bar chart showing commonly amplified oncogenes across PDX tumor samples, colored by amplicon classification. **d**, Ranked RNA expression plots in osimertinib-treated PDX LUADs. Red dots: amplified oncogenes; green dots: ecDNA based on WGS/AA analysis. **e**, Amplicon complexity scores in PDX LUAD samples. Box plot center: median; hinges: first and third quartiles; whiskers: hinge $\pm 1.5 \times \text{IQR}$. **f**, Analysis of CTCF signal in PC9 cells based on the boundaries of amplicons from PDX tumors. CTCF is enriched at the boundaries of

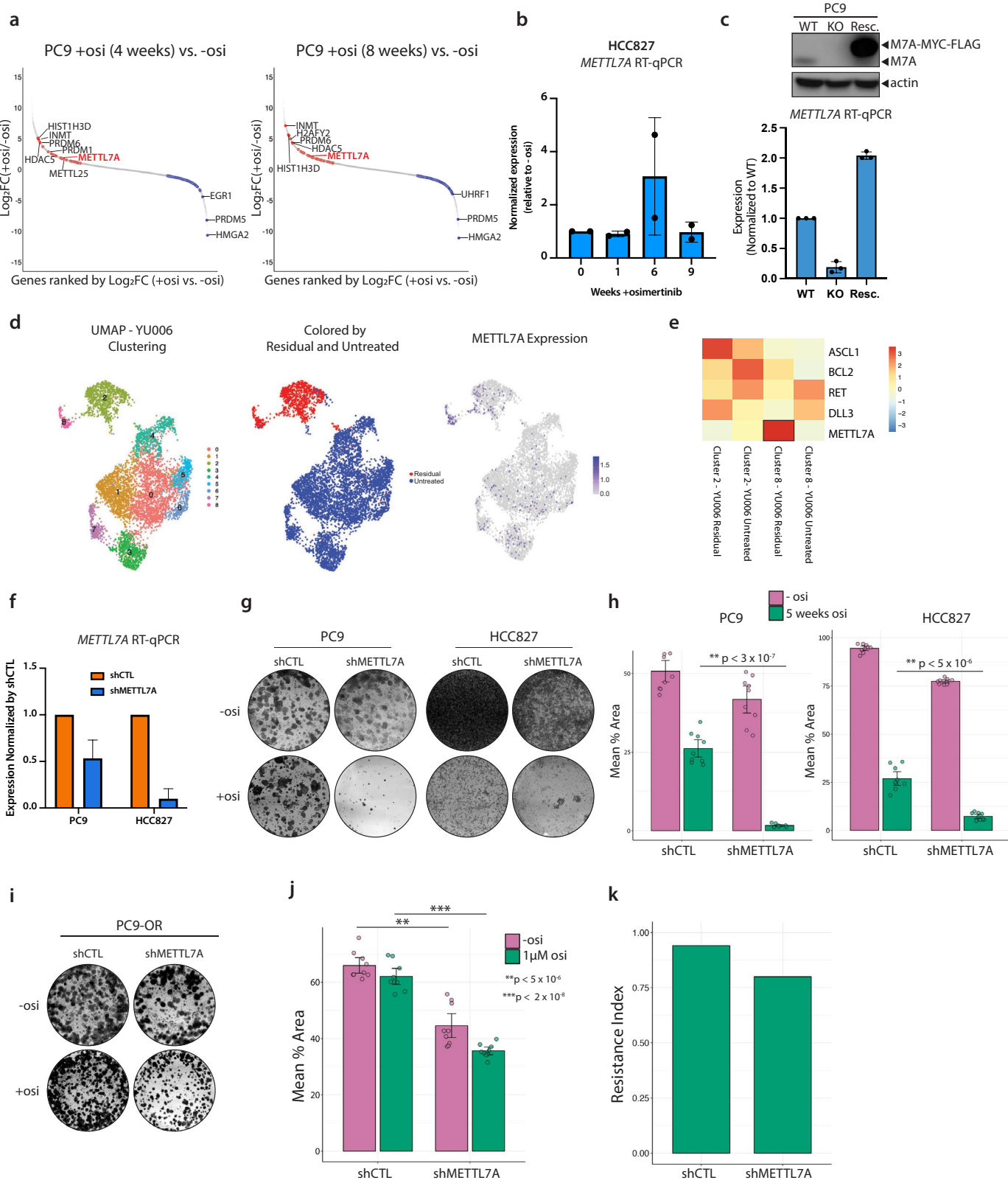
amplicons from PDX samples LAT001 and TMN0123. **g**, Example IGV sequencing tracks of PC9 CTCF signal (grey) and PC9 RAD21 signal (red) correlated with the boundaries of the amplicons from PDX tumors LAT001 (top) and TMN0123 (bottom). Both CTCF and RAD21 are enriched at one amplicon boundary.

h, Example IGV sequencing track of CTCF signal from neural crest cells correlated with the boundary of the *BRAF* amplicon in M249 cells resistant to BRAFi and MEKi. **i**, Profile plots of histone modification ChIP-Seq from ENCODE in PC9 cells across amplicons identified by AmpliconArchitect in PC9-OR cells or shuffled control regions. Signal p-value bigWig files (note: \log_{10} scale) were used for plotting. **j**, Quantification of signal p-value bigWig files from ENCODE. (left) Quantification of CTCF ChIP-Seq ± 5 kb of amplicons or shuffled regions. (right) Quantification of histone modification ChIP-Seq from (**i**).



Extended Data Fig. 3 | Chromatin priming precedes oncogene amplification. **a**, Genome coverage (RPKM) based on H2A CUT&RUN in PC9 cells treated without osimertinib or with osimertinib for 6–8 or 12+ (PC9-OR) weeks. Each dot represents an amplicon locus determined by AA in PC9-OR cells. Signal is normalized for sequencing depth. **b**, Ranked RNA expression plot showing Log₂FC between PC9 cells treated with osimertinib for 8 weeks compared to parental cells. Genes that have gained an H3K27ac peak upon osimertinib treatment are highlighted in red. **c**, Western blots showing shRNA-mediated

knockdown efficiency of RAF1 in PC9 cells (left) and MET in HCC827 cells (right). **d**, Colony formation assay in PC9 (left) and HCC827 (right) cells expressing shRNAs targeting *RAF1* or *MET*, respectively, or a non-targeting control. Cells were treated with osimertinib for approximately 5 weeks and fixed and stained with crystal violet. **e**, Quantification of (d). P-values determined by an unpaired, two-sided t-test (PC9: $P = 2.2e-16$; HCC827: $P = 1.10e-07$). Mean is plotted and error bars represent standard deviation from three biological replicates.



Extended Data Fig. 4 | See next page for caption.

Extended Data Fig. 4 | METTL7A promotes the acquisition of osimertinib-resistant LUAD. **a**, Ranked RNA expression plot showing the differentially expressed ($P_{adj} < 0.001$) putative and known epigenetic factors that are upregulated (red, $\log_2 FC > 1$) or downregulated (blue, $\log_2 FC < 1$) after 4 (left) and 8 (right) weeks of osimertinib treatment. **b**, RT-qPCR of *METTL7A* in HCC827 cells treated with osimertinib at the indicated time points from two biological replicates. **c**, Top: Western blot in PC9 *METTL7A* WT, KO, or KO cells rescued by overexpressing *METTL7A*-MYC-FLAG. Bottom: RT-qPCR of *METTL7A* in *METTL7A* WT, KO, or KO cells rescued by overexpressing *METTL7A*-MYC-FLAG. **d**, (left) UMAP of YU-006 PDX samples colored based on clusters, (middle) colored by condition, (right) colored by *METTL7A* expression. **e**, Heatmap visualization showing *METTL7A* expression in clusters 2 and 8 from **(d)** along with previously identified factors such as *ASCL1*, that pre-exist in YU-006 untreated tumor.

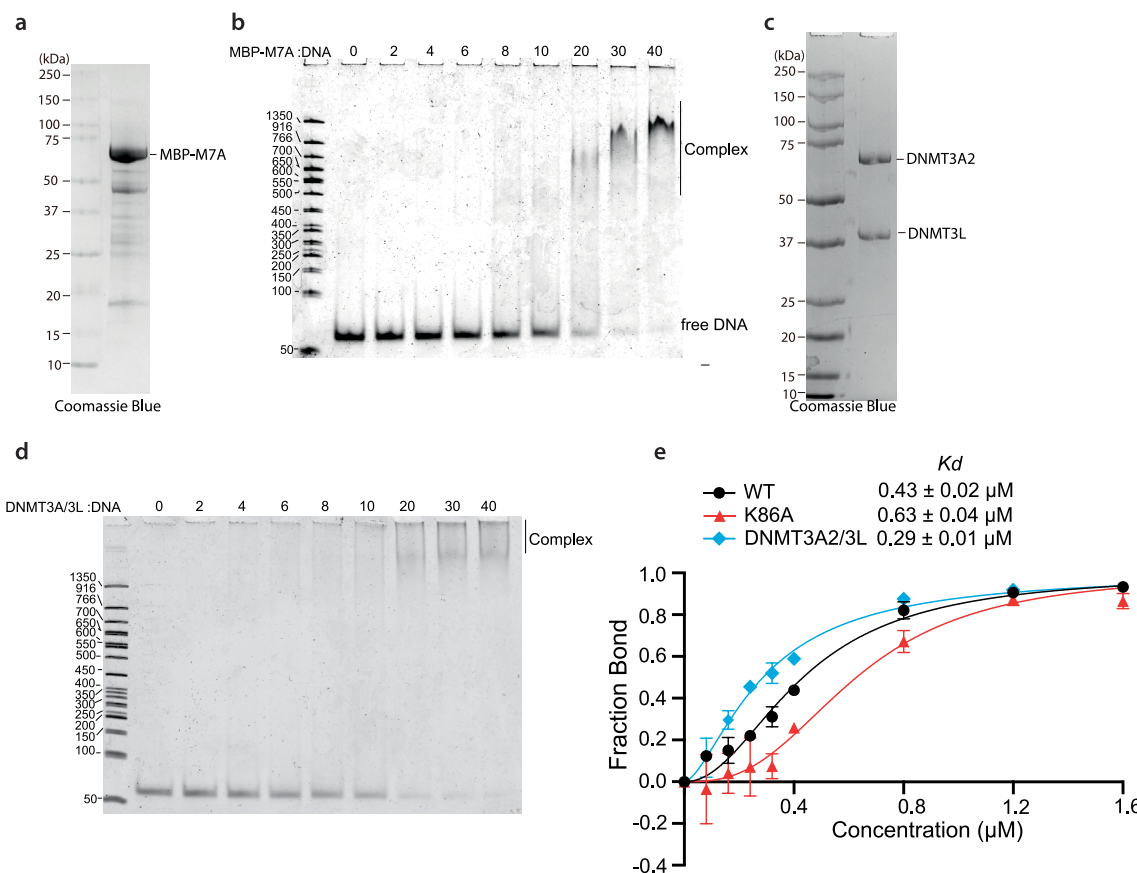
f, RT-qPCR of *METTL7A* in PC9 and HCC827 cells expressing a nontargeting control shRNA (shCTL) or an shRNA targeting *METTL7A*. Data from 3 technical replicates. Mean + SD is plotted. **g**, Colony formation assay in PC9 and HCC827 cells expressing an shRNA targeting *METTL7A* or a non-targeting shCTL. sh*METTL7A* cells fail to form osimertinib-resistant colonies after approximately 4 weeks. **h**, Quantification of **(g)**. Error bars represent standard deviation between biological triplicates. Significance determined by unpaired, two-sided t-test (PC9: $P = 2.994\text{e-}07$; HCC827: $P = 4.621\text{e-}06$). **i**, Colony formation assays in PC9-OR shCTL and sh*METTL7A* cells treated with or without osimertinib. **j**, Quantification of **(i)** via unpaired, two-sided t-test ($**P = 1.06\text{e-}08$; $***P = 4.515\text{e-}06$). **k**, Resistance index (mean percent area -osi/mean percent area +osi). Error bars represent standard deviation between biological triplicates with three technical replicates per biological replicate.



Extended Data Fig. 5 | See next page for caption.

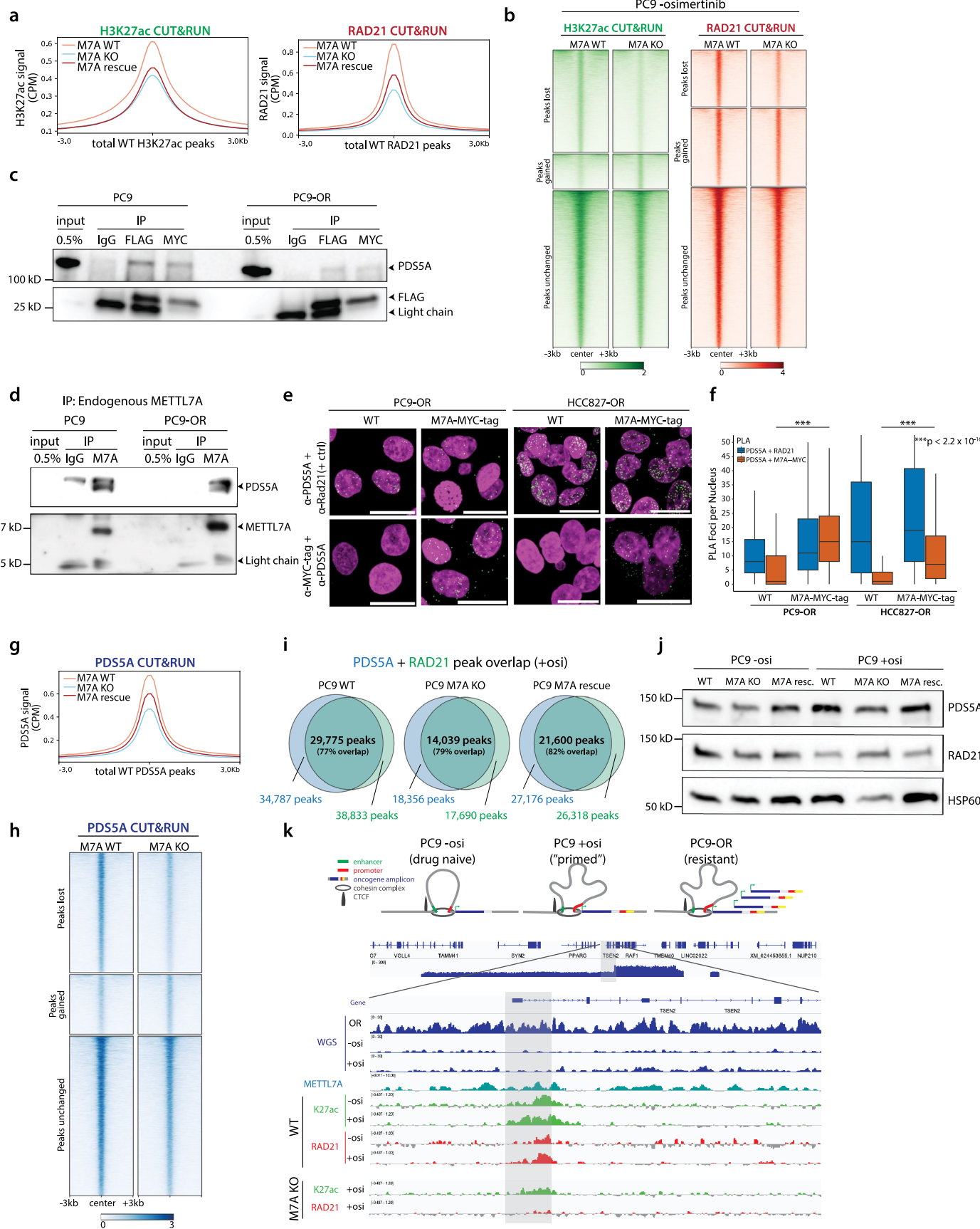
Extended Data Fig. 5 | METTL7A binds to amplified oncogenes. **a**, Subcellular fractionation of PC9 and HCC827 cells that express MYC-tagged METTL7A. Wildtype cells that do not express METTL7A-MYC were used as negative controls. α -tubulin, Calnexin, and Lamin B1 antibodies were used to ensure the purity of each indicated fraction. P: parental, OR: osimertinib-resistant. Two biological replicates were performed for each cell line with similar results. **b**, Overlap between METTL7A ChIP peaks and amplicons determined from WGS. **c**, Example IGV track of METTL7A enrichment over amplicons in PC9-OR cells. BigWig signal is normalized by ChIP input. **d**, METTL7A peak annotation in PC9-OR and HCC827-OR cells. **e**, METTL7A motif analysis via STREME. **f**, GO analysis of

METTL7A promoter peaks in PC9-OR and HCC827-OR cells. P values: Fisher Exact test. **g**, Venn diagrams showing overlap between METTL7A and H3K9me2 (top) and H3K9me3 (bottom). **h**, Western blot of rescue constructs overexpressed in the METTL7A KO background. EV = empty vector. Experiment was performed twice with similar results. **i**, Representative immunofluorescence images of METTL7A-FLAG tag in PC9-OR cells expressing either WT METTL7A-FLAG-tag or K86A-mutant METTL7A-FLAG-tag. Scale bar is 10 microns. **j**, Quantification of nuclear METTL7A-FLAG-tag foci. *** $P = 0.0003857$, two-sided Wilcoxon rank-sum exact test. Data from two biological replicates ($N = 782$ total cells). Box plot center: median; hinges: first and third quartiles; whiskers: hinge $+\/- 1.5 \times$ IQR.


Extended Data Fig. 6 | Recombinant METTL7A binds to DNA *in vitro*.

a, Coomassie gel showing MBP-tagged METTL7A purified from *E. coli*. **b**, Gel shift assay shows MBP-METTL7A-dsDNA complex formation at increasing ratios of MBP-METTL7A-to-dsDNA. **c**, SDS-PAGE image of purified DNMT3A2-DNMT3L complex. **d**, Gel shift assay showing human DNMT3A2/DNMT3L-dsDNA complex formation

at increasing ratios of DNMT3A-DNMT3L as a positive control. **e**, Quantification of binding assays using WT or K86A mutant MBP-tagged METTL7A or DNMT3A2/3L as a positive control. The K_d value was calculated based on the fraction of bound dsDNA at increasing concentrations of protein. Data from two biological replicates.

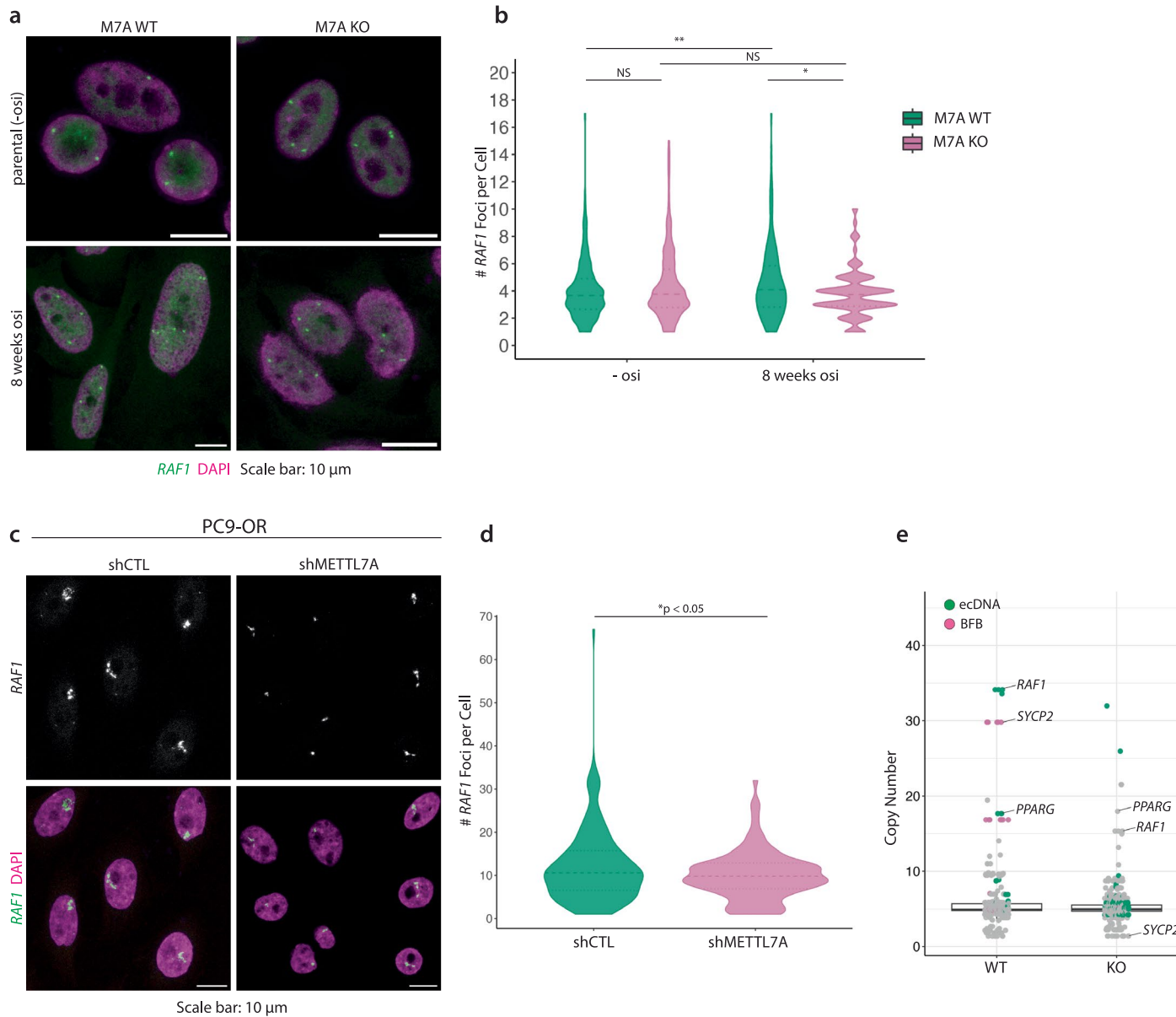


Extended Data Fig. 7 | See next page for caption.

Extended Data Fig. 7 | METTL7A affects the deposition of cohesin components.

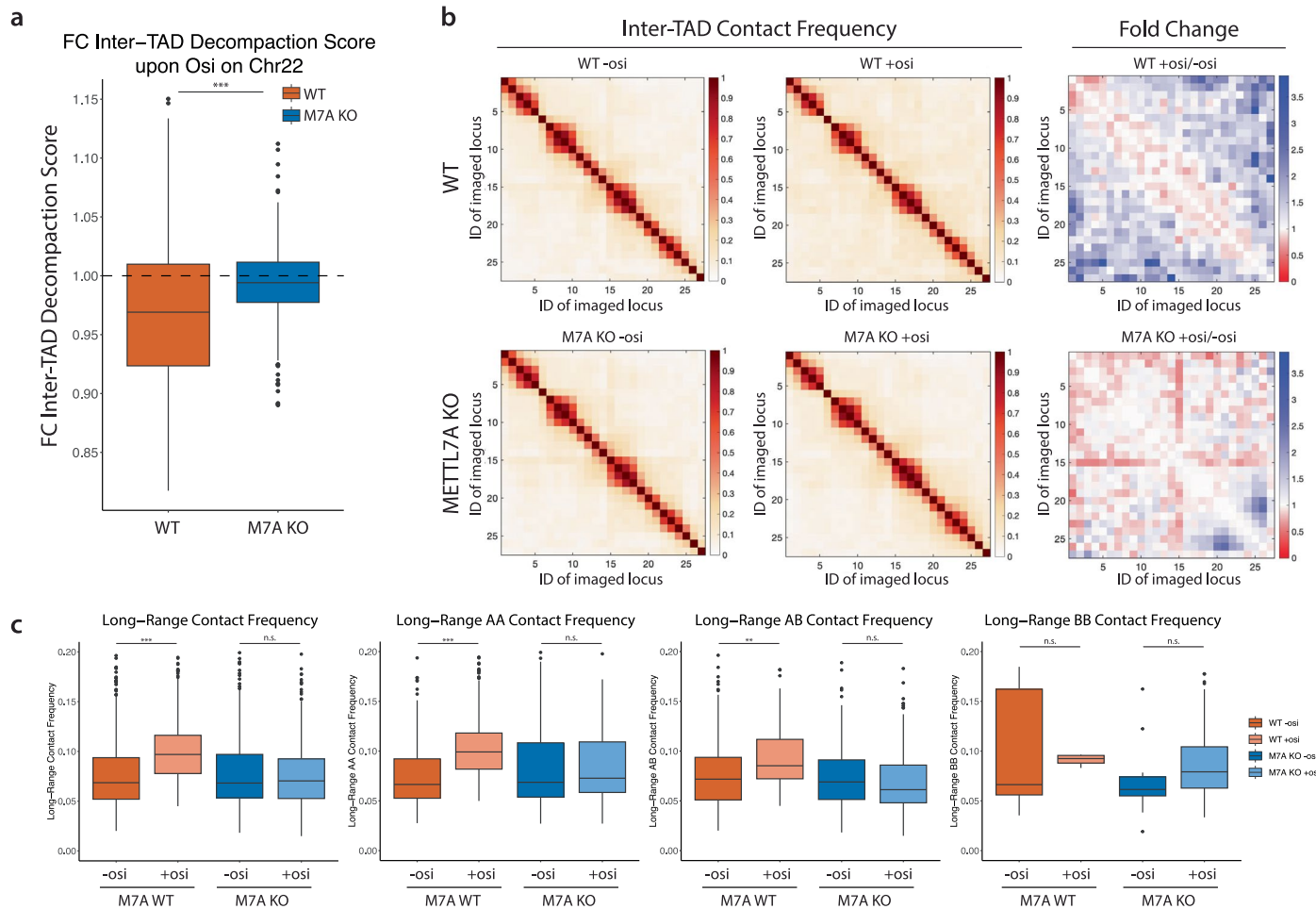
a, Metaplots of H3K27ac and RAD21 CUT&RUN in PC9 cells treated with osimertinib in the *METTL7A* (M7A) WT, KO, or rescue background. **b**, Heatmaps of H3K27ac and RAD21 CUT&RUN data in PC9 cells treated without osimertinib (parental cells). Signal is centered on peaks that were lost, gained, or unchanged upon M7A KO. CUT&RUN signal is normalized by CPM, H2A signal is subtracted, and mean bigWig signal between two biological replicates is shown. **c**, METTL7A-MYC-FLAG immunoprecipitation using antibodies against IgG, MYC, or FLAG followed by PDSSA western blotting shows binding between METTL7A-MYC-FLAG and PDSSA relative to 0.5% input. Anti-FLAG blotting shows the efficiency of each IP. Representative data from three biological replicates. **d**, METTL7A immunoprecipitation for endogenous METTL7A using antibodies against IgG or METTL7A followed by PDSSA western blotting shows binding between endogenous METTL7A and PDSSA. **e**, Proximity ligation assays in PC9-OR and HCC827-OR cells show that METTL7A and PDSSA are in close proximity. PDSSA and RAD21 antibodies were used as a positive control. Wildtype (WT) cells that do not express the METTL7A-MYC-FLAG fusion protein were used as a negative control. Green signal: PLA foci; magenta: DAPI. Scale bar: 20 μ m. **f**, Quantification of 7e. *** P = 2.2 \times 10⁻¹⁶, two-sided Wilcoxon rank-sum exact test. Data from 3

biological replicates ($N = 2,381$ total cells). Box plot center: median; hinges: first and third quartiles; whiskers: hinge +/- 1.5 * IQR. **g**, Metaplot of PDSSA CUT&RUN in PC9 cells treated with osimertinib in the *METTL7A* (M7A) WT, KO, or rescue background. **h**, Heatmaps of PDSSA CUT&RUN data in PC9 cells treated without osimertinib (parental cells). Signal is centered on peaks that were lost, gained, or unchanged upon M7A KO. CUT&RUN signal is normalized by CPM, H2A signal is subtracted, and mean bigWig signal between two biological replicates is shown. **i**, Overlap of PDSSA and RAD21 CUT&RUN peaks in cells treated with osimertinib. Percent overlap indicates percentage of overlapped peaks compared to total number of RAD21 peaks. **j**, Western blots of PDSSA and RAD21 show that changes in PDSSA and RAD21 deposition are not due to changes in protein levels. Representative data from two biological replicates. **k**, (top) Schematic depicting how the chromatin structure is “primed” during the acquisition of resistance prior to the development of resistant cells with oncogene amplification. (bottom) IGV tracks from WGS (dark blue), METTL7A ChIP in PC9-OR METTL7A-MYC cells (teal), H3K27ac CUT&RUN (green), and RAD21 CUT&RUN (red). H3K27ac and RAD21 are gained at the boundaries of the “future amplicons” (loci that are amplified in PC9-OR cells but not in “primed” cells). *METTL7A* KO leads to reduced H3K27ac and RAD21 at these loci.



Extended Data Fig. 8 | METTL7A affects gene copy number. **a**, *RAF1* FISH in PC9 WT and *METTL7A* KO parental cells and cells treated with osimertinib for 8 weeks. **b**, Quantification of *RAF1* DNA FISH in (a), unpaired, two-sided t-test (*P = 0.001354; **P = 0.0001231). **c**, *RAF1* FISH in PC9-OR shCTL and sh*METTL7A* cells. **d**, Quantification of *RAF1* DNA FISH in (c) with unpaired, two-sided t-test

(P = 0.04036). **e**, WGS and AA analysis of PC9-OR WT and KO cells shows a decrease in average copy number upon *METTL7A* depletion. WGS data from one biological replicate per cell line. Box plot center: median; hinges: first and third quartiles; whiskers: hinge +/- 1.5 * IQR.



Extended Data Fig. 9 | METTL7A affects chromatin compaction as cells acquire resistance to osimertinib. **a**, Fold change of inter-TAD decompaction score upon osimertinib (osi) treatment in PC9 WT and *METTL7A* (M7A) KO cells. Data is from 3 biological replicates (15,610 Chr22 traces total). Box plot center: median; hinges: first and third quartiles; whiskers: hinge $\pm 1.5 \times$ IQR. $P = 9.268e-14$, two-sided Wilcoxon signed rank test. **b**, Chr22 tracing reveals increased long-range inter-TAD contacts in wildtype cells treated with osimertinib compared to

METTL7A KO cells. **c**, Quantification of long-range inter-TAD contact frequency across all long-range inter-TAD pairs, AA inter-TAD pairs, AB inter-TAD pairs, and BB inter-TAD pairs. *** $P < 0.001$ [$P = 2.321e-16$, $P = 4.311e-14$]; ** $P < 0.01$ [$P = 0.001582$]; n.s. not significant; two-sided Wilcoxon rank-sum exact test) based on 3 biological replicates (15,610 Chr22 traces total). Box plot center: median; hinges: first and third quartiles; whiskers: hinge $\pm 1.5 \times$ IQR.

Reporting Summary

Nature Portfolio wishes to improve the reproducibility of the work that we publish. This form provides structure for consistency and transparency in reporting. For further information on Nature Portfolio policies, see our [Editorial Policies](#) and the [Editorial Policy Checklist](#).

Statistics

For all statistical analyses, confirm that the following items are present in the figure legend, table legend, main text, or Methods section.

n/a Confirmed

- The exact sample size (n) for each experimental group/condition, given as a discrete number and unit of measurement
- A statement on whether measurements were taken from distinct samples or whether the same sample was measured repeatedly
- The statistical test(s) used AND whether they are one- or two-sided
Only common tests should be described solely by name; describe more complex techniques in the Methods section.
- A description of all covariates tested
- A description of any assumptions or corrections, such as tests of normality and adjustment for multiple comparisons
- A full description of the statistical parameters including central tendency (e.g. means) or other basic estimates (e.g. regression coefficient) AND variation (e.g. standard deviation) or associated estimates of uncertainty (e.g. confidence intervals)
- For null hypothesis testing, the test statistic (e.g. F , t , r) with confidence intervals, effect sizes, degrees of freedom and P value noted
Give P values as exact values whenever suitable.
- For Bayesian analysis, information on the choice of priors and Markov chain Monte Carlo settings
- For hierarchical and complex designs, identification of the appropriate level for tests and full reporting of outcomes
- Estimates of effect sizes (e.g. Cohen's d , Pearson's r), indicating how they were calculated

Our web collection on [statistics for biologists](#) contains articles on many of the points above.

Software and code

Policy information about [availability of computer code](#)

Data collection	No custom code was used to collect the data in this study.
Data analysis	<p>FISH and Immunofluorescence Image Analysis Images were analyzed in CellProfiler using a custom pipeline to segment nuclei followed by identification of foci. The number of foci per cell were quantified and visualized in R (v4.2.1).</p> <p>Colony Formation Assay Analysis Green channel of each scanned plate was isolated and the area of each well was quantified using ImageJ. Three biological replicates were performed for each experiment with three technical replicates per condition.</p> <p>AmpliconArchitect and AmpliconClassifier WGS FASTQ files were processed using the AmpliconSuite-pipeline v0.1555.2 to call AmpliconArchitect v1.3.r5 and AmpliconClassifier v0.5.3. and CNVKit v0.9.10against GRCh38. Default settings were run with GRCh38 set as reference genome. Amplicon complexity scores were retrieved from the output of AmpliconClassifier and measures the diversity of amplicons. To perform grouped analysis in paired sensitive and resistant cells, GroupedAnalysis.py was run to collate all seed regions before invoking AmpliconArchitect for paired parental and osimertinib-resistant cell lines.</p> <p>WES Analysis of Oncogene Amplification BAM files were retrieved from dbGaP accession code phs002001. CNVKit v0.9.9 was used to analyze for copy number variation between post- osimertinib treated tumors and pre- osimertinib tumors. The pre-treated sample was inputted using the --normal flag. The --target flag was provided from Agilent as S06588914_Regions.bed file as the original patient samples were processed using SureSelect Clinical Research</p>

Exome Kit. The --annotate flag was provided from UCSC as refFlat.txt for hg19. RPKM for RNA-seq were retrieved from the supplemental information of PMID 32483558.

RNA-seq analysis

Sequencing reads were aligned with STAR version 2.7.7a using a GRCh38 STAR index. Gene expression was quantified using featureCounts from Subread version 2.0.3. DESeq2 was used for differential analysis. To profile differentially expressed epigenetic factors, the GSEA database was used to search for epigenetic gene lists. A single list of known or putative epigenetic and/or chromatin factors was curated by combining GSEA lists: "REACTOME_EPIGENETIC_REGULATION_OF_GENE_EXPRESSION," "GOMF_TRANSFERASE_ACTIVITY," "GOMF_DOUBLE_STRANDED_METHYLATED_DNA_BINDING", and "GOBP_NEGATIVE_REGULATION_OF_GENE_EXPRESSION_EPIGENETIC".

ChIP-seq analysis

Adapter sequences from paired-end sequencing reads were trimmed with Trimmomatic and quality control was performed using FastQC. Bowtie2 version 2.4.2 was used to align reads to the GRCh37 genome using the –very-sensitive flag and allowing for one mismatch. SAMtools version 1.16 was used to remove unmapped reads, secondary alignment reads, and reads with a Phred score of <30. Macs2 version 2.2.7.1 was used to call peaks with default peak-calling settings. Peaks were called against input chromatin. Peaks from 2 biological replicates were merged. Deeptools version 3.5.1 was used for ChIP-seq data visualization. Plots depicting ChIP-seq signal were generated by using Deeptools bamCoverage to normalize signal by CPM and duplicates were ignored. Peak intersections were performed using BEDTools v2.30 and quantified using BEDTools Fisher. The mean bigWig signal between biological replicates was plotted.

GO Analysis

ChIP-seq peaks were annotated to the nearest gene using ChIPseeker and promoter peaks were filtered before running EnrichR (<https://maayanlab.cloud/Enrichr/>). The top five significant terms ranked by p-value from ENCODE and ChEA Consensus TFs from ChIP-X were plotted.

MEME Analysis

FASTA sequences were generated using the center of ChIP-seq peaks with flanking windows of 250bp (total window size of 500bp). Enriched motifs were identified using MEME v5.4.1 meme-chip. The top three STREME outputs ranked by p-value were visualized in R using universtalmotif v3.15.

CUT&RUN analysis

Adapter sequences from paired-end sequencing reads were trimmed with Trimmomatic and quality control was performed using FastQC. Bowtie2 version 2.4.2 was used to align reads to the GRCh37 genome using the –very-sensitive flag and allowing for one mismatch. SAMtools version 1.16 was used to remove unmapped reads, secondary alignment reads, and reads with a Phred score of <30. Macs2 version 2.2.7.1 was used to call peaks with default peak-calling settings. Peaks were called against H2A. IgG peaks were subtracted from BED files using BEDTools v2.30. IDR was used to determine significant peaks between two biological replicates. Deeptools version 3.5.1 was used for data visualization. Plots depicting CUT&RUN signal were generated by using Deeptools bamCompare to normalize signal by CPM and to H2A, and duplicates were ignored. In all plots, the mean normalized bigWig signal between two biological replicates is plotted. Signal is Peak intersections were performed using BEDTools v2.30.

Mass spectrometry

Proteins were identified by database search using MaxQuant (Max Planck Institute) with a parent ion tolerance of 3 ppm and a fragment ion tolerance of 0.5 Da. Scaffold Q+S (Proteome Software) was used to verify MS/MS based peptide and protein identifications. Protein identifications were accepted if they could be established with less than 1.0% false discovery and contained at least 2 identified peptides. Protein probabilities were assigned by the Protein Prophet algorithm.

Mass spectrometry analysis

Analysis of mass spectrometry hits was performed with the SAINTExpress/APOSTL pipeline. A samples report was generated from Scaffold using the following parameters: protein threshold of 99%, minimum number of peptides = 1, and peptide threshold of 95%. Known contaminants such as keratin were manually removed. The samples report containing both biological replicates per sample was then uploaded to the APOSTL Galaxy Server. Wildtype cells not expressing the METTL7A-MYC-FLAG fusion protein were set as negative controls. The CRAPome was queried to exclude known contaminants from analysis. Thresholds were set by using a SAINT score > 0.5 and log2FC > 2.

Chromatin Tracing

The MATLAB programs for data analysis are available at <https://github.com/SiyuanWangLab/MINA> and in Liu et al., in submission. The following software were used MATLAB version R2022a.

For manuscripts utilizing custom algorithms or software that are central to the research but not yet described in published literature, software must be made available to editors and reviewers. We strongly encourage code deposition in a community repository (e.g. GitHub). See the Nature Portfolio [guidelines for submitting code & software](#) for further information.

Data

Policy information about [availability of data](#)

All manuscripts must include a [data availability statement](#). This statement should provide the following information, where applicable:

- Accession codes, unique identifiers, or web links for publicly available datasets
- A description of any restrictions on data availability
- For clinical datasets or third party data, please ensure that the statement adheres to our [policy](#)

WGS data has been deposited under PRJNA1065471.

RNA-Seq, ChIP-Seq, and CUT&RUN have been deposited in GEO database under accession number GSE254521. Imaging data can be provided upon reasonable request.

Research involving human participants, their data, or biological material

Policy information about studies with [human participants or human data](#). See also policy information about [sex, gender \(identity/presentation\), and sexual orientation](#) and [race, ethnicity and racism](#).

Reporting on sex and gender

NA

Reporting on race, ethnicity, or other socially relevant groupings

NA

Population characteristics

NA

Recruitment

NA

Ethics oversight

NA

Note that full information on the approval of the study protocol must also be provided in the manuscript.

Field-specific reporting

Please select the one below that is the best fit for your research. If you are not sure, read the appropriate sections before making your selection.

Life sciences

Behavioural & social sciences

Ecological, evolutionary & environmental sciences

For a reference copy of the document with all sections, see nature.com/documents/nr-reporting-summary-flat.pdf

Life sciences study design

All studies must disclose on these points even when the disclosure is negative.

Sample size

No sample size calculations were performed. Experiments were performed with two or more replicates to capture variability and reproducibility. Imaging quantifications included >100 cells per level for confocal imaging experiments. Sequencing experiments were performed with at least two biological replicates, which has been a standard.

Data exclusions

No data was excluded.

Replication

Experiments were performed with two or more replicates to capture variability. All replication attempts were successful.

Randomization

All experiments used cultured cell lines. No live organisms were used and, thus, randomization was not relevant to this study.

Blinding

Blinding was not relevant to this study as researchers needed to know the conditions for each experiment.

Reporting for specific materials, systems and methods

We require information from authors about some types of materials, experimental systems and methods used in many studies. Here, indicate whether each material, system or method listed is relevant to your study. If you are not sure if a list item applies to your research, read the appropriate section before selecting a response.

Materials & experimental systems

- | | |
|-------------------------------------|---|
| n/a | Involved in the study |
| <input type="checkbox"/> | <input checked="" type="checkbox"/> Antibodies |
| <input type="checkbox"/> | <input checked="" type="checkbox"/> Eukaryotic cell lines |
| <input checked="" type="checkbox"/> | <input type="checkbox"/> Palaeontology and archaeology |
| <input checked="" type="checkbox"/> | <input type="checkbox"/> Animals and other organisms |
| <input type="checkbox"/> | <input checked="" type="checkbox"/> Clinical data |
| <input checked="" type="checkbox"/> | <input type="checkbox"/> Dual use research of concern |
| <input type="checkbox"/> | <input type="checkbox"/> Plants |

Methods

- | | |
|-------------------------------------|---|
| n/a | Involved in the study |
| <input type="checkbox"/> | <input checked="" type="checkbox"/> ChIP-seq |
| <input checked="" type="checkbox"/> | <input type="checkbox"/> Flow cytometry |
| <input checked="" type="checkbox"/> | <input type="checkbox"/> MRI-based neuroimaging |

Antibodies

Antibodies used

IgG isotype control (CST 5415S), c-MYC-tag (Cell Signaling Technologies 2276S), Goat anti-Mouse IgG Alexa Fluor™ 488 (Thermo Fisher, A-11001), Goat anti-Mouse IgG Alexa Fluor™ 568 (Thermo Fisher, A-11031), anti-FLAG M2 1:1000 (Sigma F1804), anti-FLAG

1:1000 (Sigma F7425), anti-MYC-tag 1:1000 (CST 2276S), Histone H3 1:1000 (CST 4499), PDS5A 1:1000 (Thermo Fisher, PA5-57755), Lamin B1 1:1000 (Proteintech 66095-1), Calnexin 1:1000 (CST 2679), alpha-Tubulin 1:1000 (CST 2144S), CoxIV 1:1000 (abcam ab16056), cRAF 1:1000 (CST 53745), MET 1:1000 (CST 4560), Histone H2A 1:1000 (12349), RAD21 1:1000 (Active Motif 91245), H3K27ac 1:1000 (CST 8173) and IgG (EpiCypher 13-0042).

Validation

All antibodies were validated by the manufacturers (validation described below).

IgG isotype control (CST 5415S) - <https://www.cellsignal.com/products/primary-antibodies/mouse-g3a1-mab-igg1-isotype-control/5415> Validated by manufacturer via IF, ChIP, western blot.
 c-MYC-tag (Cell Signaling Technologies 2276S) - <https://www.cellsignal.com/products/primary-antibodies/myc-tag-9b11-mouse-mab/2276> Validated by manufacturer via IF, IHC, western blot.
 Goat anti-Mouse IgG Alexa Fluor™ 488 (Thermo Fisher, A-11001) - <https://www.thermofisher.com/antibody/product/Goat-anti-Mouse-IgG-H-L-Cross-Adsorbed-Secondary-Antibody-Polyclonal/A-11001> Validated by manufacturer via IF
 Goat anti-Mouse IgG Alexa Fluor™ 568 (Thermo Fisher, A-11031) - <https://www.thermofisher.com/antibody/product/Goat-anti-Mouse-IgG-H-L-Highly-Cross-Adsorbed-Secondary-Antibody-Polyclonal/A-11031> Validated by manufacturer via IF
 anti-FLAG M2 (Sigma F1804) - <https://www.sigmaldrich.com/US/en/product/sigma/f1804> Validated by manufacturer via western blot, IP, IF. Immunogen is specific to FLAG peptide.
 anti-FLAG (Sigma F7425) - <https://www.sigmaldrich.com/US/en/product/sigma/f7425>
 anti-MYC-tag (CST 2276S), Histone H3 (CST 4499) - Validated by manufacturer via western blot and IF.
 PDS5A (Thermo Fisher, PA5-57755) - <https://www.thermofisher.com/antibody/product/PDS5A-Antibody-Polyclonal/PA5-57755> Validated by manufacturer via IF, IHC, western blot.
 Lamin B1 (Proteintech 66095-1) - <https://www.ptglab.com/products/LMNB1-Antibody-66095-1-Ig.htm> Validated by manufacturer via IF, IHC, western blot.
 Calnexin 1:1000 (CST 2679) - <https://www.cellsignal.com/products/primary-antibodies/calnexin-c5c9-rabbit-mab/2679> Validated by manufacturer via IF, IHC, western blot.
 alpha-Tubulin (CST 2144S) - <https://www.cellsignal.com/products/primary-antibodies/a-tubulin-antibody/2144> Validated by manufacturer via IF, IHC, western blot.
 CoxIV (abcam ab16056) - <https://www.abcam.com/products/primary-antibodies/cox-iv-antibody-mitochondrial-loading-control-ab16056.html> Validated by manufacturer via IF, IHC, western blot.
 cRAF (CST 53745) - <https://www.cellsignal.com/products/primary-antibodies/c-raf-d4b3j-rabbit-mab/53745> Validated by manufacturer via western blot.
 MET (CST 4560) - <https://www.cellsignal.com/products/primary-antibodies/met-antibody/4560> Validated by manufacturer via western blot.
 Histone H2A (CST 12349) - Validated by manufacturer via western blot, IF, ChIP.
 RAD21 (Active Motif 91245) - <https://www.activemotif.com/catalog/details/91245/abflex-rad21-antibody-rab> Validated by manufacturer via western blot and IF.
 H3K27ac (CST 8173) - <https://www.cellsignal.com/products/primary-antibodies/acetyl-histone-h3-lys27-d5e4-xp-rabbit-mab/8173> Validated by manufacturer via western blot and IF.
 TOP2B (abcam ab72334) - <https://www.abcam.com/en-us/products/primary-antibodies/topoisomerase-ii-beta-top2b-antibody-ab72334?srsltid=AfmBOopMopiUKUy5AeBm6aTAFAvpp8BqtHRVHa2kZjKfO3L9NfSs8OJ> Validated by manufacturer via western blot and IHC.
 IgG (EpiCypher 13-0042) - <https://www.epicypher.com/products/nucleosomes/snap-cutana-spike-in-controls/cutana-rabbit-igg-cut-run-negative-control-antibody> Validated by manufacturer for CUT&RUN.
 METTL7A (OTI4B10, Thermo TA809878) - <https://www.thermofisher.com/antibody/product/METTL7A-Antibody-clone-OTI4B10-Monoclonal/TA809878>. Validated by manufacturer via western blot and IHC.

Eukaryotic cell lines

Policy information about [cell lines and Sex and Gender in Research](#)

Cell line source(s)

PC9 cells were obtained from ATCC. H1975 and HCC827 cells were a gift from K. Politi. COLO320DM and COLO320HSR were a gift from P. Mischel. BT474 cells were a gift from Q. Yan.

Authentication

None of the cell lines used were authenticated.

Mycoplasma contamination

All cell lines were tested regularly for mycoplasma at the Yale Virology Core.

Commonly misidentified lines (See [ICLAC](#) register)

None of the cell lines used are registered by ICLAC as commonly misidentified.

Clinical data

Policy information about [clinical studies](#)

All manuscripts should comply with the ICMJE [guidelines for publication of clinical research](#) and a completed [CONSORT checklist](#) must be included with all submissions.

Clinical trial registration

NCT02759835

Study protocol

https://classic.clinicaltrials.gov/ProvidedDocs/35/NCT02759835/Prot_SAP_000.pdf

Data collection

Data was not collected for this particular study as previously published sequencing data was analyzed.

Outcomes

No outcomes were measured for this particular study.

Plants

Seed stocks	NA
Novel plant genotypes	NA
Authentication	NA

ChIP-seq

Data deposition

- Confirm that both raw and final processed data have been deposited in a public database such as [GEO](#).
- Confirm that you have deposited or provided access to graph files (e.g. BED files) for the called peaks.

Data access links

May remain private before publication.

Data generated in this study have been deposited in GEO and are available under accession number GSE254521.

Raw fastq files, bigWig, merged BED files, and idr-identified narrowPeak files were uploaded.
At least two biological replicates were performed per experiment.

Files in database submission

ChIP-Seq:
 HCC827_M7A_OE_IgG_rep1_1.fq.gz
 HCC827_M7A_OE_IgG_rep1_2.fq.gz
 HCC827_M7A_OE_IgG_rep2_1.fq.gz
 HCC827_M7A_OE_IgG_rep2_2.fq.gz
 HCC827_M7A_OE_Input_rep1_1.fq.gz
 HCC827_M7A_OE_Input_rep1_2.fq.gz
 HCC827_M7A_OE_Input_rep2_1.fq.gz
 HCC827_M7A_OE_Input_rep2_2.fq.gz
 HCC827_M7A_OE_MYC_tag_rep1_1.fq.gz
 HCC827_M7A_OE_MYC_tag_rep1_2.fq.gz
 HCC827_M7A_OE_MYC_tag_rep2_1.fq.gz
 HCC827_M7A_OE_MYC_tag_rep2_2.fq.gz
 HCC827_OR_M7A_OE_IgG_rep1_1.fq.gz
 HCC827_OR_M7A_OE_IgG_rep1_2.fq.gz
 HCC827_OR_M7A_OE_IgG_rep2_1.fq.gz
 HCC827_OR_M7A_OE_IgG_rep2_2.fq.gz
 HCC827_OR_M7A_OE_Input_rep1_1.fq.gz
 HCC827_OR_M7A_OE_Input_rep1_2.fq.gz
 HCC827_OR_M7A_OE_Input_rep2_1.fq.gz
 HCC827_OR_M7A_OE_Input_rep2_2.fq.gz
 HCC827_OR_M7A_OE_MYC_tag_rep1_1.fq.gz
 HCC827_OR_M7A_OE_MYC_tag_rep1_2.fq.gz
 HCC827_OR_M7A_OE_MYC_tag_rep2_1.fq.gz
 HCC827_OR_M7A_OE_MYC_tag_rep2_2.fq.gz
 HCC827_OR_WT_IgG_rep1_1.fq.gz
 HCC827_OR_WT_IgG_rep1_2.fq.gz
 HCC827_OR_WT_IgG_rep2_1.fq.gz
 HCC827_OR_WT_IgG_rep2_2.fq.gz
 HCC827_OR_WT_Input_rep1_1.fq.gz
 HCC827_OR_WT_Input_rep1_2.fq.gz
 HCC827_OR_WT_Input_rep2_1.fq.gz
 HCC827_OR_WT_Input_rep2_2.fq.gz
 HCC827_OR_WT_MYC_tag_rep1_1.fq.gz
 HCC827_OR_WT_MYC_tag_rep1_2.fq.gz
 HCC827_OR_WT_MYC_tag_rep2_1.fq.gz
 HCC827_OR_WT_MYC_tag_rep2_2.fq.gz
 HCC827_WT_IgG_rep1_1.fq.gz
 HCC827_WT_IgG_rep1_2.fq.gz
 HCC827_WT_IgG_rep2_1.fq.gz
 HCC827_WT_IgG_rep2_2.fq.gz
 HCC827_WT_Input_rep1_1.fq.gz
 HCC827_WT_Input_rep1_2.fq.gz
 HCC827_WT_Input_rep2_1.fq.gz
 HCC827_WT_Input_rep2_2.fq.gz

HCC827_WT_MYC_tag_rep1_1.fq.gz
HCC827_WT_MYC_tag_rep1_2.fq.gz
HCC827_WT_MYC_tag_rep2_1.fq.gz
HCC827_WT_MYC_tag_rep2_2.fq.gz
HCC827_M7A_OE_IgG_mean.bigWig
HCC827_M7A_OE_Input_mean.bigWig
HCC827_M7A_OE_MYC_tag_mean.bigWig
HCC827_OR_M7A_OE_IgG_mean.bigWig
HCC827_OR_M7A_OE_Input_mean.bigWig
HCC827_OR_M7A_OE_MYC_tag_mean.bigWig
HCC827_OR_WT_IgG_mean.bigWig
HCC827_OR_WT_Input_mean.bigWig
HCC827_OR_WT_MYC_tag_mean.bigWig
HCC827_WT_IgG_mean.bigWig
HCC827_WT_Input_mean.bigWig
HCC827_WT_MYC_tag_mean.bigWig
HCC827_M7A_OE_IgG_idr
HCC827_M7A_OE_MYC_tag_idr
HCC827_OR_M7A_OE_IgG_idr
HCC827_OR_M7A_OE_MYC_tag_idr
HCC827_OR_WT_IgG_idr
HCC827_OR_WT_MYC_tag_idr
HCC827_WT_IgG_idr
HCC827_WT_MYC_tag_idr
PC9_M7A_OE_input_rep1_1.fq.gz
PC9_M7A_OE_input_rep1_2.fq.gz
PC9_M7A_OE_input_rep2_1.fq.gz
PC9_M7A_OE_input_rep2_2.fq.gz
PC9_M7A_OE_MYC_rep1_1.fq.gz
PC9_M7A_OE_MYC_rep1_2.fq.gz
PC9_M7A_OE_MYC_rep2_1.fq.gz
PC9_M7A_OE_MYC_rep2_2.fq.gz
PC9_OR_EV_input_rep1_1.fq.gz
PC9_OR_EV_input_rep1_2.fq.gz
PC9_OR_EV_input_rep2_1.fq.gz
PC9_OR_EV_input_rep2_2.fq.gz
PC9_OR_EV_MYC_rep1_1.fq.gz
PC9_OR_EV_MYC_rep1_2.fq.gz
PC9_OR_EV_MYC_rep2_1.fq.gz
PC9_OR_EV_MYC_rep2_2.fq.gz
PC9_OR_K86A_input_rep1_1.fq.gz
PC9_OR_K86A_input_rep1_2.fq.gz
PC9_OR_K86A_input_rep2_1.fq.gz
PC9_OR_K86A_input_rep2_2.fq.gz
PC9_OR_K86A_MYC_rep1_1.fq.gz
PC9_OR_K86A_MYC_rep1_2.fq.gz
PC9_OR_K86A_MYC_rep2_1.fq.gz
PC9_OR_K86A_MYC_rep2_2.fq.gz
PC9_OR_M7A_OE_input_rep1_1.fq.gz
PC9_OR_M7A_OE_input_rep1_2.fq.gz
PC9_OR_M7A_OE_input_rep2_1.fq.gz
PC9_OR_M7A_OE_input_rep2_2.fq.gz
PC9_OR_M7A_OE_MYC_rep1_1.fq.gz
PC9_OR_M7A_OE_MYC_rep1_2.fq.gz
PC9_OR_M7A_OE_MYC_rep2_1.fq.gz
PC9_OR_M7A_OE_MYC_rep2_2.fq.gz
PC9_OR_M7A_OE_MYC_rep2_2.fq.gz
PC9_OR_WT_input_rep1_1.fq.gz
PC9_OR_WT_input_rep1_2.fq.gz
PC9_OR_WT_input_rep2_1.fq.gz
PC9_OR_WT_input_rep2_2.fq.gz
PC9_OR_WT_MYC_rep1_1.fq.gz
PC9_OR_WT_MYC_rep1_2.fq.gz
PC9_OR_WT_MYC_rep2_1.fq.gz
PC9_OR_WT_MYC_rep2_2.fq.gz
PC9_WT_input_rep1_1.fq.gz
PC9_WT_input_rep1_2.fq.gz
PC9_WT_input_rep2_1.fq.gz
PC9_WT_input_rep2_2.fq.gz
PC9_WT_MYC_rep1_1.fq.gz
PC9_WT_MYC_rep1_2.fq.gz
PC9_WT_MYC_rep2_1.fq.gz
PC9_WT_MYC_rep2_2.fq.gz
PC9_M7A_OE_MYC_mean.bigWig
PC9_M7A_OE_MYC_merged.bed
PC9_OR_EV_MYC_mean.bigWig
PC9_OR_EV_MYC_merged.bed

```

PC9_OR_K86A_MYC_mean.bigWig
PC9_OR_K86A_MYC_merged.bed
PC9_OR_M7A_OE_MYC_mean.bigWig
PC9_OR_M7A_OE_MYC_merged.bed
PC9_OR_WT_MYC_mean.bigWig
PC9_OR_WT_MYC_merged.bed
PC9_WT_MYC_mean.bigWig
PC9_WT_MYC_merged.bed

CUT&RUN:
PC9_M7A_KO_H2A_rep1_1.fq.gz
PC9_M7A_KO_H2A_rep1_2.fq.gz
PC9_M7A_KO_H2A_rep2_1.fq.gz
PC9_M7A_KO_H2A_rep2_2.fq.gz
PC9_M7A_KO_H3K27Ac_rep1_1.fq.gz
PC9_M7A_KO_H3K27Ac_rep1_2.fq.gz
PC9_M7A_KO_H3K27Ac_rep2_1.fq.gz
PC9_M7A_KO_H3K27Ac_rep2_2.fq.gz
PC9_M7A_KO_IgG_rep1_1.fq.gz
PC9_M7A_KO_IgG_rep1_2.fq.gz
PC9_M7A_KO_IgG_rep2_1.fq.gz
PC9_M7A_KO_IgG_rep2_2.fq.gz
PC9_M7A_KO_osi_H2A_rep1_1.fq.gz
PC9_M7A_KO_osi_H2A_rep1_2.fq.gz
PC9_M7A_KO_osi_H2A_rep2_1.fq.gz
PC9_M7A_KO_osi_H2A_rep2_2.fq.gz
PC9_M7A_KO_osi_H3K27Ac_rep1_1.fq.gz
PC9_M7A_KO_osi_H3K27Ac_rep1_2.fq.gz
PC9_M7A_KO_osi_H3K27Ac_rep2_1.fq.gz
PC9_M7A_KO_osi_H3K27Ac_rep2_2.fq.gz
PC9_M7A_KO_osi_IgG_rep1_1.fq.gz
PC9_M7A_KO_osi_IgG_rep1_2.fq.gz
PC9_M7A_KO_osi_IgG_rep2_1.fq.gz
PC9_M7A_KO_osi_IgG_rep2_2.fq.gz
PC9_M7A_KO_osi_PDS5A_rep1_1.fq.gz
PC9_M7A_KO_osi_PDS5A_rep1_2.fq.gz
PC9_M7A_KO_osi_PDS5A_rep2_1.fq.gz
PC9_M7A_KO_osi_PDS5A_rep2_2.fq.gz
PC9_M7A_KO_osi_RAD21_rep1_1.fq.gz
PC9_M7A_KO_osi_RAD21_rep1_2.fq.gz
PC9_M7A_KO_osi_RAD21_rep2_1.fq.gz
PC9_M7A_KO_osi_RAD21_rep2_2.fq.gz
PC9_M7A_KO_PDS5A_rep1_1.fq.gz
PC9_M7A_KO_PDS5A_rep1_2.fq.gz
PC9_M7A_KO_PDS5A_rep2_1.fq.gz
PC9_M7A_KO_PDS5A_rep2_2.fq.gz
PC9_M7A_KO_RAD21_rep1_1.fq.gz
PC9_M7A_KO_RAD21_rep1_2.fq.gz
PC9_M7A_KO_RAD21_rep2_1.fq.gz
PC9_M7A_KO_RAD21_rep2_2.fq.gz
PC9_M7A_Rescue_H2A_rep1_1.fq.gz
PC9_M7A_Rescue_H2A_rep1_2.fq.gz
PC9_M7A_Rescue_H2A_rep2_1.fq.gz
PC9_M7A_Rescue_H2A_rep2_2.fq.gz
PC9_M7A_Rescue_H3K27Ac_rep1_1.fq.gz
PC9_M7A_Rescue_H3K27Ac_rep1_2.fq.gz
PC9_M7A_Rescue_H3K27Ac_rep2_1.fq.gz
PC9_M7A_Rescue_H3K27Ac_rep2_2.fq.gz
PC9_M7A_Rescue_IgG_rep1_1.fq.gz
PC9_M7A_Rescue_IgG_rep1_2.fq.gz
PC9_M7A_Rescue_IgG_rep2_1.fq.gz
PC9_M7A_Rescue_IgG_rep2_2.fq.gz
PC9_M7A_Rescue_osi_H2A_rep1_1.fq.gz
PC9_M7A_Rescue_osi_H2A_rep1_2.fq.gz
PC9_M7A_Rescue_osi_H2A_rep2_1.fq.gz
PC9_M7A_Rescue_osi_H2A_rep2_2.fq.gz
PC9_M7A_Rescue_osi_H3K27Ac_rep1_1.fq.gz
PC9_M7A_Rescue_osi_H3K27Ac_rep1_2.fq.gz
PC9_M7A_Rescue_osi_H3K27Ac_rep2_1.fq.gz
PC9_M7A_Rescue_osi_H3K27Ac_rep2_2.fq.gz
PC9_M7A_Rescue_osi_IgG_rep1_1.fq.gz
PC9_M7A_Rescue_osi_IgG_rep1_2.fq.gz
PC9_M7A_Rescue_osi_IgG_rep2_1.fq.gz
PC9_M7A_Rescue_osi_IgG_rep2_2.fq.gz
PC9_M7A_Rescue_osi_PDS5A_rep1_1.fq.gz
PC9_M7A_Rescue_osi_PDS5A_rep1_2.fq.gz

```

PC9_M7A_Rescue_osi_PDS5A_rep2_1.fq.gz
PC9_M7A_Rescue_osi_PDS5A_rep2_2.fq.gz
PC9_M7A_Rescue_osi_RAD21_rep1_1.fq.gz
PC9_M7A_Rescue_osi_RAD21_rep1_2.fq.gz
PC9_M7A_Rescue_osi_RAD21_rep2_1.fq.gz
PC9_M7A_Rescue_osi_RAD21_rep2_2.fq.gz
PC9_M7A_Rescue_PDS5A_rep1_1.fq.gz
PC9_M7A_Rescue_PDS5A_rep1_2.fq.gz
PC9_M7A_Rescue_PDS5A_rep2_1.fq.gz
PC9_M7A_Rescue_PDS5A_rep2_2.fq.gz
PC9_M7A_Rescue_RAD21_rep1_1.fq.gz
PC9_M7A_Rescue_RAD21_rep1_2.fq.gz
PC9_M7A_Rescue_RAD21_rep2_1.fq.gz
PC9_M7A_Rescue_RAD21_rep2_2.fq.gz
PC9_WT_H2A_rep1_1.fq.gz
PC9_WT_H2A_rep1_2.fq.gz
PC9_WT_H2A_rep2_1.fq.gz
PC9_WT_H2A_rep2_2.fq.gz
PC9_WT_H3K27Ac_rep1_1.fq.gz
PC9_WT_H3K27Ac_rep1_2.fq.gz
PC9_WT_H3K27Ac_rep2_1.fq.gz
PC9_WT_H3K27Ac_rep2_2.fq.gz
PC9_WT_IgG_rep1_1.fq.gz
PC9_WT_IgG_rep1_2.fq.gz
PC9_WT_IgG_rep2_1.fq.gz
PC9_WT_IgG_rep2_2.fq.gz
PC9_WT_osi_H2A_rep1_1.fq.gz
PC9_WT_osi_H2A_rep1_2.fq.gz
PC9_WT_osi_H2A_rep2_1.fq.gz
PC9_WT_osi_H2A_rep2_2.fq.gz
PC9_WT_osi_H3K27Ac_rep1_1.fq.gz
PC9_WT_osi_H3K27Ac_rep1_2.fq.gz
PC9_WT_osi_H3K27Ac_rep2_1.fq.gz
PC9_WT_osi_H3K27Ac_rep2_2.fq.gz
PC9_WT_osi_IgG_rep1_1.fq.gz
PC9_WT_osi_IgG_rep1_2.fq.gz
PC9_WT_osi_IgG_rep2_1.fq.gz
PC9_WT_osi_IgG_rep2_2.fq.gz
PC9_WT_osi_PDS5A_rep1_1.fq.gz
PC9_WT_osi_PDS5A_rep1_2.fq.gz
PC9_WT_osi_PDS5A_rep2_1.fq.gz
PC9_WT_osi_PDS5A_rep2_2.fq.gz
PC9_WT_osi_RAD21_rep1_1.fq.gz
PC9_WT_osi_RAD21_rep1_2.fq.gz
PC9_WT_osi_RAD21_rep2_1.fq.gz
PC9_WT_osi_RAD21_rep2_2.fq.gz
PC9_WT_PDS5A_rep1_1.fq.gz
PC9_WT_PDS5A_rep1_2.fq.gz
PC9_WT_PDS5A_rep2_1.fq.gz
PC9_WT_PDS5A_rep2_2.fq.gz
PC9_WT_RAD21_rep1_1.fq.gz
PC9_WT_RAD21_rep1_2.fq.gz
PC9_WT_RAD21_rep2_1.fq.gz
PC9_WT_RAD21_rep2_2.fq.gz
PC9_M7A_KO_H3K27Ac_idr
PC9_M7A_KO_IgG_idr
PC9_M7A_KO_osi_H3K27Ac_idr
PC9_M7A_KO_osi_IgG_idr
PC9_M7A_KO_osi_PDS5A_idr
PC9_M7A_KO_osi_RAD21_idr
PC9_M7A_KO_PDS5A_idr
PC9_M7A_KO_RAD21_idr
PC9_M7A_Rescue_H3K27Ac_idr
PC9_M7A_Rescue_IgG_idr
PC9_M7A_Rescue_osi_H3K27Ac_idr
PC9_M7A_Rescue_osi_IgG_idr
PC9_M7A_Rescue_osi_PDS5A_idr
PC9_M7A_Rescue_osi_RAD21_idr
PC9_M7A_Rescue_PDS5A_idr
PC9_M7A_Rescue_RAD21_idr
PC9_WT_H3K27Ac_idr
PC9_WT_IgG_idr
PC9_WT_osi_H3K27Ac_idr
PC9_WT_osi_IgG_idr
PC9_WT_osi_PDS5A_idr
PC9_WT_osi_RAD21_idr

PC9_WT_PDS5A_idr
PC9_WT_RAD21_idr
PC9_M7A_KO_H2A_mean.bigWig
PC9_M7A_KO_H3K27Ac_mean.bigWig
PC9_M7A_KO_IgG_mean.bigWig
PC9_M7A_KO_osi_H2A_mean.bigWig
PC9_M7A_KO_osi_H3K27Ac_mean.bigWig
PC9_M7A_KO_osi_IgG_mean.bigWig
PC9_M7A_KO_osi_PDS5A_mean.bigWig
PC9_M7A_KO_osi_RAD21_mean.bigWig
PC9_M7A_KO_PDS5A_mean.bigWig
PC9_M7A_KO_RAD21_mean.bigWig
PC9_M7A_Rescue_H2A_mean.bigWig
PC9_M7A_Rescue_H3K27Ac_mean.bigWig
PC9_M7A_Rescue_IgG_mean.bigWig
PC9_M7A_Rescue_osi_H2A_mean.bigWig
PC9_M7A_Rescue_osi_H3K27Ac_mean.bigWig
PC9_M7A_Rescue_osi_IgG_mean.bigWig
PC9_M7A_Rescue_osi_PDS5A_mean.bigWig
PC9_M7A_Rescue_osi_RAD21_mean.bigWig
PC9_M7A_Rescue_PDS5A_mean.bigWig
PC9_M7A_Rescue_RAD21_mean.bigWig
PC9_WT_H2A_mean.bigWig
PC9_WT_H3K27Ac_mean.bigWig
PC9_WT_IgG_mean.bigWig
PC9_WT_osi_H2A_mean.bigWig
PC9_WT_osi_H3K27Ac_mean.bigWig
PC9_WT_osi_IgG_mean.bigWig
PC9_WT_osi_PDS5A_mean.bigWig
PC9_WT_osi_RAD21_mean.bigWig
PC9_WT_PDS5A_mean.bigWig
PC9_WT_RAD21_mean.bigWig
PC9_M7A_KO_H2A_rep1_1.fq.gz
PC9_M7A_KO_H2A_rep1_2.fq.gz
PC9_M7A_KO_H2A_rep2_1.fq.gz
PC9_M7A_KO_H2A_rep2_2.fq.gz
PC9_M7A_KO_osi_H2A_rep1_1.fq.gz
PC9_M7A_KO_osi_H2A_rep1_2.fq.gz
PC9_M7A_KO_osi_H2A_rep2_1.fq.gz
PC9_M7A_KO_osi_H2A_rep2_2.fq.gz
PC9_M7A_KO_osi_TOP2B_rep1_1.fq.gz
PC9_M7A_KO_osi_TOP2B_rep1_2.fq.gz
PC9_M7A_KO_osi_TOP2B_rep2_1.fq.gz
PC9_M7A_KO_osi_TOP2B_rep2_2.fq.gz
PC9_M7A_KO_TOP2B_rep1_1.fq.gz
PC9_M7A_KO_TOP2B_rep1_2.fq.gz
PC9_M7A_KO_TOP2B_rep2_1.fq.gz
PC9_M7A_KO_TOP2B_rep2_2.fq.gz
PC9_WT_H2A_rep1_1.fq.gz
PC9_WT_H2A_rep1_2.fq.gz
PC9_WT_H2A_rep2_1.fq.gz
PC9_WT_H2A_rep2_2.fq.gz
PC9_WT_osi_H2A_rep1_1.fq.gz
PC9_WT_osi_H2A_rep1_2.fq.gz
PC9_WT_osi_H2A_rep2_1.fq.gz
PC9_WT_osi_H2A_rep2_2.fq.gz
PC9_WT_osi_TOP2B_rep1_1.fq.gz
PC9_WT_osi_TOP2B_rep1_2.fq.gz
PC9_WT_osi_TOP2B_rep2_1.fq.gz
PC9_WT_osi_TOP2B_rep2_2.fq.gz
PC9_WT_TOP2B_rep1_1.fq.gz
PC9_WT_TOP2B_rep1_2.fq.gz
PC9_WT_TOP2B_rep2_1.fq.gz
PC9_WT_TOP2B_rep2_2.fq.gz
PC9_M7A_KO_H2A_mean.bigWig
PC9_M7A_KO_osi_H2A_mean.bigWig
PC9_M7A_KO_osi_TOP2B_intersected_peaks.bed
PC9_M7A_KO_osi_TOP2B_mean.bigWig
PC9_M7A_KO_TOP2B_intersected_peaks.bed
PC9_M7A_KO_TOP2B_mean.bigWig
PC9_WT_H2A_mean.bigWig
PC9_WT_osi_H2A_mean.bigWig
PC9_WT_osi_TOP2B_intersected_peaks.bed
PC9_WT_osi_TOP2B_mean.bigWig
PC9_WT_TOP2B_intersected_peaks.bed

PC9_WT_TOP2B_mean.bigWig

Genome browser session
(e.g. [UCSC](#))

NA

Methodology

Replicates

Each experiment was performed at least twice with two biological replicates.

Sequencing depth

All sequencing was performed using paired-end 150bp reads. The total number of reads and uniquely mapped reads are provided below:

ChIP-Seq:

HCC827_WT_MYC_tag_rep1: 20096809 total read pairs, 15187952 uniquely mapped reads
 HCC827_OR_WT_MYC_tag_rep1: 20805602 total read pairs, 21324323 uniquely mapped reads
 HCC827_M7A_OE_MYC_tag_rep1: 16054232 total read pairs, 14142500 uniquely mapped reads
 HCC827_OR_M7A_OE_MYC_tag_rep1: 11430372 total read pairs, 6895236 uniquely mapped reads
 HCC827_WT_IgG_rep1: 9200008 total read pairs, 3842824 uniquely mapped reads
 HCC827_OR_WT_IgG_rep1: 11021060 total read pairs, 6768089 uniquely mapped reads
 HCC827_M7A_OE_IgG_rep1: 10003465 total read pairs, 5284670 uniquely mapped reads
 HCC827_OR_M7A_OE_IgG_rep1: 9220114 total read pairs, 3888705 uniquely mapped reads
 HCC827_WT_Input_rep1: 12513041 total read pairs, 5030898 uniquely mapped reads
 HCC827_OR_WT_Input_rep1: 29103215 total read pairs, 11392144 uniquely mapped reads
 HCC827_M7A_OE_Input_rep1: 22124231 total read pairs, 9988598 uniquely mapped reads
 HCC827_OR_M7A_OE_Input_rep1: 22224748 total read pairs, 7803662 uniquely mapped reads
 HCC827_WT_MYC_tag_rep2: 6932463 total read pairs, 4676024 uniquely mapped reads
 HCC827_OR_WT_MYC_tag_rep2: 8156000 total read pairs, 4926590 uniquely mapped reads
 HCC827_M7A_OE_MYC_tag_rep2: 14547574 total read pairs, 13685762 uniquely mapped reads
 HCC827_OR_M7A_OE_MYC_tag_rep2: 14010815 total read pairs, 9597552 uniquely mapped reads
 HCC827_WT_IgG_rep2: 10066860 total read pairs, 4970615 uniquely mapped reads
 HCC827_OR_WT_IgG_rep2: 8859046 total read pairs, 5901577 uniquely mapped reads
 HCC827_M7A_OE_IgG_rep2: 11973554 total read pairs, 3362932 uniquely mapped reads
 HCC827_OR_M7A_OE_IgG_rep2: 13158202 total read pairs, 5543043 uniquely mapped reads
 HCC827_WT_Input_rep2: 14765911 total read pairs, 4841248 uniquely mapped reads
 HCC827_OR_WT_Input_rep2: 19516130 total read pairs, 6921884 uniquely mapped reads
 HCC827_M7A_OE_Input_rep2: 21220205 total read pairs, 9547755 uniquely mapped reads
 HCC827_OR_M7A_OE_Input_rep2: 18718296 total read pairs, 7024155 uniquely mapped reads

CUT&RUN:

PC9_M7A_KO_H2A_rep1: 9963141 total read pairs, 15950991 uniquely mapped reads
 PC9_M7A_KO_H2A_rep2: 31764027 total read pairs, 39434077 uniquely mapped reads
 PC9_M7A_KO_IgG_rep1: 5129891 total read pairs, 7358294 uniquely mapped reads
 PC9_M7A_KO_IgG_rep2: 27813280 total read pairs, 21919446 uniquely mapped reads
 PC9_M7A_KO_H3K27Ac_rep1: 38986431 total read pairs, 32980989 uniquely mapped reads
 PC9_M7A_KO_H3K27Ac_rep2: 38591750 total read pairs, 32449422 uniquely mapped reads
 PC9_M7A_KO_osi_H2A_rep1: 35254101 total read pairs, 44629267 uniquely mapped reads
 PC9_M7A_KO_osi_H2A_rep2: 19662521 total read pairs, 25716237 uniquely mapped reads
 PC9_M7A_KO_osi_IgG_rep1: 32666319 total read pairs, 25394658 uniquely mapped reads
 PC9_M7A_KO_osi_IgG_rep2: 25682008 total read pairs, 24405330 uniquely mapped reads
 PC9_M7A_KO_osi_H3K27Ac_rep1: 29749723 total read pairs, 34021878 uniquely mapped reads
 PC9_M7A_KO_osi_H3K27Ac_rep2: 38236365 total read pairs, 43019646 uniquely mapped reads
 PC9_M7A_KO_osi_PDS5A_rep1: 33900546 total read pairs, 24174179 uniquely mapped reads
 PC9_M7A_KO_osi_PDS5A_rep2: 31967430 total read pairs, 23834827 uniquely mapped reads
 PC9_M7A_KO_osi_RAD21_rep1: 28523736 total read pairs, 22522296 uniquely mapped reads
 PC9_M7A_KO_osi_RAD21_rep2: 26040577 total read pairs, 23829866 uniquely mapped reads
 PC9_M7A_KO_PDS5A_rep1: 4930901 total read pairs, 6829903 uniquely mapped reads
 PC9_M7A_KO_PDS5A_rep2: 33847639 total read pairs, 19376079 uniquely mapped reads
 PC9_M7A_KO_RAD21_rep1: 8001175 total read pairs, 7928729 uniquely mapped reads
 PC9_M7A_KO_RAD21_rep2: 29701024 total read pairs, 21511194 uniquely mapped reads
 PC9_M7A_Rescue_H2A_rep1: 15977067 total read pairs, 23034081 uniquely mapped reads
 PC9_M7A_Rescue_H2A_rep2: 36652177 total read pairs, 46190066 uniquely mapped reads
 PC9_M7A_Rescue_IgG_rep1: 9301818 total read pairs, 9627399 uniquely mapped reads
 PC9_M7A_Rescue_IgG_rep2: 21292635 total read pairs, 13513151 uniquely mapped reads
 PC9_M7A_Rescue_H3K27Ac_rep1: 28773177 total read pairs, 37616960 uniquely mapped reads
 PC9_M7A_Rescue_H3K27Ac_rep2: 30507126 total read pairs, 39100770 uniquely mapped reads
 PC9_M7A_Rescue_osi_H2A_rep1: 41569411 total read pairs, 59007692 uniquely mapped reads
 PC9_M7A_Rescue_osi_H2A_rep2: 42150504 total read pairs, 53959324 uniquely mapped reads
 PC9_M7A_Rescue_osi_IgG_rep1: 28459837 total read pairs, 25073329 uniquely mapped reads
 PC9_M7A_Rescue_osi_IgG_rep2: 32397608 total read pairs, 21810759 uniquely mapped reads
 PC9_M7A_Rescue_osi_H3K27Ac_rep1: 43148593 total read pairs, 44189966 uniquely mapped reads
 PC9_M7A_Rescue_osi_H3K27Ac_rep2: 42965338 total read pairs, 41071891 uniquely mapped reads
 PC9_M7A_Rescue_osi_PDS5A_rep1: 46756808 total read pairs, 33932484 uniquely mapped reads
 PC9_M7A_Rescue_osi_PDS5A_rep2: 53169547 total read pairs, 30900806 uniquely mapped reads
 PC9_M7A_Rescue_osi_RAD21_rep1: 35742104 total read pairs, 27026970 uniquely mapped reads
 PC9_M7A_Rescue_osi_RAD21_rep2: 60707017 total read pairs, 24554966 uniquely mapped reads
 PC9_M7A_Rescue_PDS5A_rep1: 10048961 total read pairs, 13282160 uniquely mapped reads

PC9_M7A_Rescue_PDS5A_rep2: 27396123 total read pairs, 20842489 uniquely mapped reads
 PC9_M7A_Rescue_RAD21_rep1: 8523800 total read pairs, 9346321 uniquely mapped reads
 PC9_M7A_Rescue_RAD21_rep2: 28156369 total read pairs, 24554966 uniquely mapped reads
 PC9_WT_H2A_rep1: 7930857 total read pairs, 11504217 uniquely mapped reads
 PC9_WT_H2A_rep2: 34516451 total read pairs, 42940909 uniquely mapped reads
 PC9_WT_IgG_rep1: 5061586 total read pairs, 4415893 uniquely mapped reads
 PC9_WT_IgG_rep2: 27456664 total read pairs, 21242061 uniquely mapped reads
 PC9_WT_H3K27Ac_rep1: 23668699 total read pairs, 23969284 uniquely mapped reads
 PC9_WT_H3K27Ac_rep2: 26073870 total read pairs, 27014013 uniquely mapped reads
 PC9_WT_osi_H2A_rep1: 48662656 total read pairs, 64227835 uniquely mapped reads
 PC9_WT_osi_H2A_rep2: 49994018 total read pairs, 62252276 uniquely mapped reads
 PC9_WT_osi_IgG_rep1: 26647217 total read pairs, 21264548 uniquely mapped reads
 PC9_WT_osi_IgG_rep2: 31703846 total read pairs, 26351268 uniquely mapped reads
 PC9_WT_osi_H3K27Ac_rep1: 22336253 total read pairs, 25892853 uniquely mapped reads
 PC9_WT_osi_H3K27Ac_rep2: 34151501 total read pairs, 38867307 uniquely mapped reads
 PC9_WT_osi_PDS5A_rep1: 45170200 total read pairs, 29219991 uniquely mapped reads
 PC9_WT_osi_PDS5A_rep2: 46472301 total read pairs, 24659058 uniquely mapped reads
 PC9_WT_osi_RAD21_rep1: 52123253 total read pairs, 27403226 uniquely mapped reads
 PC9_WT_osi_RAD21_rep2: 43350262 total read pairs, 22957262 uniquely mapped reads
 PC9_WT_PDS5A_rep1: 5321947 total read pairs, 5181106 uniquely mapped reads
 PC9_WT_PDS5A_rep2: 29726446 total read pairs, 23561668 uniquely mapped reads
 PC9_WT_RAD21_rep1: 7614844 total read pairs, 5992363 uniquely mapped reads
 PC9_WT_RAD21_rep2: 31583612 total read pairs, 20670374 uniquely mapped reads

Antibodies

PDS5A (Thermo Fisher, PA5-57755), H3K27Ac (CST 8173), Rad21 (Active Motif 91245), c-MYC-tag (Cell Signaling Technologies 2276S), TOP2B (abcam ab72334), IgG isotype control (CST 5415S), Histone H2A (CST 12349). Validation described above.

Peak calling parameters

Bowtie2 was used to align reads with one mismatch. Peaks were called using MACS2 for all samples except TOP2B, for which peaks were called using SEACR. IDR was used to identify reproducible peaks

Data quality

Total number of reads and mapped reads were checked using fastQC and % of reads passing QC after alignment. IDR on default settings were used to identify reproducible peaks.

ChIP-Seq:

HCC827_M7A_OE_IgG_idr: 70 unique, reproducible peaks
 HCC827_M7A_OE_MYC_tag_idr: 2271 unique, reproducible peaks
 HCC827_OR_M7A_OE_IgG_idr: 96 unique, reproducible peaks
 HCC827_OR_M7A_OE_MYC_tag_idr: 3165 unique, reproducible peaks
 HCC827_OR_WT_IgG_idr: 2529 unique, reproducible peaks
 HCC827_OR_WT_MYC_tag_idr: 2767 unique, reproducible peaks
 HCC827_WT_IgG_idr: 1444 unique, reproducible peaks
 HCC827_WT_MYC_tag_idr: 1005 unique, reproducible peaks

CUT&RUN:

PC9_M7A_KO_H3K27Ac_idr: 23684 unique, reproducible peaks
 PC9_M7A_KO_IgG_idr: 170 unique, reproducible peaks
 PC9_M7A_KO_osi_H3K27Ac_idr: 39199 unique, reproducible peaks
 PC9_M7A_KO_osi_IgG_idr: 2705 unique, reproducible peaks
 PC9_M7A_KO_osi_PDS5A_idr: 18356 unique, reproducible peaks
 PC9_M7A_KO_osi_RAD21_idr: 17690 unique, reproducible peaks
 PC9_M7A_KO_PDS5A_idr: 9235 unique, reproducible peaks
 PC9_M7A_KO_RAD21_idr: 19011 unique, reproducible peaks
 PC9_M7A_Rescue_H3K27Ac_idr: 39514 unique, reproducible peaks
 PC9_M7A_Rescue_IgG_idr: 1053 unique, reproducible peaks
 PC9_M7A_Rescue_osi_H3K27Ac_idr: 45237 unique, reproducible peaks
 PC9_M7A_Rescue_osi_IgG_idr: 898 unique, reproducible peaks
 PC9_M7A_Rescue_osi_PDS5A_idr: 27176 unique, reproducible peaks
 PC9_M7A_Rescue_osi_RAD21_idr: 26318 unique, reproducible peaks
 PC9_M7A_Rescue_PDS5A_idr: 33602 unique, reproducible peaks
 PC9_M7A_Rescue_RAD21_idr: 24689 unique, reproducible peaks
 PC9_WT_H3K27Ac_idr: 22628 unique, reproducible peaks
 PC9_WT_IgG_idr: 1059 unique, reproducible peaks
 PC9_WT_osi_H3K27Ac_idr: 44132 unique, reproducible peaks
 PC9_WT_osi_IgG_idr: 7614 unique, reproducible peaks
 PC9_WT_osi_PDS5A_idr: 34787 unique, reproducible peaks
 PC9_WT_osi_RAD21_idr: 38833 unique, reproducible peaks
 PC9_WT_PDS5A_idr: 14398 unique, reproducible peaks
 PC9_WT_RAD21_idr: 15528 unique, reproducible peaks

Software

Trimmomatic (v0.39)
 FastQC (v0.11.9)
 Bowtie2 (v2.4.2)
 Burrows-Wheeler Aligner (BWA, v0.7.17)

SAMtools (v1.16)
Bedtools (v2.30.0)
Deeptools (v3.5.2)